ATOMIZED DIELECTRIC SPRAY-BASED ELECTRIC DISCHARGE MACHINING (SPRAY-EDM) FOR SUSTAINABLE MANUFACTURING

BY

ARVIND PATTABHIRAMAN

THESIS

Submitted in partial fulfillment of the requirements
for the degree of Master of Science in Mechanical Engineering
in the Graduate College of the
University of Illinois at Urbana-Champaign, 2015

Urbana, Illinois

Adviser:

Professor Shiv G. Kapoor

Abstract

Electrical Discharge Machining is a non-traditional machining process that is widely used in the tool and die-making industry, automotive, and aerospace industries due to its ability to produce complex three-dimensional geometries with good accuracy and surface finish. Despite the aforementioned advantages, the consumption of a large quantity of dielectric (especially hydrocarbon oils) poses a significant health and environmental hazard including respiratory and skin irritation issues. Further, the disposal of waste dielectric that contains a significant amount of metal particulates poses safety concerns. In order to comply with environmental safety standards, extensive filtration and treatment systems capable of handling huge amounts of dielectric waste need to be set up for their safe disposal. This leads to an increased energy consumption and hence higher operating cost for the machining process. Thus, there is a need to reduce the consumption of oil-based dielectrics without compromising their superior machining performance. Several techniques including dry and near-dry EDM have been developed to reduce the consumption of dielectrics. However, they have poor debris flushing capability. This research seeks to develop a technique that minimizes the consumption of dielectrics and also improves the flushing of debris from the inter-electrode gap.

A novel method of using atomized dielectric spray in EDM (Spray-EDM) to reduce the consumption of dielectric is developed in this study. The atomized dielectric droplets form a moving dielectric film up on impinging the work surface that penetrates the inter-electrode gap and acts as a single-phase dielectric medium between the electrodes. It also effectively removes the debris particles from the discharge zone. Single-discharge EDM experiments are performed using

three different dielectric supply methods, viz., conventional Wet-EDM (electrodes submerged in dielectric medium), Dry-EDM and Spray-EDM in order to compare the processes based on material removal, tool electrode wear and flushing of debris from the inter-electrode gap across a range of discharge energies. It is observed that Spray-EDM produces higher material removal compared to the other two methods for all combinations of discharge parameters used in the study. The tool electrode wear using atomized dielectric is significantly better than Dry-EDM and comparable to that observed in Wet-EDM. The percentage of debris particles deposited within a distance of 100 μm from the center of EDM crater is also significantly reduced using the Spray-EDM technique.

In order to understand and improve the debris flushing phenomenon in Spray-EDM, a model based on Computational Fluid Dynamics (CFD) is developed in this research. The debris flushing in Spray-EDM is investigated by developing models for three processes, viz., dielectric spray formation, film formation and debris flushing. The dielectric spray model developed to study droplet atomization and dielectric spray formation is based on the Discrete Phase Modeling (DPM) approach that solves the force-balance equations of the dielectric droplets in a Lagrangian reference frame. The range of spray system parameters including gas pressure and impingement angle that ensure formation of dielectric film on the surface are identified using this model. The film formation model makes use of the Eulerian Wall Film (EWF) approach to facilitate the mass and momentum transfer from the dielectric droplets to the film formed on the machining surface. This model is especially used, to determine the characteristics of the dielectric film including thickness and velocity. The debris flushing model utilizes the DPM approach to predict the trajectory of the EDM debris in the inter-electrode gap. The flushing ability in conventional EDM with stationary dielectric and Spray-EDM processes is investigated. It is observed that the characteristics of the dielectric film, viz., film thickness and velocity play a significant role in removing the debris particles from the machining region.

To my parents, for their love and support.

Acknowledgments

I would like to thank my adviser, Professor Shiv G. Kapoor, for providing the opportunity to work on this project. His constant guidance and encouragement over the course of this research were instrumental in the successful completion of the research objectives. I would also like to thank Post Doc, Dr. Deepak Marla, whose knowledge and support helped to overcome the challenges over the course of this research.

I gratefully acknowledge the use of facilities in the Frederick Seitz Materials Research Laboratory Central Facilities and the MechSE machine shop at the University of Illinois at Urbana-Champaign.

I have been fortunate to have seniors who have always been there to provide constant motivation and encouragement to overcome the technical challenges presented by this research. I thank Soham S. Mujumdar for sharing his knowledge through the numerous discussions we have had right from the start of this project. His eagerness to help the members in his research group is something that I would like to develop. I also thank Rajavasanth Rajasegar whose constant guidance and motivation during my graduate program helped me overcome the difficult phases of this research. I also thank Aravind Murali who has always been there to clarify all my doubts and provide guidance right from the day I decided to take up the graduate program at UIUC.

Finally, I would like to thank my parents, Pattabhiraman and Lalitha, and my sister, Priyadharshini, for their selfless love, support and encouragement throughout my life.

Table of Contents

List of Tables

List of Figures

List of Abbreviations

EDM	Electric Discharge Machining.
ACF	Atomized Cutting Fluid.
DPM	Discrete Phase Model.
EWF	Eulerian Wall Film.
MRR	Material Removal Rate.
EWR	Electrode Wear Rate.
PIV	Particle Image Velocimetry.
CFD	Computational Fluid Dynamics.
VOF	Volume of Fluid.
SST	Shear Stress Transport.
HOTR	Higher Order Term Relaxation.
TAB	Taylor Analogy Breakup.

List of Symbols

d_s Distance of tool electrode from spray impingement point on machining surface.

h_f Thickness of dielectric film.

v_f Velocity of dielectric film.

d_d Diameter of dielectric droplet.

v_d Velocity of dielectric droplet.

μ_d Dynamic viscosity of dielectric medium.

ρ_d Density of dielectric medium.

σ_d Surface tension of dielectric medium.

We Weber number.

Re Reynolds number.

Oh Ohnesorge number.

K_m, K, K_y Non-dimensional numbers governing spread-splash boundary.

α Spray impingement angle.

L_s Distance from the exit of droplet nozzle.

N_l Length of droplet nozzle.

d Vertical distance between droplet nozzle and machining surface.

d_{gap} Inter-electrode gap in EDM.

$\vec{F}_d$ Drag force on dielectric droplets exerted by carrier gas.

u Velocity of carrier gas.

g Acceleration due to gravity.

ρ	Density of carrier gas.
μ	Dynamic viscosity of carrier gas.
C_D	Coefficient of drag between carrier gas and dielectric droplets.
Y_{d_d}	Mass fraction of droplets with diameter greater than d_d.
$d_{d,mean}$	Mean diameter of dielectric droplets.
n	Size distribution parameter for droplets.
f	Frequency of ultrasonic atomizer.
P_o	Stagnant pressure of carrier gas.
P_s	Static pressure of carrier gas.
γ	Specific heat ratio of carrier gas.
M	Mach number for carrier gas.
v_{dn}	Normal velocity of dielectric droplet.
α_{min}	Minimum angle of impingement for spreading.
α_{max}	Maximum angle of impingement for spreading.
P	Pressure of carrier gas.
∇_s	Surface gradient operator.
$\dot{m}_s$	Mass source for dielectric droplets per unit wall area.
$\vec{\tau}_{fs}$	Viscous shear force at carrier-gas and dielectric film interface.
$\dot{q}_s$	Momentum source for dielectric droplets.
$\dot{m}_d$	Flow rate of dielectric droplet stream.
$\vec{v'}_f$	Film velocity in the inter-electrode gap.
v_{debris}	Velocity of debris particles.
$\vec{F'}_d$	Drag force on debris particles exerted by dielectric film.
ρ_{debris}	Density of debris particles.
d_{debris}	Diameter of debris particles.
F_T	Total force on the tool electrode.
F_H	Hydrodynamic force on sides of the tool electrode.

F_S Shear force on bottom of the tool electrode.

D Diameter of the tool electrode.

h_1 Film height corresponding to bottom of tool electrode.

V_o Open circuit voltage applied in EDM.

t_{on} Pulse-on time for single-discharge EDM.

I Circuit current for EDM.

R Resistance of EDM plasma channel.

Δ Difference in tool length before and after EDM discharges.

Chapter 1

Introduction

1.1 Background and Motivation

Electric discharge machining (EDM) is one of the most extensively used non-traditional machining process. It has been successfully employed in aerospace, automobile, and other industries for shaping, cutting, deburring and finishing [36, 37]. Due to its complex shape generation it has rapidly earned its place among many nontraditional machining processes. The process is based on material removal using electrical discharges between tool and workpiece that are submerged in dielectric, predominantly hydrocarbon oils. This leads to a significantly large amount of dielectric usage in comparison to the effective dielectric that plays a role in the discharge process, which is nearly equal to the volume of the inter-electrode gap. While the gap sizes in EDM are in the range of 1-50 μm, typical EDM machines use several gallons of dielectric during the operation. The consumption of oil-based dielectrics ranges from 160 to 3500 liters per year based on the size of the machine [38]. Oil-based dielectrics that are commonly used in EDM pose severe environmental hazards resulting from the disposal of such large amount of dielectric waste containing particulates of metals [5, 39, 40]. In addition, bacterial growth on the walls of the dielectric tank both in oil-based and water-based dielectrics can be hazardous to the operator when he comes in contact with the bacteria-laden dielectric [41]. Also, prolonged exposure to the vapors of dielectric produced during machining causes ataxia, drowsiness and convulsions [38]. Their use in conventional die-sinking EDM requires chillers for controlling the temperature of dielectric and extensive filtration systems for removing metal particulates,

further increasing the energy consumption of the process [40]. The energy utilized in the spark that removes material is typically less than 20% of the total electric energy input but the energy consumed by the dielectric system is as high as 50% [5]. Clearly, there is a need for techniques to reduce the dielectric usage in EDM and make it a clean and sustainable process.

In order to make EDM environmental friendly and less hazardous, Dry-EDM is often proposed. In Dry-EDM, liquid dielectric is replaced by a high velocity gaseous dielectric such as helium, argon, oxygen, nitrogen and air [42, 43, 44]. However, the major limitation of the process is its very low material removal rate [45]. Also, the debris re-attachment and odor of burning are other serious drawbacks of Dry-EDM [46]. To get both high material removal rate and good surface finish, a combination of liquid-gas (mist) dielectric has also been used by researchers [8, 47]. However, while the surface finish was seen to be slightly improved, the material removal could match with Wet-EDM (in which tool and workpiece are submerged in dielectric) only at very low discharge energies.

Irrespective of the dielectric used, the small inter-electrode gap also makes it extremely difficult to flush the debris. This ineffective removal of debris leads to arcing and abnormal discharges that makes flushing system an essential component of EDM process. With regard to flushing out the debris in EDM, techniques such as pressure flushing and jet flushing are commonly employed [48, 10]. Debris removal by passing dielectric through a hollow electrode to the inter-electrode gap has also been used in drilling holes [49]. In addition, techniques such as ultrasonic vibration of tool or workpiece [50] and application of magnetic field in the vicinity of inter-electrode gap [51] have recently been proposed to efficiently remove the debris. However, the use of such techniques requires an additional set-up for the operation of Electro Discharge machines. Also, there is possibility of tool electrode deflection due to the force exerted by the dielectric fluids with the jet flushing methods, especially for wire-EDM and micro-EDM applications. This compromises the accuracy of machining and also has a negative effect on the surface finish obtained.

2

The use of atomized dielectric in EDM is a viable and innovative solution both to reduce the consumption of dielectric and to efficiently flush out the debris. This idea stems from the recent investigations on the use of spray atomization for supplying cutting fluids in machining applications [24, 26]. Droplet impingement on a solid surface leads to the formation of a thin film. This thin film of cutting fluid penetrates the tool-chip interface improving the cooling and lubrication capabilities. This results in lower cutting forces and temperature compared to dry machining and flood cooling techniques. An improvement in tool life of about 40% is also observed [26]. Also, enhanced evacuation of chips from the machining region is observed with the atomization-based cutting fluid system. The concept of thin film formation due to spray atomization could also be exploited in EDM. The proposed method is different from the near-dry EDM technique in that the dielectric is made of only a single-phase (liquid) in the form of a thin film. On the contrary, in the near-dry EDM process, a mixture of liquid and gas that has lower viscosity and heat removal capability compared to a liquid dielectric is used. The lower viscosity of the dielectric does not constrain the expansion of the plasma channel, thereby resulting in lower explosion force during the discharge. This results in reduced material removal and flushing ability in near-dry EDM. While retaining the original single-phase dielectric properties, the use of a thin dielectric film that penetrates the inter-electrode gap to effectively flush the debris is a unique characteristic of the proposed Spray-EDM process compared to other existing EDM techniques.

The knowledge-base developed for the spray systems in traditional machining applications, however, cannot be directly applied to the EDM process. This is because for turning and micro-milling applications, the primary focus is to improve the cooling and lubrication properties of the cutting fluid via thin film formation. In Spray-EDM, the objective is to ensure the formation of a thin dielectric film that fills the inter-electrode gap completely since the presence of an air-gap adversely affects the discharge process and reduces the volume of material removed [8]. Also, the film must have sufficient velocity to effectively flush

the debris from the discharge region. The effect of spray parameters including dielectric flow rate, size of droplets, gas pressure and the distance between spray unit and machining surface on the film characteristics needs to be investigated for developing an efficient and sustainable Spray-EDM process.

1.2   Research Objectives, Scope, and Tasks

1.2.1   Research Objectives

The goal of this research is to develop a fundamental knowledge base that will enable the design and implementation of a Spray-EDM system that minimizes the dielectric consumption and improves flushing of EDM debris from machining region. To accomplish this, the specific objectives of the research are:

1. To understand the phenomena in Spray-EDM process including dielectric spray formation, spray-surface interaction and dielectric film formation on machining surface through computational modeling approach.

2. To study the flow characteristics of dielectric film on machining surface and its effect on the flushing of EDM debris from inter-electrode gap.

3. To design and develop a Spray-EDM test bed using the knowledge-base created with the aforementioned modeling studies and assess the performance of the Spray-EDM process.

In order to study the Spray-EDM process through Computational Fluid Dynamics (CFD) approach, three models, viz., (i) dielectric spray model, (ii) film formation model and (iii) debris flushing model are developed. The dielectric spray model is used to determine the velocity of the carrier gas and the dielectric droplets at various distances from the nozzle exit along its axis.The model is then validated by comparing carrier gas velocity against the experimental measurements obtained for a range of distances from the nozzle exit. Using the results

from the dielectric spray model, the range of impingement angles and distances from nozzle exit that ensure the droplet-surface interaction is within the spreading regime are estimated. The film formation model is developed using the Eulerian Wall Film (EWF) approach to estimate the film characteristics. The model is then validated by comparing film thickness against the experimental measurements obtained for a specific combination of spray system parameters. Using the validated film formation model, a three-dimensional profile of film is obtained and thickness and velocity for different combinations of gas pressure, impingement angle and distance from nozzle exit are determined. The debris flushing model is developed to predict the trajectory of debris by taking into account plasma pressure and radius, non-uniform debris size distribution, debris velocity, properties of workpiece material and actual topography of the machined crater. The trajectory of debris particles is computed using the Discrete Phase Model (DPM) that is based on solving force-balance equations of the individual debris particles in a Lagrangian reference frame. The model is then validated by comparing the distribution of debris around the crater with experimental measurements obtained from SEM images of the machined surface. The validated flushing model is used to evaluate the effectiveness of debris flushing using Spray-EDM for different combinations of spray system parameters.

Using the range of spray parameters identified through the aforementioned models, single-discharge EDM experiments are carried out for the Spray-EDM process and the performance is compared with Dry-EDM and Wet-EDM in terms of the volume of material removed, tool electrode wear and the distribution of debris around the EDM crater.

1.2.2 Scope of Research

This research focuses on the modeling and experimental investigation of the Spray-EDM process. Spray systems for machining applications typically involve droplets in the size rage of few microns to about 50 μm and this research will only

5

consider droplets within this range. Single-discharge experiments are considered in this research to eliminate variability associated with multiple discharge EDM experiments. Only the die-sinking EDM process is investigated in this research. The work material used throughout this research is Stainless Steel since it is has several engineering applications. The study is limited to using tungsten wire as the tool electrode since it is widely used and the focus of experimental research is to compare the performance of EDM process with different dielectric supply methods, viz., Wet-EDM (stationary liquid dielectric), Dry-EDM and Spray-EDM. The dielectric media used in the study are Chem Finish EDM 3001 Lite™ and air. The dielectric film used in Spray-EDM is only a few microns thick which is small compared to the lateral dimensions of the film. Hence, the spray-surface interaction and the dielectric film formation models in this research are based on thin film theory that is applicable to fluid films of thickness less than 300 μm [52].

1.2.3 Research Tasks

The objectives of this research are accomplished in three phases detailed below.

Phase I: The focus is to develop a physics-based model to understand the effect of parameters including dielectric fluid properties, droplet size, carrier gas pressure, distance of spray nozzle from machining surface and angle of impingement with respect to machining surface on dielectric film formation. This is achieved by the following sequence of tasks:

1. Develop the dielectric spray model to determine the velocity of dielectric droplets propagated by the carrier gas.

2. Conduct experiments to evaluate gas velocity to validate dielectric spray model.

3. Use the validated dielectric spray model to identify the combination of gas pressure, distance from spray nozzle and impingement angle that ensures

6

spreading of droplets on machining surface.

4. Understand the effect of spray parameters on film characteristics such as film thickness and film velocity by developing a model based on Eulerian Wall Film approach.

5. Validate film formation model by performing optical measurements of dielectric film formed on machining surface.

Phase II: The aim of the following set of tasks is to identify the effect of spray parameters on the flushing of debris particles from the machining region and also evaluate the performance of the Spray-EDM process.

1. Develop a physics-based model to simulate the movement of debris particles in the inter-electrode gap in EDM

2. Perform single-discharge EDM experiments to gather input data for debris flushing model and validate the model by analyzing SEM images of machined surface.

3. Use the validated debris flushing model to understand the effect of film thickness and film velocity on the motion of debris particles and compare with results from conventional EDM that uses stationary dielectric fluid.

4. Evaluate the performance of Spray-EDM process through single-discharge experiments and compare with conventional Wet-EDM (stationary liquid dielectric) and Dry-EDM techniques in terms of material removal, tool wear and flushing of debris particles.

1.3   Overview of Thesis

The remainder of the thesis is organized as follows. Chapter 2 presents a thorough literature review of topics relevant to this research including the mechanics of

macro and μ-EDM process and its applications, current techniques to improve the process efficiency and their limitations, Atomized Cutting Fluid (ACF) systems for machining applications, droplet impingement dynamics, modeling of dielectric fluid sprays and film formation, and modeling the flushing of debris from inter-electrode gap in EDM. Finally, the gaps in knowledge for developing Spray-EDM process are summarized.

Chapter 3 presents the fundamental concepts of the Spray-EDM process including the working principle and spray system components. A physics-based model to understand the formation of dielectric spray and its interaction with the machining surface is developed. First, the dielectric spray model is developed and validated to identify the combination of spray parameters for spreading regime. The spatial distribution and velocity of the dielectric droplets are determined using the Discrete Phase Model (DPM) approach. Then the film formation model is developed using the Eulerian Wall Film (EWF) approach. The validated model is used to determine the dielectric film thickness and velocity for different combinations of spray system parameters. The debris flushing model is developed to study the trajectory of debris particles in the Spray-EDM process using the DPM approach.

In Chapter 4, the validation of debris flushing model through single-discharge EDM experiments is discussed. Also, the range of spray parameters for enhanced debris flushing with Spray-EDM technique is determined. The performance of the Spray-EDM process is then evaluated through single-discharge experiments and compared with conventional Wet-EDM and Dry-EDM processes in terms of volume of material removed, tool wear and flushing of EDM debris from machining zone.

Chapter 5 presents the conclusions reached through the current research. The potential areas of future work in this field are also suggested.

Chapter 2

Literature Review

The overarching objective of this research is to develop a novel EDM technique that not only reduces the consumption of dielectric fluids but also improves the performance of the EDM process. In this regard, it is important to understand the mechanics of the EDM process including material removal mechanisms and debris flushing. Also, the current techniques used to improve the process performance and efforts taken to make the EDM process more sustainable need to be discussed. The contents of this chapter have been organized to facilitate a thorough understanding of the aforementioned topics. Section 2.1 discusses the fundamentals of EDM process including its advantages, limitations and applications. Section 2.2 provides a review of the current techniques used to reduce consumption of dielectric fluids along with the limitations of each method. The significance of debris flushing in EDM and available literature on modeling this phenomenon are discussed in Section 2.3. Section 2.4 discusses the fundamentals of atomization-based spray systems and its applications in micro-machining and machining Titanium alloys. In order to understand the interaction between dielectric spray and the machining surface in EDM, a brief overview of spray impingement dynamics and film formation is also provided in Section 2.4. This is followed by a summary of existing experimental and modeling approaches to study the film formation phenomenon in Section 2.5. The final section identifies the gaps in knowledge to develop an efficient Spray-EDM process.

2.1 Mechanics of the EDM Process

Electrical Discharge Machining is a complex process that involves several phenomena such as dielectric breakdown, plasma generation and discharge, melt-pool formation, and ejection of work material in the form of debris particles. A number of parameters affect the performance of the EDM process. Figure 2.1 shows the critical parameters in EDM and how they affect the process performance. In order to develop a novel EDM technique that aims to improve process performance, it is pertinent to understand both the material removal mechanism and the flushing of debris particles. The flushing of debris deals with how the material is removed from the inter-electrode gap to prevent short-circuiting [1].
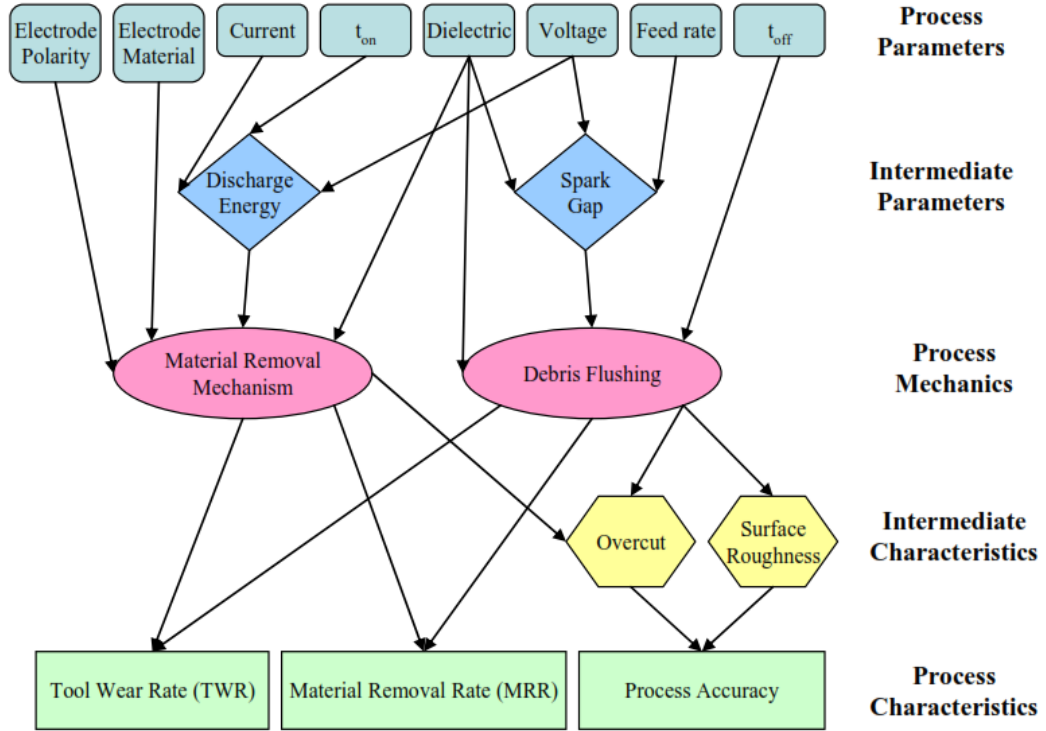
Figure 2.1: Schematic of EDM parameters [1].

Material removal in EDM

In EDM, the material removal is due to controlled erosion of work material by the use of electrical discharges. The volume of material removed in a single spark ranges from 10^{-6} to 10^{-4} mm^3 and is repeated for about 10000 times per second, resulting in considerable material removal over time [2]. The material removal in EDM is schematically described in Fig. 2.2. The electrically conductive electrodes (workpiece and tool) are separated by a very small distance, typically of the order of few tens to hundreds of microns, with a dielectric medium between them. A high voltage (around 200 V) is applied between the electrodes. Break down of the dielectric medium occurs when the resulting electric field across the gap given by $E = V/d_{gap}$ is greater than the dielectric strength of the medium, which is about 38 MV/m for deionized water [53]. The breakdown produces heating, melting of the electrodes and subsequently results in material removal.
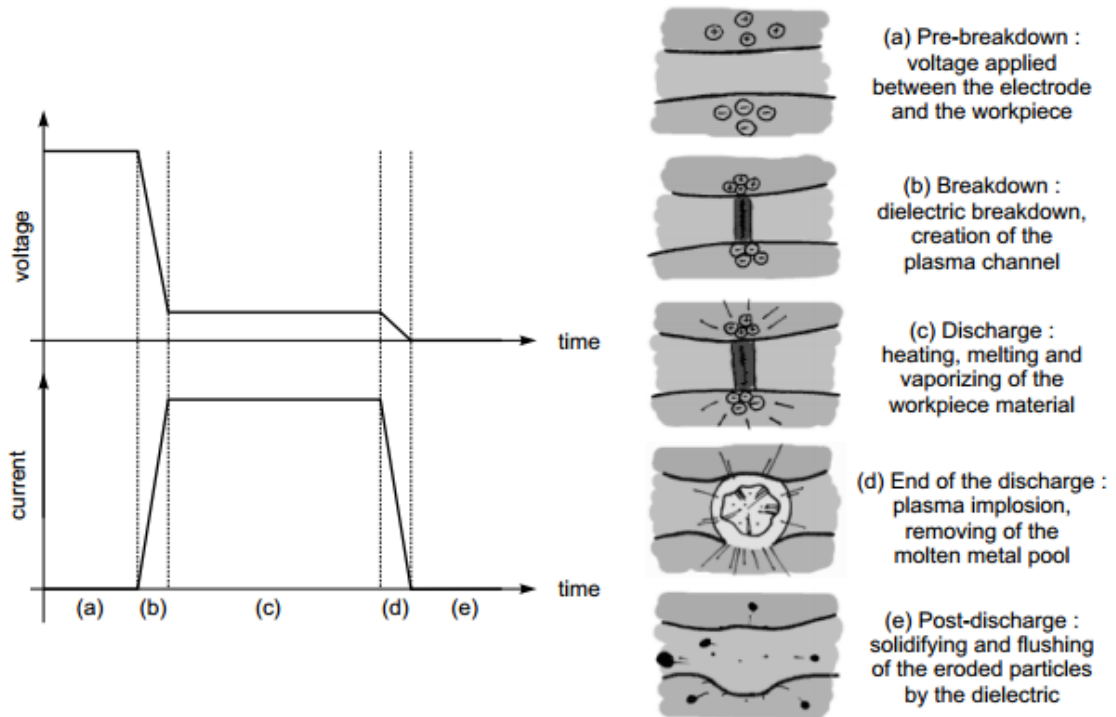
Figure 2.2: Schematic of material removal in EDM [2].

In order to comprehend the mechanism by which the breakdown of dielectric

11

medium occurs, it is important to understand the concept of streamer. A streamer is a narrow channel of weakly ionized medium. A positive streamer originates from the anode while a negative streamer starts from the cathode. These two types vary significantly in terms of their structure and speed of propagation, especially in high density media such as liquid dielectrics [2]. The positive streamer(Fig. 2.3) has a filamentary appearance and the negative one has a thicker structure. The propagation speed of the former is about 1 to 10 km/s while that of the latter is around 100 m/s. Figure 2.4 shows the mechanism of streamer formation within the inter-electrode gap. The discharge process begins with the formation of a streamer from a primary avalanche of electrons and ions. This avalanche is created in a lower density region (such as a bubble) within the inter-electrode gap since the high density of the liquid dielectric prevents the propagation of electrons in the liquid phase. The primary avalanche within the bubble heats the liquid dielectric in front of it which results in the growth of the bubble and also formation of new bubbles. These bubbles in turn promote the formation of secondary avalanches and the cycle of vaporizing liquid dielectric and growth of avalanche results in the formation of a streamer within the inter-electrode gap. The width of the ionized channel increases when the streamer reaches the other electrode, thereby resulting in a spark discharge between the electrodes. This process is accompanied by intense emission of light.

The formation of the highly ionized plasma channel from the streamer is followed by a drastic reduction in the voltage across the gap and sudden spike in the current. The bombardment of the ions from the plasma channel on the electrodes results in intense heat generation on their surfaces. This heat is sufficiently high to vaporize some of the material and also melt the material in the regions close to the plasma channel, creating a molten pool of metal on the surfaces (Fig. 2.5). However, the fraction of total material removed by vaporization is only about 1.15 to 4.1 % and the material is predominantly removed by melting [54]. The size of the melt pool increases with time as the radius of plasma channel keeps increasing during the discharge process. When the voltage between the electrodes is turned
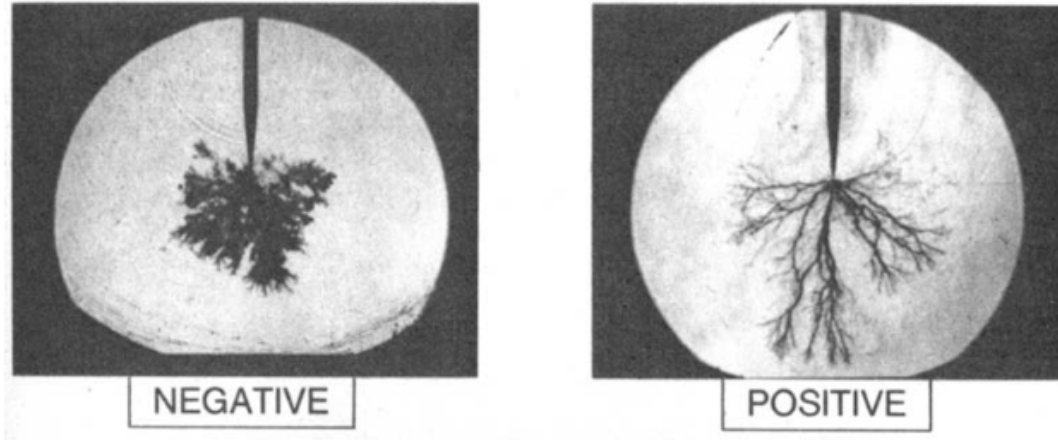
Figure 2.3: Shadowgraphs of negative and positive streamers in oil [3].
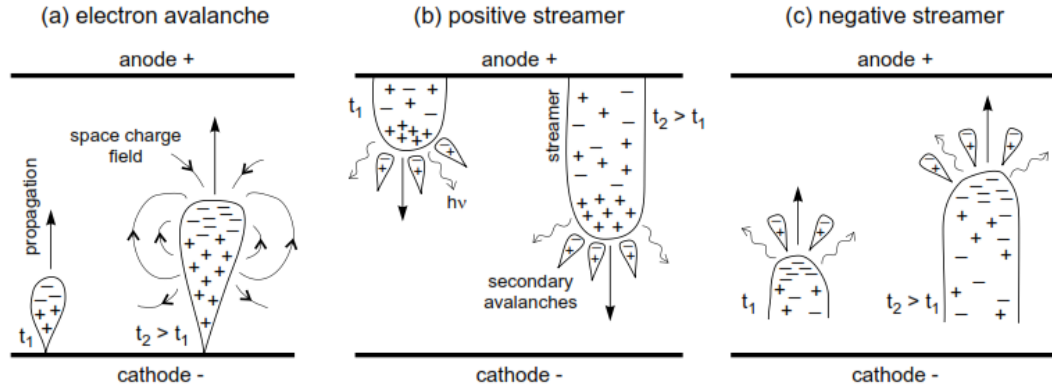
Figure 2.4: Mechanism of streamer formation [2].

off, the plasma channel implodes due to the pressure exerted by the surrounding dielectric medium. This is followed by the ejection of molten metal from the melt pool by a complex process that involves forces from electrodynamics, thermodynamics, and hydrodynamics [55]. The ejected metal solidifies on contact with the dielectric medium in the form of globules. At the end of this process a crater is formed on both the electrode surfaces, the size of which depends on EDM parameters such as discharge energy. The selection of the tool and work material and their polarity during EDM process can be tailored such that the amount of material removed from the workpiece is significantly higher than that removed from the tool electrode.

13
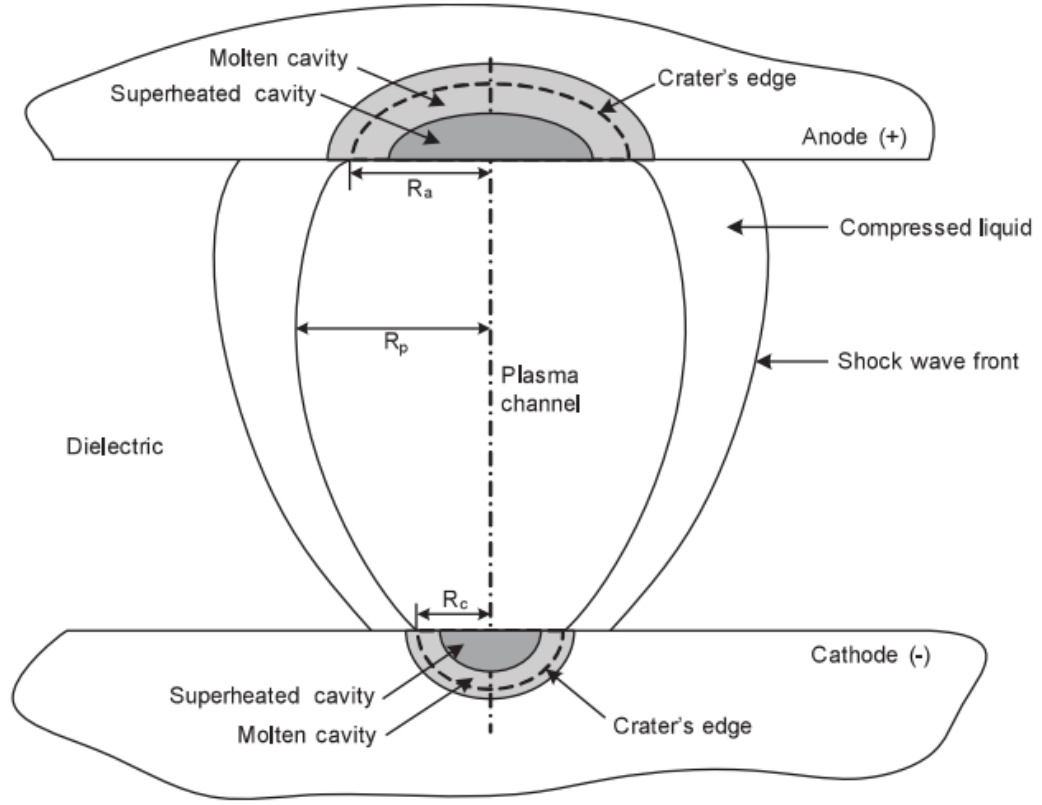
Figure 2.5: Schematic of the melt pool formed during the EDM process [4].

Role of dielectric fluid in EDM

Some of the commonly used dielectrics in EDM are water, hydrocarbon oils such as kerosene, and gases such as oxygen, helium and argon. Though water has the advantages of having low viscosity, fire resistance, and low cost, the control of spark gap is effectively achieved by using hydrocarbon oils [56]. Hence oil-based dielectrics are predominantly used in machining applications. The dielectric fluid performs the following functions during the EDM process [2].

1. Ensures that a high pressure plasma channel is formed within the inter-electrode gap which exerts greater force on the melt pool when the plasma collapses at the end of discharge.

2. Reduces the temperature at the tool and workpiece surfaces.

3. Solidifies the ejected molten metal from the electrodes into globule-shaped debris particles.

4. Flushes the debris particles from the machining zone.

The role of the dielectric as discharge medium between the electrodes was discussed extensively in the previous section. Careful selection and circulation of dielectric between the electrodes is necessary for control of electric spark and efficient performance. The ability of the dielectric to flush away the debris particles is critical to achieving the desired work surface finish and accuracy. The accumulation of particles in the gap will increase the electrical conductivity of the dielectric in the regions where the particles are concentrated. This leads to the concentration of spark discharges in these regions leading to enhanced material removal compared to the other parts of the work surface, thus resulting in poor control over the material erosion process during EDM. The effect of debris on the discharge is more significant in μ-EDM due to smaller gap distances employed in the process compared to macro-EDM. Hence effective flushing of the debris is crucial to improving the efficiency and stability of the EDM process [1]. It has been determined that effective flushing of debris enhances the efficiency of the process and reduces machining time by a factor of six [57]. Also,important EDM performance measures such as tool wear, surface roughness, and depth of recast layer are affected by flushing mechanisms adopted during machining [58, 59, 60]. In order to ensure stable and uniform material removal, the dielectric fluid must have the ability to penetrate the inter-electrode gap and flush debris. Some of the commonly used flushing methods are through-the-tool flushing, vacuum flow, vibration-assisted flushing, jet flushing using nozzles, and flushing by imparting relative motion between tool and workpiece [61].

However, the use of large quantity of dielectrics, especially hydrocarbon oils has inherent disadvantages of having a harmful effect on the EDM operators. The prolonged exposure to noxious smoke, aerosols and vapors of the dielectric oil produced due to the high temperature in the discharge gap during machining

15

causes severe respiratory and skin irritation issues [41, 62]. Also, the disposal of these dielectrics along with metal particulates also has serious environmental impact [5, 39]. Their use in conventional die-sinking EDM requires chillers for controlling the temperature of dielectric and preventing a fire hazard [63]. In order to comply with environmental standards extensive filtration and treatment systems capable of handling huge amounts of dielectric waste need to be set up for their safe disposal. This leads to an increased energy consumption and hence higher operating cost for the machining process. In order to overcome the aforementioned issues, several techniques have been developed to minimize the consumption of dielectrics in EDM. These are thoroughly discussed in the next section along with the disadvantages of each method.

2.2 Techniques to Minimize Consumption of Dielectric Fluids in EDM

Some of the factors that influence the environmental aspect of EDM are energy consumption in the process, exposure to aerosols and consumption of large quantity of dielectric [64]. These are schematically shown in Fig. 2.6. The consumption of kerosene as dielectrics in medium and large EDM machines used for manufacturing high precision automation parts was estimated to be roughly between 160 liters to 3500 liters per year [38]. This results not only in increased operating costs for the industry but also in harmful environmental effects. Toenshoff. et. al (1996) [62] found that mineral oils produced hazardous fumes such as polycyclic aromatic hydrocarbons, benzene and mineral aerosols. In order to overcome these limitations, several techniques such as dry EDM, near dry EDM and EDM using water have been developed to reduce consumption of hydrocarbon oils as dielectrics and are discussed in detail in this section.
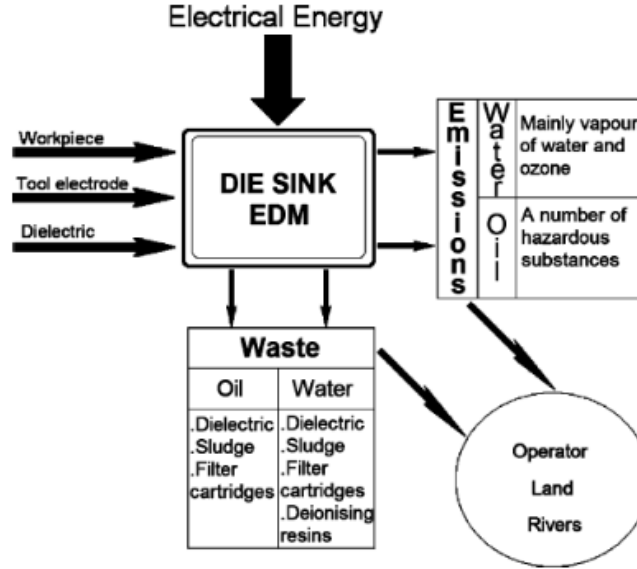
Figure 2.6: Environmental impact of EDM process [5].

Dry EDM

A thin-walled tube is used as the tool electrode and a gas such as air, oxygen or argon is fed at high pressure through the tool into the inter-electrode gap. The gas reduces the temperature in the machining region and also helps to remove debris particles produced by the discharges. It is environmentally clean because there is neither generation of hazardous gases nor waste from dielectric fluid. A schematic of the Dry-EDM process is shown in Fig. 2.7. The process is characterized by good material removal rate (only when oxygen is used), thinner white layer on machined surface, absence of electrolytic corrosion of workpiece, smaller discharge gap, smaller residual stresses on the machined surface, and compact size (due to absence of a dielectric fluid tank) [65]. Dry EDM also results in better machining accuracy, especially in the case of wire EDM because of the reduced forces on the electrode wire compared to oil-based dielectrics that prevents excessive deflection of tool. The material removal rate is lower compared to oil-based EDM except when using oxygen because the lower viscosity of the gas phase generates lower energy density per pulse and explosive force during the process [46].

Yu. et. al (2004) [66] studied the machining of cemented carbide using Dry-EDM
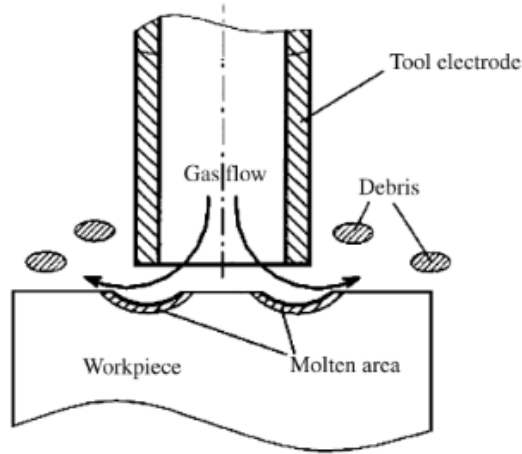
Figure 2.7: Schematic of the Dry-EDM process [6].

milling, oil EDM milling and die-sinking EDM using a copper electrode. High pressure oxygen was fed through the tool electrode as dielectric. It was observed that the work material removal rate in case of Dry-EDM was about six times that of oil EDM for the same discharge energy and they attributed the enhanced material removal to the oxidation reaction that occurs at the inter-electrode gap during the discharge process. The thermally-activated oxidation reaction at the tool- workpiece interface causes the material to melt and vaporize explosively, a phenomenon similar to that observed in plasma jet cutting process [7]. Precise machining is difficult when oxygen is used since the explosive oxidation reaction in the gap cannot be controlled by the electrical energy supplied across the electrodes. In order to overcome this limitation, Kunieda et. al. (2003) [7] explored the possibility of using a *quasi-static explosion mode* that has material removal rate in between the normal discharge and explosive mode but offers much better control over the process. These modes are schematically shown in Fig. 2.8. The material removal increased when the discharge energy density exceeded a threshold value and was comparable to that achieved during high speed milling of quenched steel by milling machine. The machining accuracy improved when the gas was sucked through the tool electrode instead of being jetted out since it controlled the diffusion of plasma in the radial direction within the gap.

Normal	Quasi-explosion	Explosion
No chemical reaction when pulse generator is turned off.	No chemical reaction when pulse generator is turned off.	Chemical reaction continues even if pulse generator is turned off.
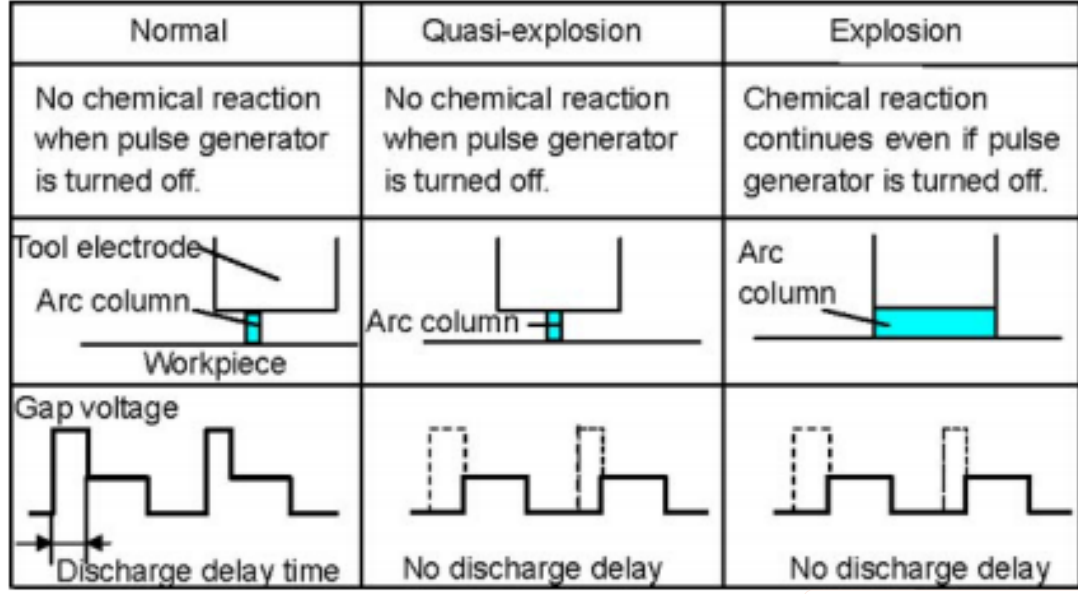
Figure 2.8: Mode transition observed in Dry-EDM [7].

Dry-EDM was also employed to drill holes in hard-to-machine materials with a tubular copper electrode using argon or helium as the dielectric [67]. Kao. et. al. (2006) [46] used air as dielectric to machine thin workpieces of brass and aluminum with wire EDM process and compared the performance with water-based EDM. The material removal rate using water was about 14 mm^3/min and that observed in Dry-EDM was only 3.8 mm^3/min.

The increased material removal in Dry-EDM is not observed for all work materials and dielectric gas combinations and is limited to machining steel with oxygen [6]. Also, in Dry-EDM and the machined surface has a higher roughness compared to oil EDM due to the poor flushing of debris which makes them re-adhere to the surface after removal [47]. This is because the molten debris move with an almost constant velocity in air and do not re-solidify until they come in contact with the electrode-surface. On the contrary, in oil-based EDM the debris are decelerated due to the bubbles and solidify into a spherical shape due to surface tension [68] and are flushed from the gap. Dry EDM is also not very effective when large depth of cuts are employed or in finishing operations since there is no sufficient flow of gas in the side gaps between the machining surface and tool(see

Fig. 2.9). Dry-EDM is also characterized by frequent short circuiting since the gap distance is small and this has a significant effect on the productivity of the process [45]. In the case of dry-wire EDM, Kunieda and Furudate (2001) [69] observed lower material removal rate compared to oil-based EDM and also a large number of streak marks on the finished surface. This was caused by the wire feed turning back and forth frequently due to short-circuiting. Li et. al. (2004) [70] observed that positive polarity of electrodes resulted in better machining performance in Dry-EDM and that a high pressure must be imparted to the dielectric gas in order to strengthen the de-ionizaton process in between the discharges. This is not suitable for certain machining applications such as $\mu - EDM$ where excessive pressure might damage either the tool or the machined features.
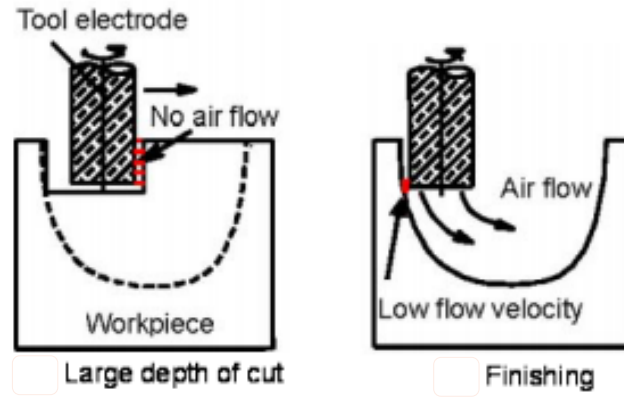
Figure 2.9: Scenarios in which Dry-EDM is not effective [7].

Near-dry EDM

Recently, a 'near-dry' EDM process has been developed that utilizes a combination of liquid and gas (mist) dielectric medium [8, 47]. An MQL-type fluid dispenser is used to generate a liquid-gas mixture as the two-phase dielectric medium that is supplied to the discharge zone by a high-pressure air stream through a nozzle system.

Kao et. al. (2007) [8] compared the performance of dry, near-dry and Wet-EDM processes for wire EDM and EDM drilling operations with Al6061 as work

material. Compared to the flow rate of 107 ml/min used for the Wet-EDM, only 21 ml/min was used in the near-dry EDM process. The MRR envelopes for the three processes are shown in Fig. 2.10. The MRR for near-dry process was found to be higher than that observed in Dry-EDM for all combinations of discharge duration and pulse interval time, but it was still significantly lower than Wet-EDM (where workpiece is submerged in a liquid dielectric) in the region of high discharge energy (pulse interval time less than 250 μs). Also, the frequency of wire breakage in near-dry process was higher than Wet-EDM because of the reduced heat-removal capability of the water-air mixture compared to single-phase liquid as dielectric. At high discharge energies, liquid dielectric generates larger explosion force due to its higher viscosity compared to liquid-gas mixture that has lower viscosity due to mixing with gas phase [70].
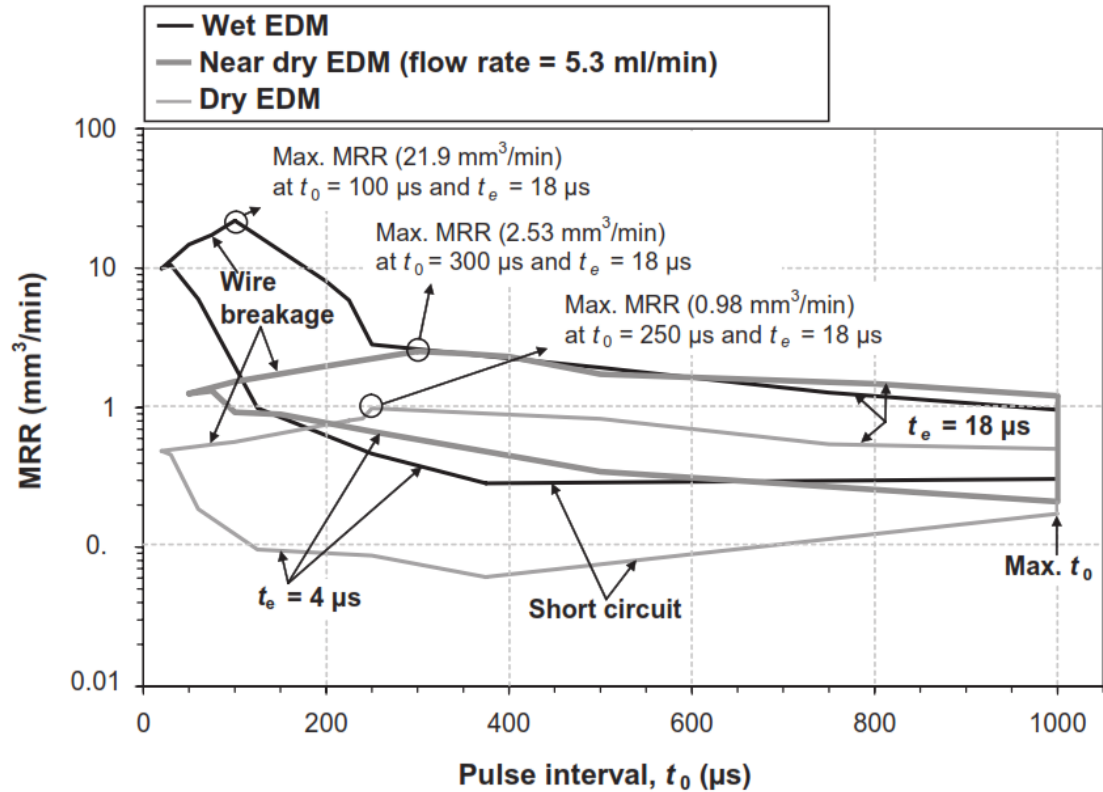
Figure 2.10: Comparison of MRR envelopes for three processes with gap current of 25 A and gap voltage of 45 V [8].

The comparison of MRR for different flow rates of the liquid dielectric in near-

dry EDM is shown in Fig. 2.11. It is observed that high water flow rate improves the MRR due to better cooling, higher dielectric fluid viscosity and improved debris flushing.
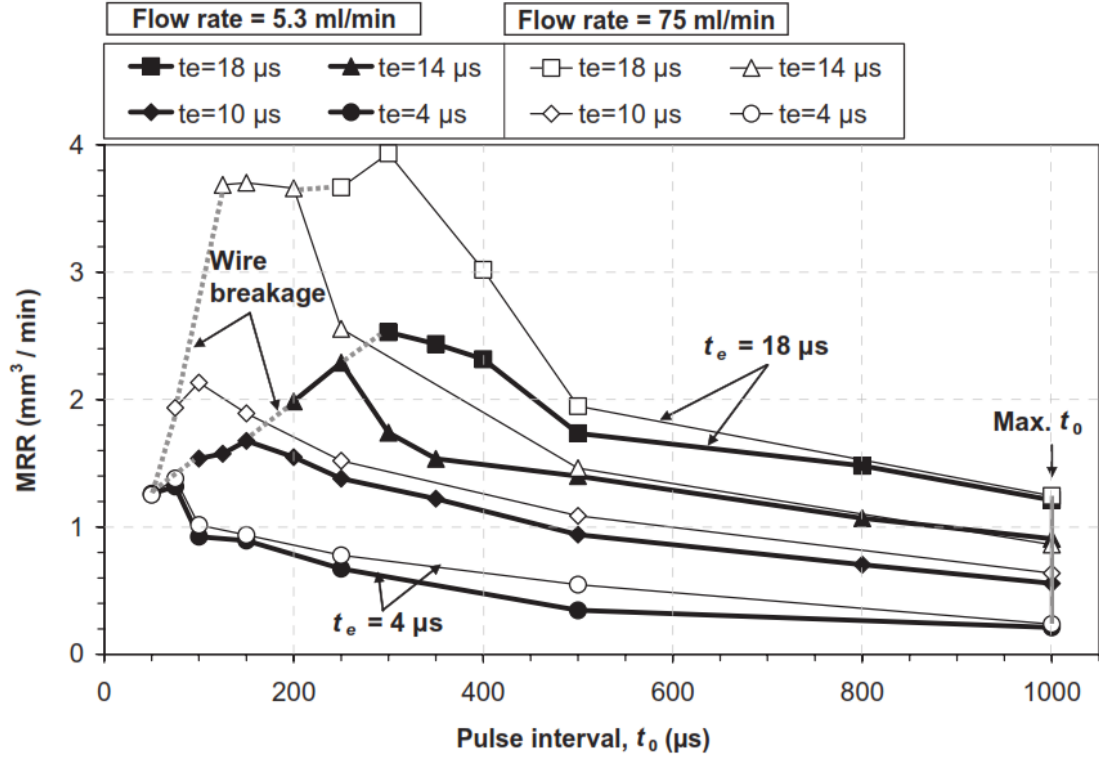
Figure 2.11: Comparison of MRR envelopes for different flow rates with gap current of 25 A and gap voltage of 45 V [8].

The profile of EDM drilled holes using the three processes is shown in Fig. 2.12. The time taken to drill a hole of depth 1.27 mm was found to be 428 s, 11 s and 13 s for the dry, wet and near-dry EDM processes, respectively. It is observed that near-dry EDM produces straight holes with sharp edges compared to the other two processes.

Despite the reduction in consumption of dielectric fluids in near-dry EDM, the mixture of gas and liquid is less effective than single-phase liquid dielectric in removing debris particles from the machining region, resulting in frequent short-circuiting. Also, the electrode wear in the near-dry EDM is higher than that obtained in the Wet-EDM process.
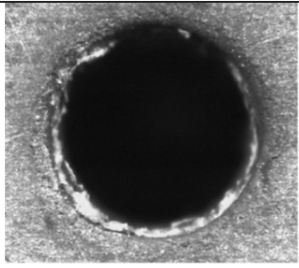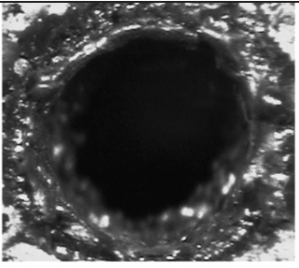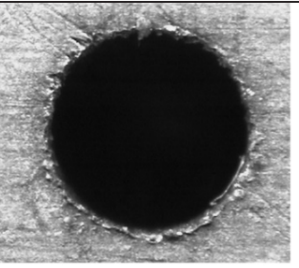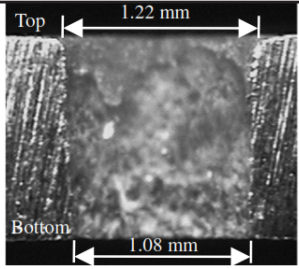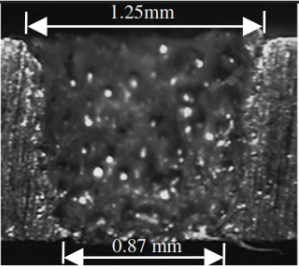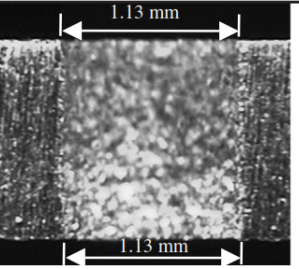
	Wet	Dry	Near dry
Top view			
Cross-Sectional side view	Top 1.22 mm / Bottom 1.08 mm	1.25mm / 0.87 mm	1.13 mm / 1.13 mm
Drilling time (s)	11	428	13

Figure 2.12: Optical micrographs of holes with gap current of 10 A and gap voltage of 60 V [8].

EDM using water

Pure water and water with additives (predominantly organic compounds) have been explored to replace hydrocarbon oils as dielectrics in the past several years. The idea stemmed from the research of Jeswani (1981) [71] where performance of distilled water and kerosene was compared. It was observed that a higher material rate was achievable using distilled water compared to kerosene, especially in the range of high discharge energy $72 - 288$ mJ. This is because the water dipoles directed into the electric field accelerate spark formation in water. The erosion process in water-based EDM systems possess higher thermal stability and higher discharge energy can be achieved. This is attributed to the fact that the specific boiling energy of water-based dielectrics is about eight times higher than oil-based ones and the boiling occurs at a lower temperature [72]. Also, the deposition of the tool material on the machined surface was less with distilled water. Lower tool wear ratio and good surface finish were also observed but the machining accuracy was poor. However, distilled water as a potentially effective dielectric medium

23

is restricted only to high discharge energy conditions. In the case of electrodes immersed in a tank of water, energy is wasted due to the leakage of charges from electrodes to surrounding dielectric. This is a significant issue with EDM circuits having a relaxation type pulse generator.

Chen. et. al. (1999) [9] observed that distilled water resulted in higher material removal compared to oil in machining Ti-6Al-4V. The decomposed carbon from the hydrocarbon oil formed TiC on the surface and reduced material removal since TiC has a higher melting point. However, the average size of debris particles was greater when distilled water was used compared to kerosene. This can have a profound impact on the process since the frequency of short-circuiting in EDM increases with the debris concentration, especially when an ineffective flushing mechanism is employed. Also, the density of micro-cracks on the machined surface was higher with water-based EDM which decreases the fatigue strength of the machined parts. This will severely limit the part's functionality(see Fig. 2.13). Kranz. et. al. (1990) [73] observed severe toughness losses for high-strength tool steels after machining with water-based dielectrics due to the combined effect of changes in the micro-structure of the work material and micro-cracks.

Konig and Jorres [74] studied the feasibility of adding organic compounds with large molecular weight such as ethylene glycol, glycerine, polyethylene glycol, dextrose, and sucrose with water. The increase in viscosity of water with these additives and the decomposition of these compounds during the spark discharge to produce high pressure gaseous result in a greater material removal per discharge. Water-based dielectrics with glycerine concentration between 50 and 60% is well-suited for roughing operations which involve long pulse durations, duty factors and discharge currents.

Although water as a dielectric in EDM results in a better machining performance in some scenarios, hydrocarbon oils are superior in a wide range of machining conditions [5]. In general, the lower viscosity of water compared to oil provides a lesser restriction of the plasma channel, thereby decreasing the energy density and the subsequent material removal. The higher energy required to heat
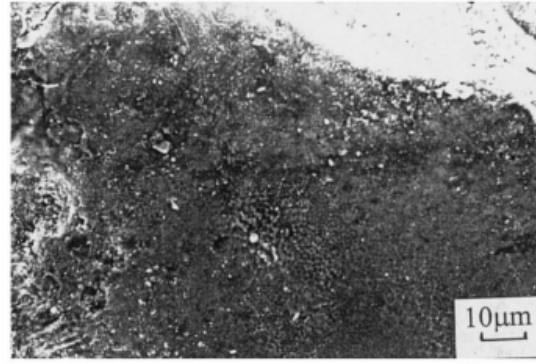
Kerosene
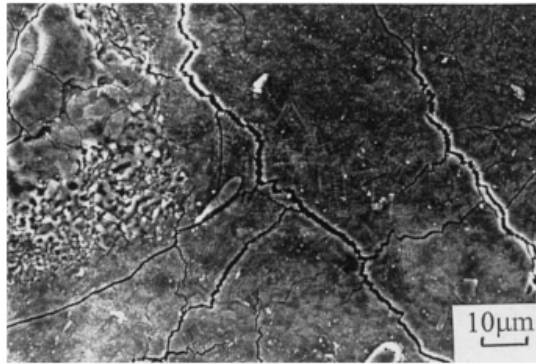
Distilled water

Figure 2.13: SEM images of crack distribution on EDMed surface [9].

and vaporize the water in the discharge gap results in lower gas pressure, which inhibits the complete removal of material from the melt pool. Hence, there is a need to reduce the consumption of hydrocarbon oils as dielectrics in EDM without affecting the process performance.

The consumption of hydrocarbon oils as dielectrics in the EDM process is minimized through Dry-EDM, near-dry EDM and using water as dielectric. However, these techniques have a lower material removal capability compared to the conventional EDM techniques. Also, apart from the quantity of the dielectric used in the EDM process, one of the important aspects to be addressed is the effective removal of the debris from the inter-electrode gap. An overview of the current techniques to improve the debris flushing in EDM process is presented in the next

section.

2.3 Debris Flushing in EDM

A good flushing mechanism has a significant effect on the performance of EDM process. A higher material removal is achieved with an effective flushing method because of reduction in frequency of abnormal discharges that occur when debris are present in the inter-electrode gap. Also, in order to achieve uniform material removal from the part, the concentration of debris in a particular region mus be avoided and is achieved by a proper flushing system. Flushing also impacts the tool wear, crack density and recast layer thickness on the machined surface which can be minimized by an optimal flushing method [59]. Benedict [61] classified the most common flushing methods into five categories, viz., through-the-tool flushing, jet flushing, relative motion between tool and workpiece, vibration-assisted, and magnetic flushing. These techniques along with their limitations are discussed in detail in this section.

2.3.1 Techniques to improve debris flushing

Jet flushing

This is the simplest and most widely used method where dielectric fluid is ejected from a nozzle placed adjacent to the discharge gap at a high pressure. The debris are carried out of the inter-electrode by the flow of the fresh fluid. Wang at. al. (2005) [75] studied the jet flushing of dielectrics for machining tungsten carbide and found that the machining stability decreased due to turbulence in the small inter-electrode gap, especially for higher flushing pressures. Also, the uniformity of debris distribution in the vicinity of the electrical discharges is not ensured due to a fixed flow field of the dielectric fluid [10] which results in uneven gap distance, thereby reducing machining accuracy. In order to overcome

this limitation, Masuzawa et. al. (1992) [10] developed a sweeping-jet method in which two nozzles are placed on either side of the machining region and positions are dynamically changed during the discharges to achieve uniform debris distribution. As seen from Fig. 2.14, the surface flatness using the sweep-jet method was better than normal jet flushing.
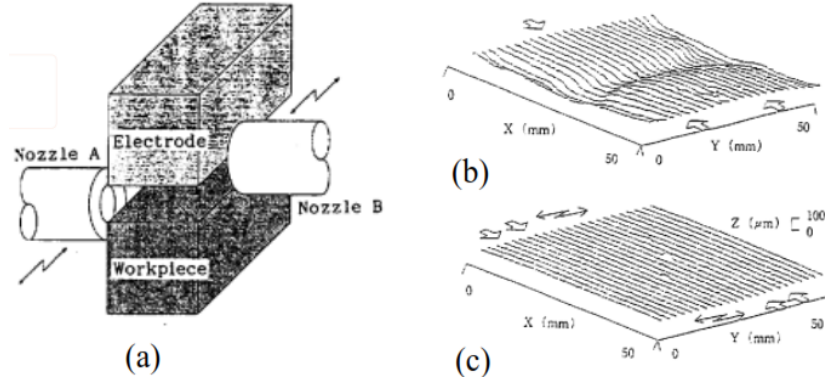
Figure 2.14: (a) Sweep-jet flushing schematic, Surface profile of workpiece using (b) normal jet flushing and (c) sweep-jet flushing [10].

Jet flushing is also not preferable for wire-EDM applications and $\mu - EDM$ because the impact force of the dielectric jet from the nozzle can deflect the wire or tool and compromises the machining accuracy.

Tool movement

The plunging movement of the tool electrode during discharges has been studied in the past [21, 76, 77, 78]. Cetin et. al. (2003) [21] investigated the effect of the electrode jump parameters such as jump height and jump speed on the flushing performance and material removal rate in die-sinking EDM. The material removal increased with tool plunging motion due to enhanced circulation of the dielectric and removal of debris.

Since the flow of the dielectric is not well controlled by a simple upward or downward movement of the tool electrode, Masuzawa et. al. (1983) [79] devised a movement of the tool electrode in the workpiece cavity using a controller and motor system that *draws in* fluid from one side and *pushes out* through the other

side. The gap between the tool and the side and bottom walls are fed back to the controller to define an optimal tool movement path. However, this method is not efficient for machining shallow features since the tool movement in such as case will not be able to *draw in* the dielectric. Also, time for the tool movement does not directly contribute to the material removal and increases the machining time.

Guu and Hocheng (2001) [11] developed a rotary EDM method in which the workpiece was rotated during the discharge process to improve the circulation of dielectric fluid within the gap. The material removal rate in this technique was almost twice as high as that observed in the conventional method (see Fig. 2.15). The centrifugal forces in rotary EDM flushed the debris efficiently from the discharge gap, thereby avoiding abnormal discharges and enhanced machining performance. Lower surface roughness and uniform residual stresses on the recast layer were also observed in this method. However, this method is only suitable for machining axially symmetric features in the workpiece.

A similar approach of rotating the tool electrode instead of the workpiece was developed by researchers [80, 81, 12, 82]. Soni and Chakraverti (1994) [12] observed that material removal was higher with rotation of the tool electrode due to improved flushing action and sparking efficiency. This technique can be used to machine axially non-symmetric features too. However, the surface roughness and the tool wear rate were observed to be higher in comparison to stationary electrode (see Fig. 2.16).

Vibration-assisted flushing

The application of low frequency vibration to the electrodes during the EDM process has been investigated in the past [83, 84, 14, 85, 13]. Ghoreishi and Atkinson (2002) [13] compared the performance of tool vibration and rotation-assisted EDM process and found that an increase in MRR upto about 35% can be achieved by synchronizing the rotation and vibration of the tool electrode(see Fig. 2.17). Prihandana et. al. (2011) [83] studied the effect of low frequency vibrations of
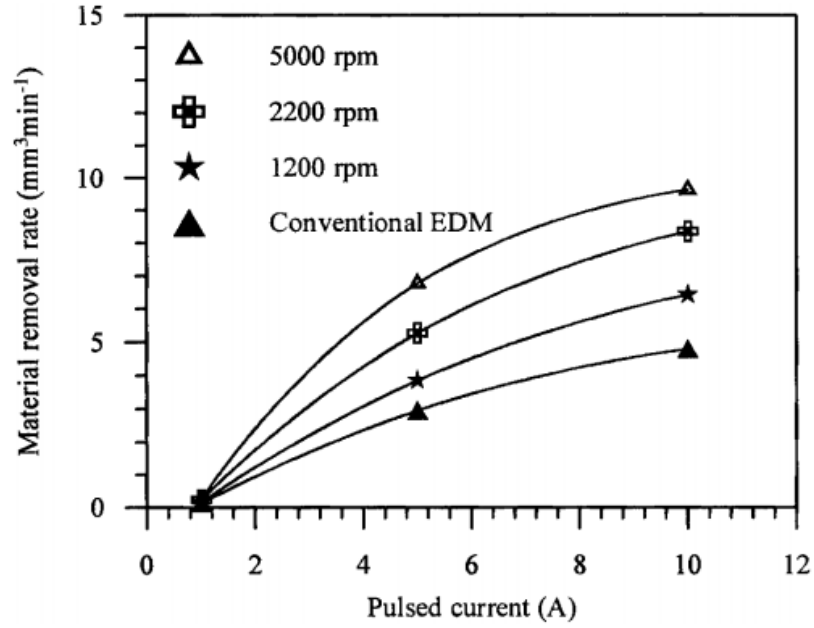
(a)
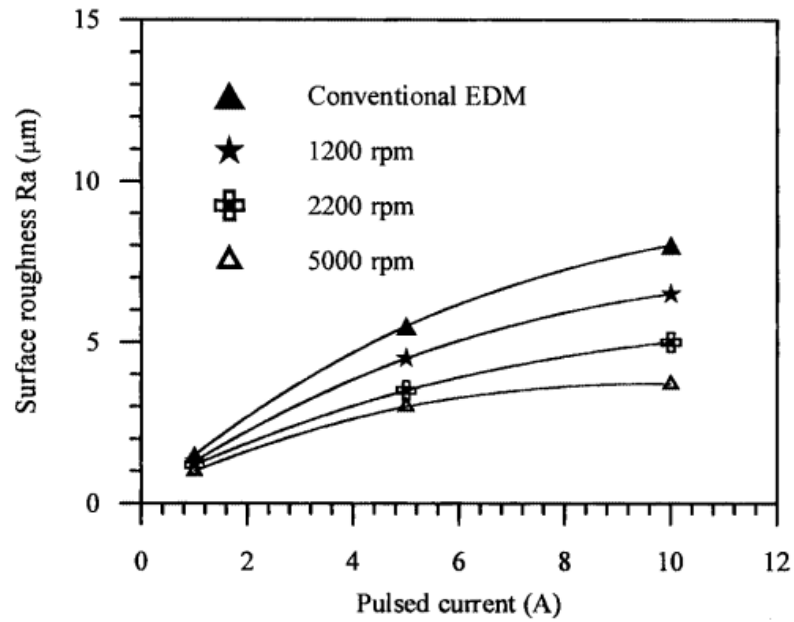
(b)

Figure 2.15: Comparison of conventional and rotary EDM in terms of (a)MRR and (b)surface roughness [11].

the workpiece on the material removal rate, surface roughness and tool wear. The MRR in vibration-assisted EDM was about 25% higher than conventional method because of the enhanced circulation of the dielectric within the discharge
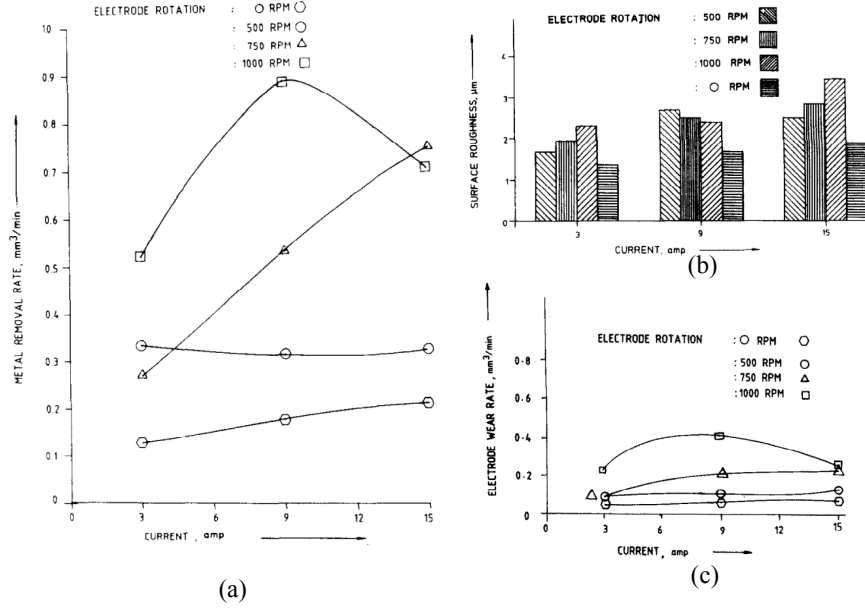
Figure 2.16: Comparison of stationary and rotating electrode in terms of (a) MRR, (b) Surface roughness and (c) Tool wear rate [12].

gap which promoted debris flushing. The MRR was significantly affected by the amplitude and the frequency of vibration. The surface roughness was lower than conventional EDM but only at lower frequencies and amplitude of vibration. High frequency vibrations had a detrimental effect on the surface finish and also the tool wear during EDM. Jahan et. al. (2010) [14] investigated the drilling of deep micro-holes in tungsten carbide by using low frequency vibration of the workpiece. There was a significant improvement in machining stability due to the vibrations as is evident from the number of short-circuit pulses shown in Fig. 2.18. The continuous change in the dielectric fluid pressure within the gap generates a periodic suction and pumping action that circulates uncontaminated fluid into the machining zone. The effective flushing of debris prevents the abnormal discharges and improves the discharge process. A marginal increase in MRR and a lower electrode wear rate were also observed with low frequency vibrations(see Fig. 2.19). As observed in previous studies, very high frequency and amplitude of vibration affected the micro-hole's surface quality and accuracy.

Ultrasonic vibrations have also been used to improve the machining perfor-
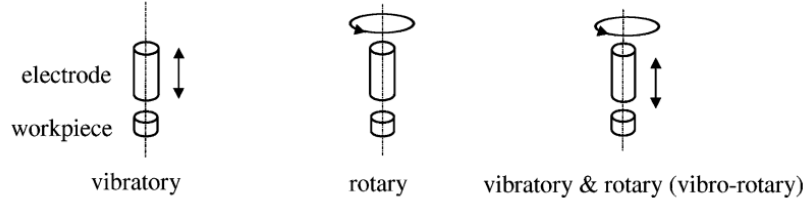
Figure 2.17: Types of motion imparted to the tool electrode [13].
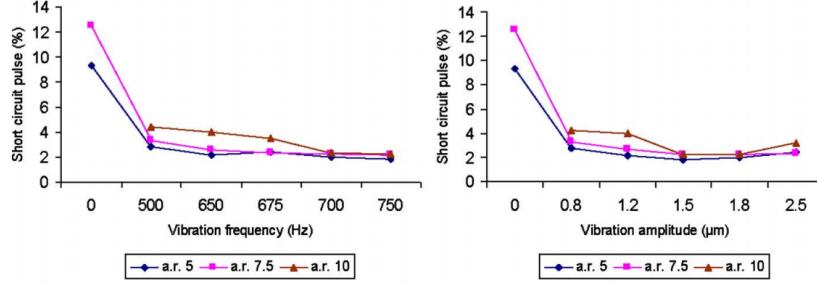
Figure 2.18: Comparison of machining stability in conventional and vibration-assisted EDM [14].
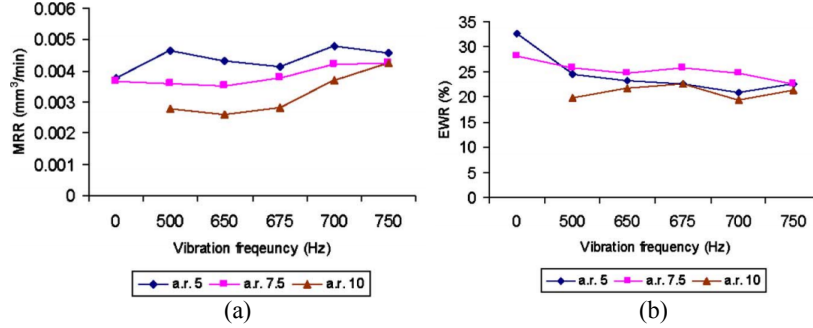
Figure 2.19: Comparison of conventional and vibration-assisted EDM in terms of (a) MRR and (b) Electrode Wear Rate [14].

mance of EDM process since the mid 1980s [86, 87, 88, 89, 90, 91, 92, 93] especially in cases where conventional forced or suction of dielectrics cannot be employed. The debris in the gap are subjected to ultrasonic field forces and unique kind of convection currents that are generated due to cavitation and micro-streaming phenomena [87] which helps in clearing out the inter-electrode gap. The ultrasonic vibrations improved the ejection of material from the melt pool, reduced the thickness of the heat affected layer and number of micro-cracks on the machined

31

surface [89]. The material removal is enhanced because of a decrease in the hydrostatic pressure within the gap. Gao and Liu (2003) [15] found that ultrasonic vibration lead to enhanced material removal compared to conventional EDM, especially for thin workpieces where an eight-fold increase in MRR was observed (see Fig. 2.20). This was attributed to the better flushing conditions within the gap. Yeo and Tan (1999) [94] improved the aspect ratio of micro-holes drilled in stainless steel workpiece from six to fourteen by imparting ultrasonic vibrations to the tool electrode.
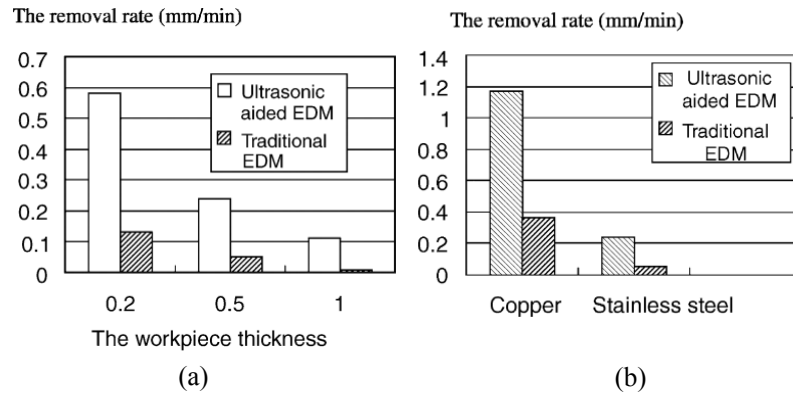
Figure 2.20: Comparison of MRR in conventional and ultrasonic EDM [15].

Thoe et. al. (1999) [91] used ultrasonic vibrations to increase the MRR when drilling micro-holes in hard-to-machine materials such as ceramic coated nickel alloys. The diameter difference between entrance and exit when drilling holes with diameter and depth of about 150μm and 500μm was drastically reduced to about 2μm with the use of ultrasonic vibrations. Huang et. al (2003) [16] used ultrasonic vibrations to increase machining efficiency by about sixty times in drilling micro-holes in Nitinol without significantly affecting electrode wear. However, the introduction of ultrasonic vibrations created a small and unwanted horizontal vibration of the tool electrode which resulted in profile errors for the drilled holes (see Fig. 2.21).

Ultrasonic vibrations are not widely used for $\mu - $ EDM applications due to the possibility of deflection of the tool electrode due to the high frequency vibrations. This can also result in reduced machining stability, especially when thin electrodes

Without ultrasonic vibrations   With ultrasonic vibrations
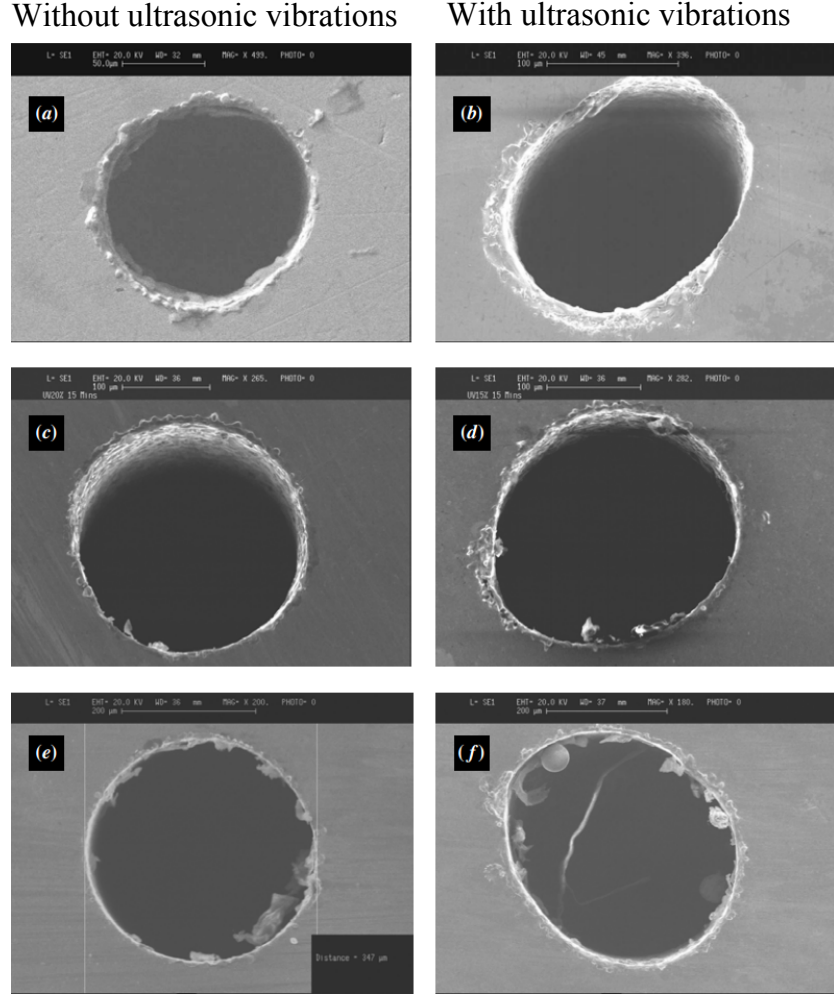
Figure 2.21: Micro-hole profiles at the entrance for electrode diameters of (a) and (b) 100μm, (c) and (d) 200μm, (e) and (f) 300μm [16].

are employed [14]. They also tend to accelerate tool wear even though a higher material removal is achieved. Machining accuracy is also compromised to some extent when ultrasonic vibrations are used [95].

Magnetic field-assisted flushing

Several research efforts have been made into the use of magnetic field for improved flushing in EDM [17, 96, 97, 18, 98, 19]. The concept of using magnetic field to assist in gap cleaning for EDM was first developed by De Bruijn et. al. (1978) [97]. The debris particles within the gap behave as dipoles when subjected to a mag-

netic field. The direction of the field is such that the magnetic force directs the particle out of the machined feature and away from the discharge region. Yeo et. al. (2004) [17] found that there is no appreciable difference in MRR between conventional and magnetic field-assisted EDM in the initial stages of machining (see Fig. 2.22). This is because the centrifugal force of the rotating electrode is sufficient to remove the debris from the drilled hole for smaller depths. However, with further machining the effect of magnetic field becomes appreciable and about 26% increase in depth of hole is observed due to effective debris transport achieved with magnetic field.
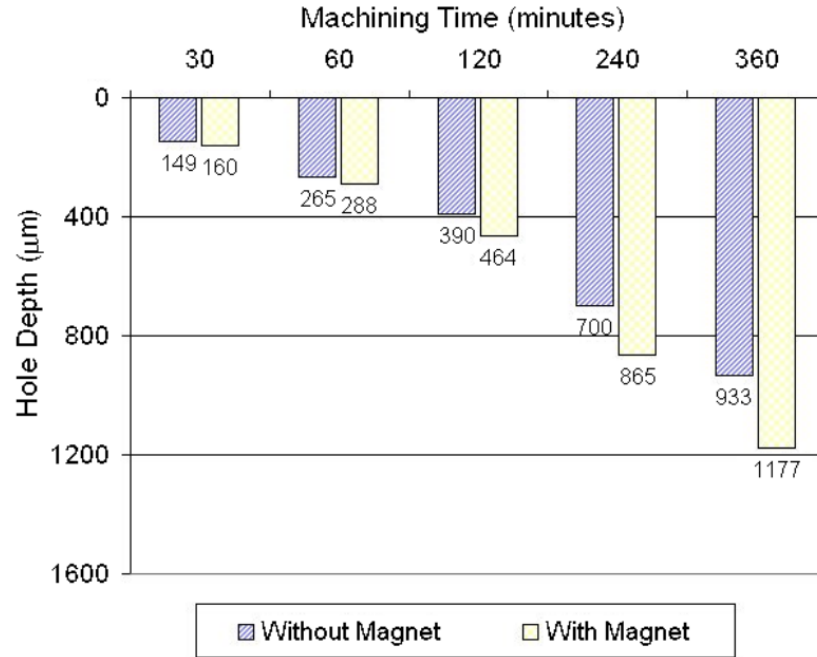
Figure 2.22: Variation in depth of drilled hole with machining time [17].

Although no significant difference in surface roughness was observed, the tool wear was higher along the length of the electrode in the case of magnetic field-assisted EDM (see Fig. 2.23). This was attributed to distortion in the tool electrode due to applied magnetic field.

Lin et. al. (2009) [18] studied the effects of magnetic field on the machining of SKD 61 steel using copper electrode. As seen from Fig. 2.24, the MRR was about three times higher than the conventional EDM and the surface roughness
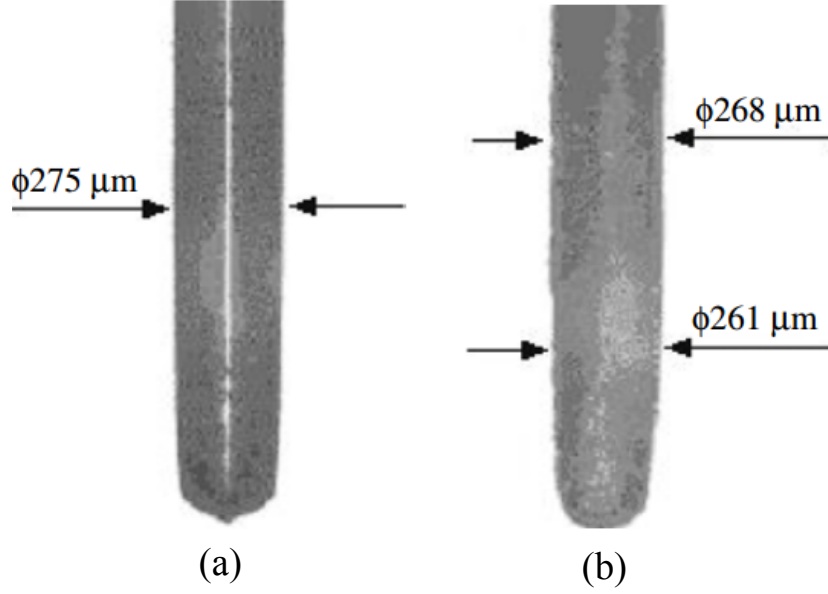
Figure 2.23: Shape of tool electrode after machining (a) without magnetic field and (b) with magnetic field [17].

was also lower. The reduction in frequency of short circuiting due to effective debris removal was identified as the reason for enhanced MRR in the case of magnetic field-assisted EDM. Also, the thickness of the recast layer was higher for conventional EDM because unexpelled debris were re-melted and re-solidified on the machined surface. With effective flushing, these debris move away from the discharge region, thereby limiting the formation of the recast layer (see Fig. 2.25).

Heinz et. al. (2011) [19] developed a method to improve the performance of $\mu - $ EDM for non-magnetic materials. When a directional current is flowing through the non-magnetic workpiece placed in a magnetic field, a Lorentz force is produced when the current and the magnetic field are non-parallel. The Lorentz force can be directed into or out of the workpiece for improvement in MRR. It was observed that upto 50% increase in MRR can be achieved when the Lorentz force was pointing into work surface. Also, the average distance of the debris particles from the center of the crater increased from about 164 μm to 207 μm when Lorentz force was applied (see Fig. 2.27).

In summary, the magnetic field-assisted EDM is applicable only to workpieces that are magnetic. Several materials that are machined using EDM are non-
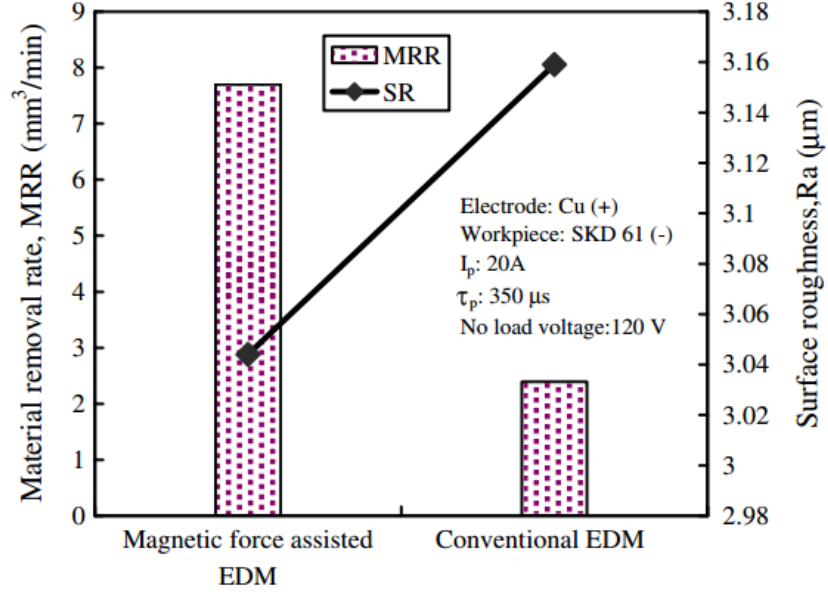
Figure 2.24: Comparison of MRR and surface roughness for conventional and magnetic field-assisted EDM [18].
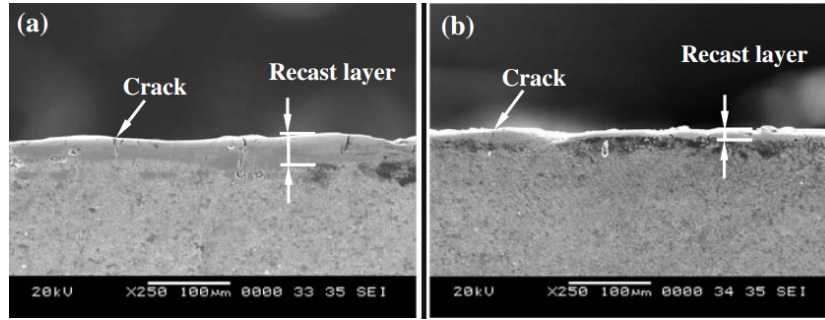
Figure 2.25: Cross section of machined surface obtained by (a) conventional EDM and (b) magnetic field-assisted EDM [18].

magnetic and this technique cannot be used for improving the machining performance in such cases. Though a method was developed for non-magnetic materials, a large magnetic field is required to achieve improvement in process performance. Also, the magnetic field induced a distortion in the tool electrode which caused higher wear during operation.

In addition to the experimental research on developing better flushing systems for EDM, computational modeling has also been used to investigate the debris flushing phenomenon. A thorough review of the models developed for improving
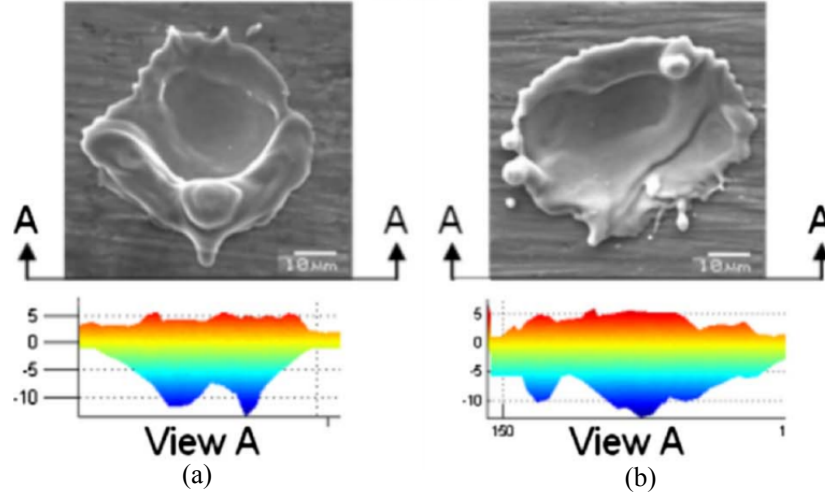
Figure 2.26: SEM and laser scan images for (a) conventional EDM and (b) Lorentz force-assisted EDM [19].
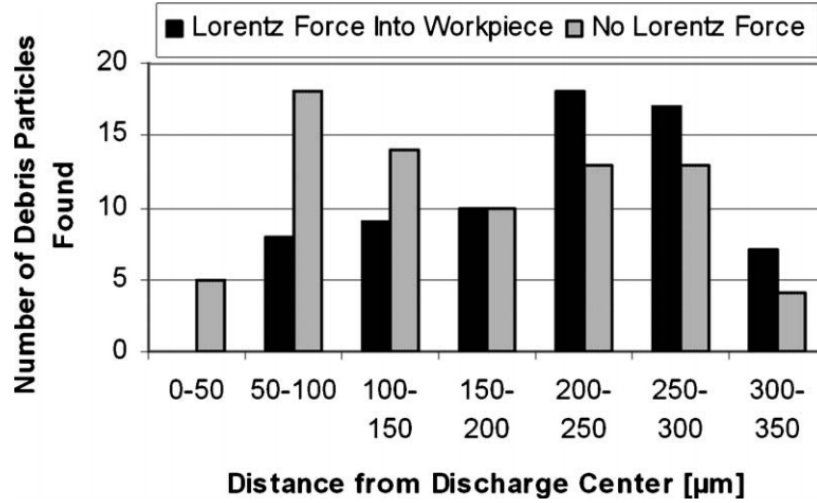
Figure 2.27: Comparison of debris distribution for conventional and Lorentz force-assisted EDM [19].

debris flushing in EDM is presented in the next section.

2.3.2   Modeling Debris Flushing in EDM

As discussed in Section 2.3, the removal of debris is critical to achieving good process performance in EDM. In this regard, several modeling studies have been performed to understand the debris flushing in EDM. Okada et. al. [20] studied the flow field of the dielectric medium in machined kerf during the wire-EDM

process. The effect of the flow rate of the dielectric from the nozzles and the stand-off distance (distance between the nozzle exit and the workpiece surface) on the flow field and debris distribution within the machining zone were investigated with a three-dimensional, unsteady and turbulent flow model with one-way coupling between the continuum and particles to determine the optimum parameters for supplying the dielectric. The flow field from model was compared with PIV measurements obtained using transparent acrylic *dummy* workpiece. A good quantitative agreement was observed for the flow velocity in both cases (see Fig. 2.28).
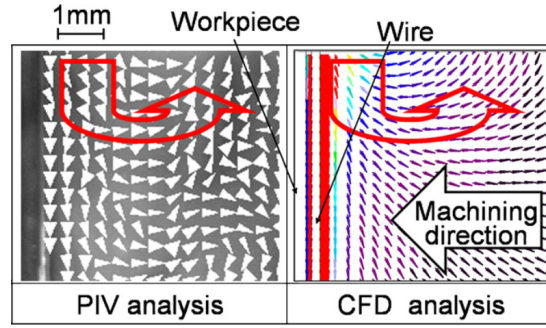
Figure 2.28: Comparison of flow velocity for PIV and CFD model [20]

The flow field in the machined kerf for different flow rates from the top and bottom nozzle are shown in Fig. 2.29. A stagnation area where the top and bottom jets meet results in the poor flushing within the vicinity due to very small fluid velocity. The recirculation of debris in the stagnation region is clearly depicted in Fig. 2.30. Only 32 debris particles were considered in this study which is too few to derive statistically valid conclusions. Also, the impact force associated with the sparks (the pressure due to the plasma bubble is of the order of 200 MPa [47]), one of the critical factors affecting the dielectric flow and trajectory of debris particles was not considered in their model. Also, the debris particles were assumed to have the same diameter (10μm), unlike the actual case.

Cetin et. al. [21] studied the concentration of debris particles in the machining region during deep hole drilling operation. A 2-dimensional, axisymmetric, unsteady, turbulent model was developed to investigate the effect of electrode
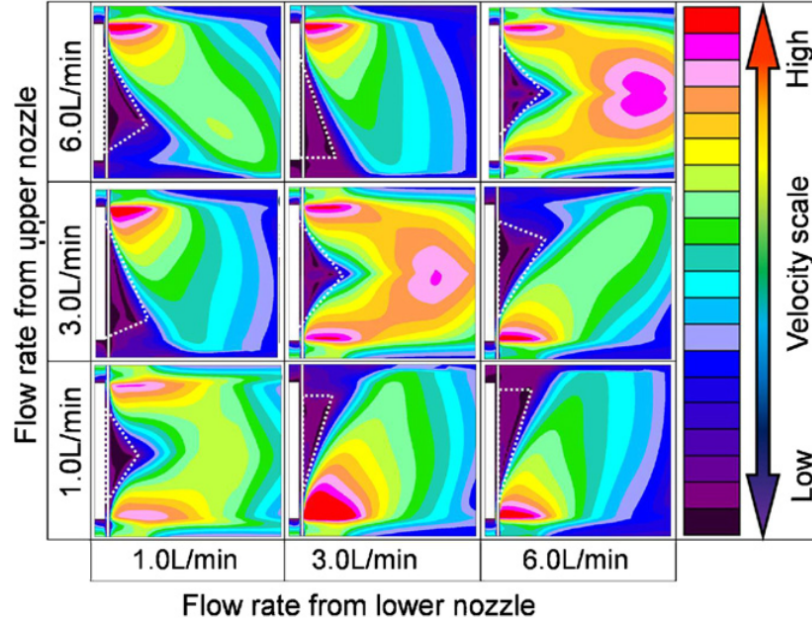
Figure 2.29: Velocity contours of fluid in machined kerf [20]
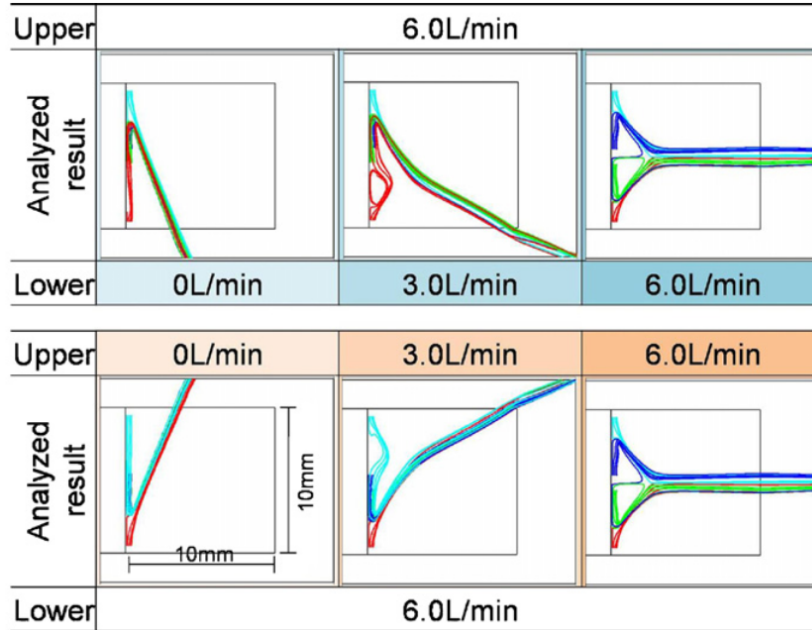
Figure 2.30: Trajectory of debris particles [20]

jump height and jump speed for enhancing the debris flushing in a linear motor-equipped Electric Discharge Machine. The fluid domain is shown in Fig. 2.31 and the velocity field of the dielectric for small and large jump heights are shown in and Fig. 2.32 and Fig. 2.33, respectively. The retraction of the electrode results

39

in the formation of two vortices within the inter-electrode gap which can result in improper flushing of the debris.
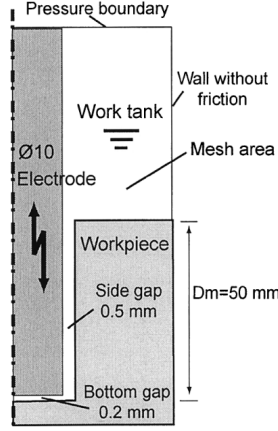
Figure 2.31: Fluid domain for simulating electrode jump motion [21]
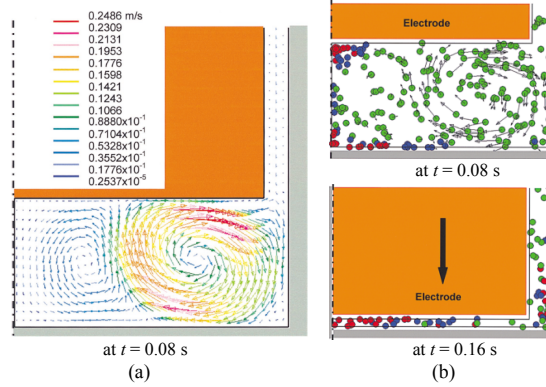
Figure 2.32: Jump height of 2.4 mm (a) velocity vectors and (b) debris particles motion [21]

About 362 debris particles with constant diameter of 10μm were considered and distributed uniformly within the fluid domain. A larger *jump height* of the electrode produced better flushing compared to lower height as seen in Fig. 2.33. Thus larger *jump height* prevents formation of debris-rich regions in the inter-electrode gap, thereby minimizing the concavity of side walls during EDM.

However, the effect of impact force of the discharges on debris movement was neglected. Also, too few particles with same diameter were considered in this study unlike the actual scenario.
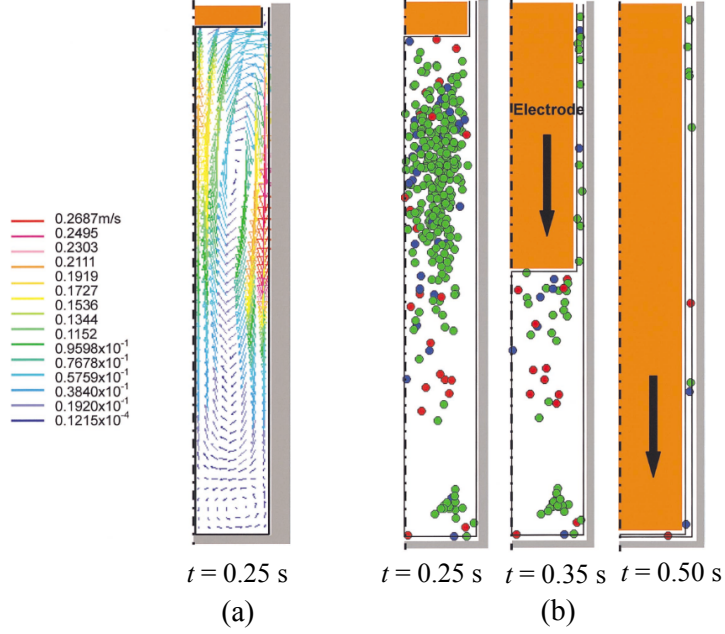
Figure 2.33: Jump height of 38 mm (a) velocity vectors and (b) debris particles motion [21]

Wang and Han [22] studied the distribution of debris particles for EDM with multiple discharges by developing a 3-dimensional, unsteady, laminar model with solid particles (debris), liquid (dielectric) and gas bubbles (from vaporized dielectric). The VOF method was used to predict the formation and movement of the bubbles and the DPM module was used for determining the trajectories of the debris particles formed. This enabled them to include the effect of bubbles on the trajectory of debris particles. The movement of bubbles and debris within the discharge gap is shown in Fig. 2.34 and Fig. 2.35. However, all the debris particles were assumed to be 25μm in diameter, unlike the actual case.

Mastud et. al. (2014) [23] developed a two-dimensional axisymmeteric model to study the vibration-assisted Reverse Micro-Electrical Discharge Machining process (R $-$ μEDM) that is used to make high aspect ratio micro-structures. A large number of particles (around 36000) with a log-normal debris size distribution (90 to 950 nm) was considered. The different zones in the fluid domain are shown in Fig. 2.36. The pulsating movement of the tool electrode at higher frequencies prevents the agglomeration of particles within the gap and the flow
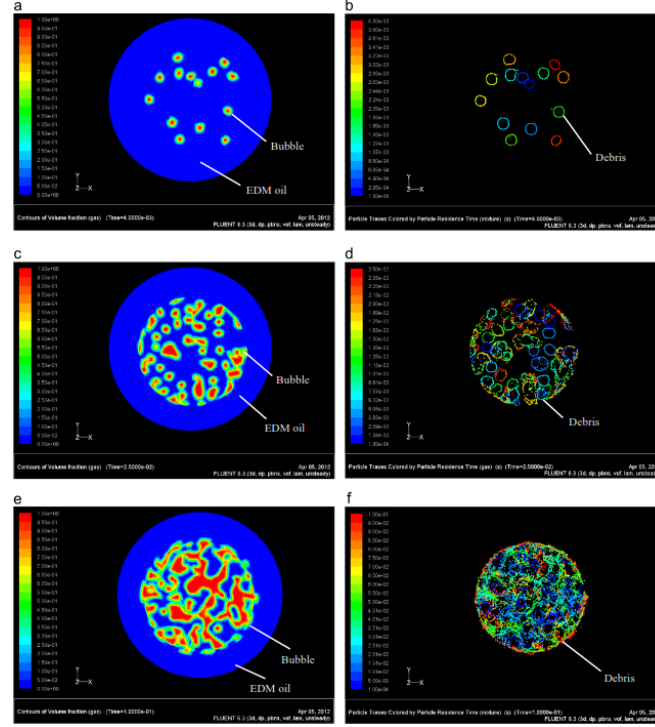
Figure 2.34: Evolution of bubbles and debris on the bottom of tool electrode at (a),(b) 0.004 s; (c),(d) 0.025 s and (e),(f) 0.1 s [22]

reversal helps to alter the sparking location, thereby resulting in uniform material removalFig. 2.37.

The roughness on the machined surface is comparable to the size of debris particles and influences the trajectories. However, the actual topography of the machined surface is not considered in this study. Also, the effect of plasma implosion/explosion on the debris motion is not included in the model.

In summary, several techniques including jet flushing, magnetic flushing, vibration flushing have been developed to enhance the removal of debris particles from the discharge zone in EDM. However, these methods require extensive set ups for implementation and proper synchronization with the discharge process is required for techniques such as vibration-assisted flushing. Also, the consumption of dielectrics is not minimized with methods like jet flushing. There is a need to develop a novel process that will improve debris flushing and also reduce consumption of dielectric fluids. To achieve this objective, a technique similar to the
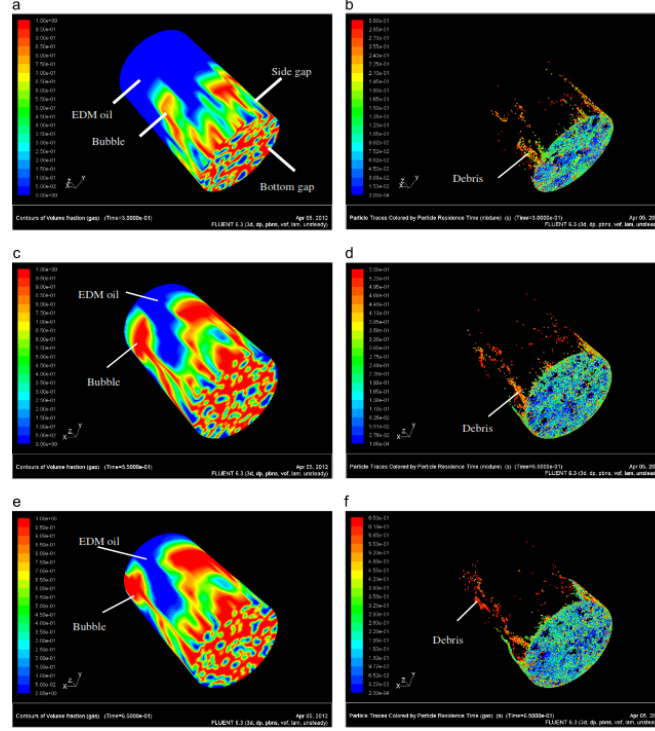
Figure 2.35: Evolution of bubbles and debris on the sides of tool electrode at (a),(b) 0.3 s; (c),(d) 0.55 s and (e),(f) 0.65 s [22]
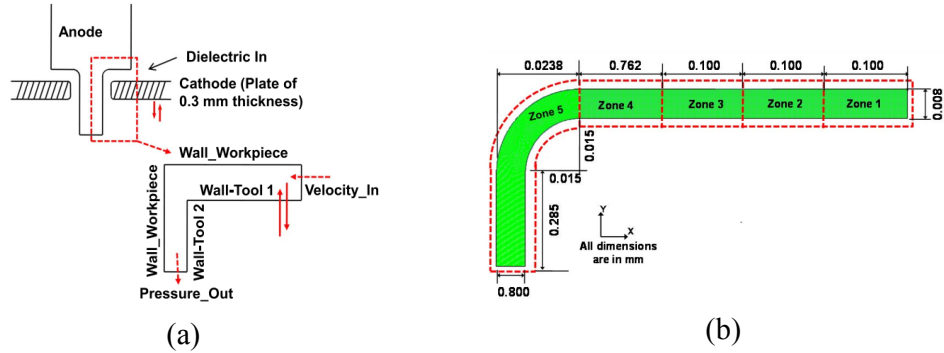
Figure 2.36: (a) Fluid domain for $(R - \mu EDM)$ simulation and (b) Zones and dimensions in fluid domain [23]

Atomization-based Cutting Fluid (ACF) systems that is currently used for micro-milling and turning applications could be developed for EDM. A brief overview of the ACF system including the components, working principle and results from previous machining studies are discussed in the next section.
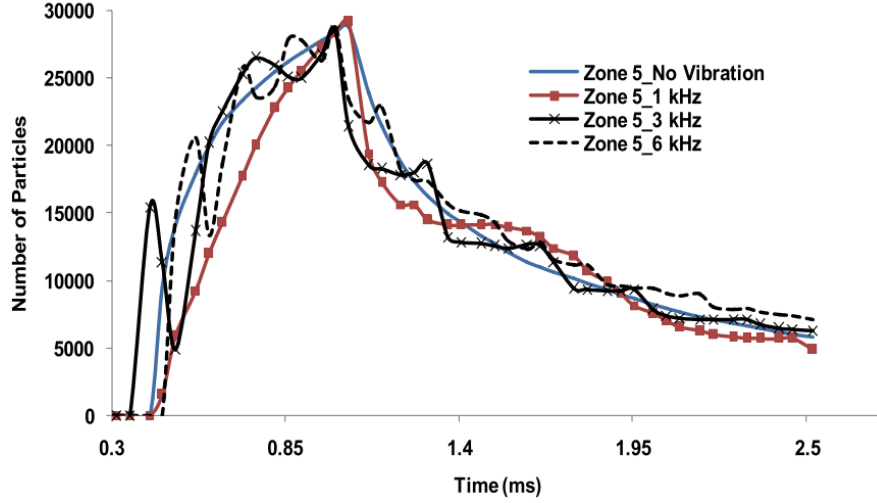
Figure 2.37: Debris particle concentration in discharge region (Zone 5) [23]

2.4 Atomization-based Spray Systems for Machining

The ACF system was developed by Jun et. al. (2008) [24] and Nath et. al. (2012) [26] for micro-machining and machining titanium alloys, respectively. The use of atomization-based cutting fluid system has been extensively researched in the recent years [24, 26, 29, 99, 100, 101, 52, 25, 102]. The ACF system was developed by Jun et. al. (2008) [24] because the forces generated by conventional flood cooling systems on the tool are comparable to the machining forces for micro-machining and might deflect the tool, thereby reducing the accuracy. Also, the cutting fluid must be able to penetrate the narrow cutting zone (order of μm) for effective cooling and lubrication during machining. A schematic of the system used for micro-milling aluminum is shown in Fig. 2.38. Droplets of cutting fluid produced by the ultrasonic atomizer are transported through a pipe that has a nozzle co-axially placed inside it and through which a stream of high velocity gas is supplied. As soon as the droplets reach the exit of the pipe, they are entrained by the high velocity carries gas and carried to the machining zone. The velocity of the gas is selected such that the droplets are in spreading regime when they impact the machining surface.

44
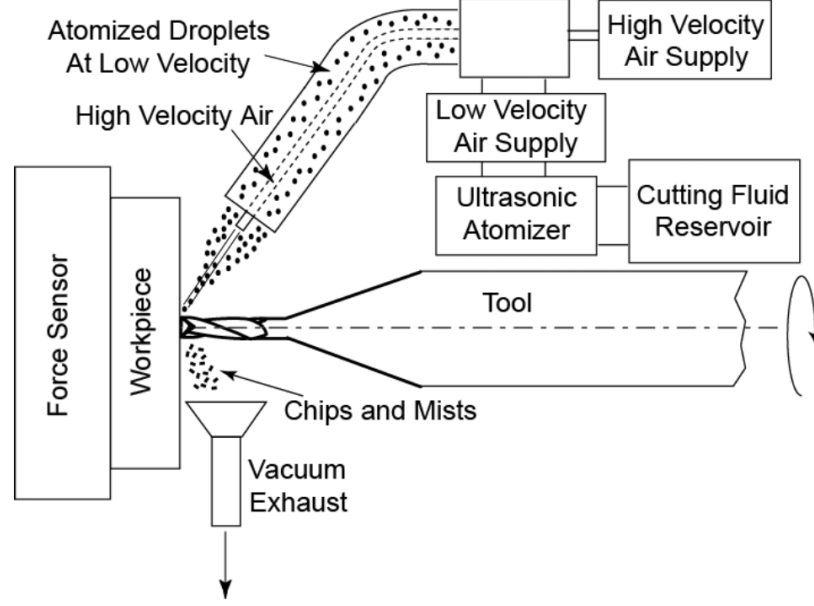
Figure 2.38: Schematic of the ACF spray system [24].

Components of a typical ACF spray system

A schematic of the spray system developed by Nath. et. al. (2012) [26] is shown in Fig. 2.39. It consists of a reservoir for the cutting fluid that is connected to a an ultrasonic atomizer system. Ultrasonic atomization is preferred to shear-flow atomization to generate the droplets due to better control over droplet size and velocity in the former method. Also, this method does not require a high pressure pump to produce droplets and results in lesser energy consumption during the atomization process [24]. The fluid from reservoir is fed to the horn of the atomizer forming a film on its surface. A fluid film that is contact with the resonating surface of the atomizer forms surface waves that reach instability and undergo a break-up process, thereby producing uniform droplets (Fig. 2.40). The mean diameter of droplets d_m is related to the density (ρ), surface tension (σ) of fluid and frequency of ultrasonic vibrator (f) by the corrected Lang formula as [103],

$$d_m = 0.73 \left(\frac{\sigma}{\rho f^2} \right)^{1/3}.$$ \hfill (2.1)

The droplets are fed through a *droplet nozzle* that has a converging portion.

45
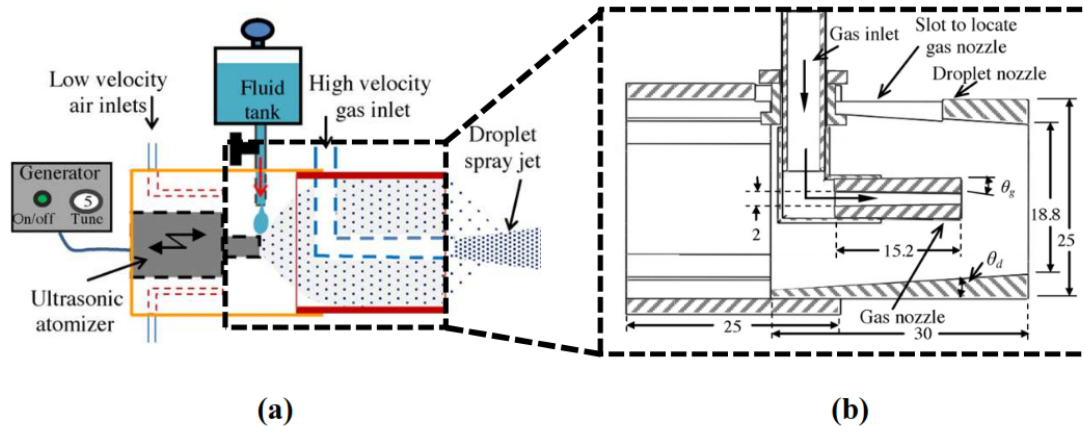
Figure 2.39: (a) Schematic of the ACF system; and (b) Cross-section of the nozzle assembly [25].

1- Backing piece	3 – Mechanical transformer
2.1 – Piezoelectric element	4 – Atomizer horm
2.2 - Piezoelectric element	5 – Small channel for liquid to enter atomizer
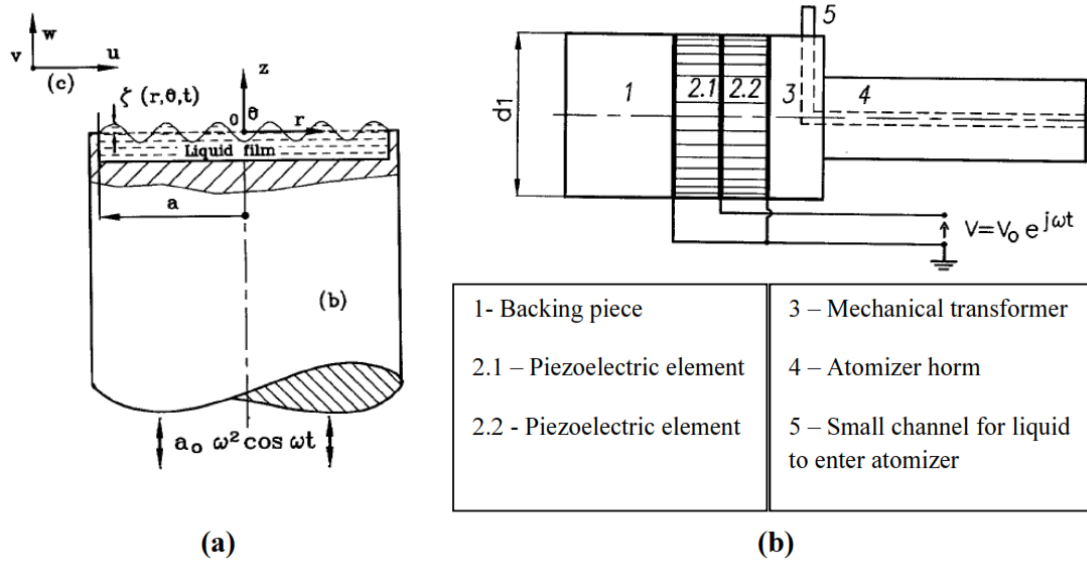
Figure 2.40: (a) Break-up of liquid film on a resonating surface; and (b) Schematic of ultrasonic atomizer [25].

A *gas nozzle* is placed co-axially within the *droplet nozzle* and a high pressure carrier gas (air,CO_2) is supplied through it. The droplets interact with the high velocity gas from the *gas nozzle* and are entrained due to the pressure drop created at the center line of the nozzle. The atomized droplets are transported to the machining zone where they form a thin film due to impingement on the surface. The improved penetration of the film into the tool-chip interface enhances the

46

cooling and lubrication processes during machining.

Performance of ACF spray system

The performance of dry cutting, flood coolant and ACF systems was investigated by Jun et. al. (2008) [24] and lower cutting forces were observed in th case of the ACF system (Fig. 2.41). Also, more than 50 slots were machined with a micro-milling cutter using the ACF system compared to 8 slots and 5 slots when using flood cooling and dry cutting, respectively. This was attributed to the better evacuation of chips from the cutting zone provided by the ACF system (Fig. 2.42). In other two methods inadequate removal of chips resulted in increased welding of chips on the machined surface, thereby increasing surface roughness and also reducing tool life considerably.
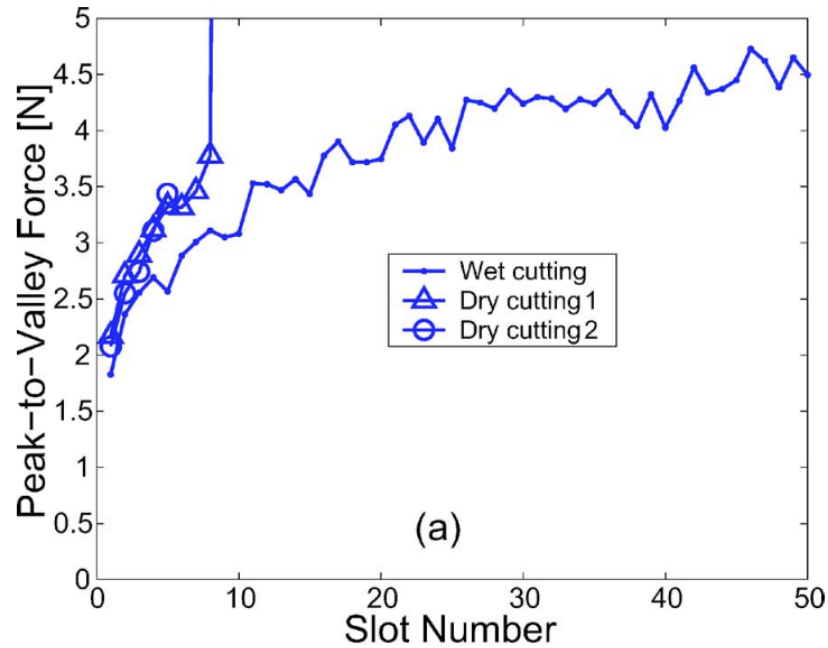
Figure 2.41: Cutting forces for a feed rate of 0.33μm/flute [24].

Nath et. al. (2012) [26] used the ACF system for machining difficult-to-machine materials such as titanium alloys in macro-scales. Due to larger cutting zone in macro-scale compared to micro-machining, the flow rate of cutting fluid was
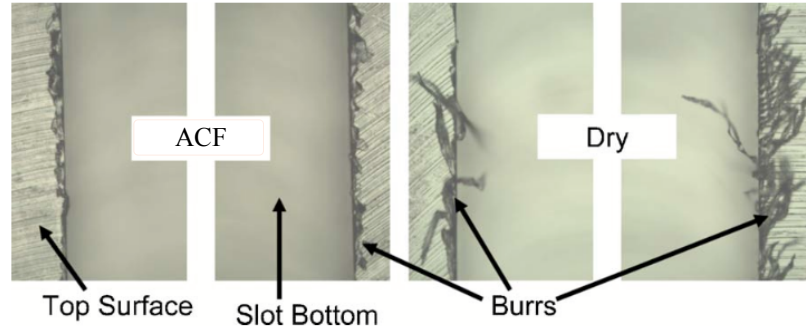
Figure 2.42: Burrs produced by micro-machining at a feed rate of 0.33μm/flute [24].

about $10-20$ml/min compared to $1-2$ml/min used in the latter case. Turning experiments were performed using uncoated carbide inserts as tool materials to study the effect of the ACF system parameters viz., carrier gas type and pressure, fluid flow rate, impingement angle, and spray distance on machining performance. With the ACF system, tool life improved by as much as 40-50% over flood cooling. The atomized droplets have been observed to easily penetrate the tool chip interface via thin film formation, thereby improving tool life. Figure 2.43 shows a combination of low pressure, long spray distance and high flow rate results in enhanced tool life. The tool rake and flank wears are shown in Fig. 2.44. Also, the use of air-CO_2 mixture was observed to produce more broken chips compared to other carrier gases, thereby preventing the entanglement of chips near machining zone and results in better machining performance (Fig. 2.45). This was attributed to the lower temperature of the gas due to mixing with CO_2 that makes the chips formed to be highly brittle.

In order to improve the performance of machining using the ACF system, it is critical to ensure the formation of a thin film of cutting fluid at the tool-chip interface. The formation of a thin film on a surface is influenced by several parameters including the diameter of droplets, velocity of droplets, nature of the surface and the angle of impingement of the droplets on the surface. In this regard, the fundamental aspects of droplet-surface interaction are discussed in the next section.
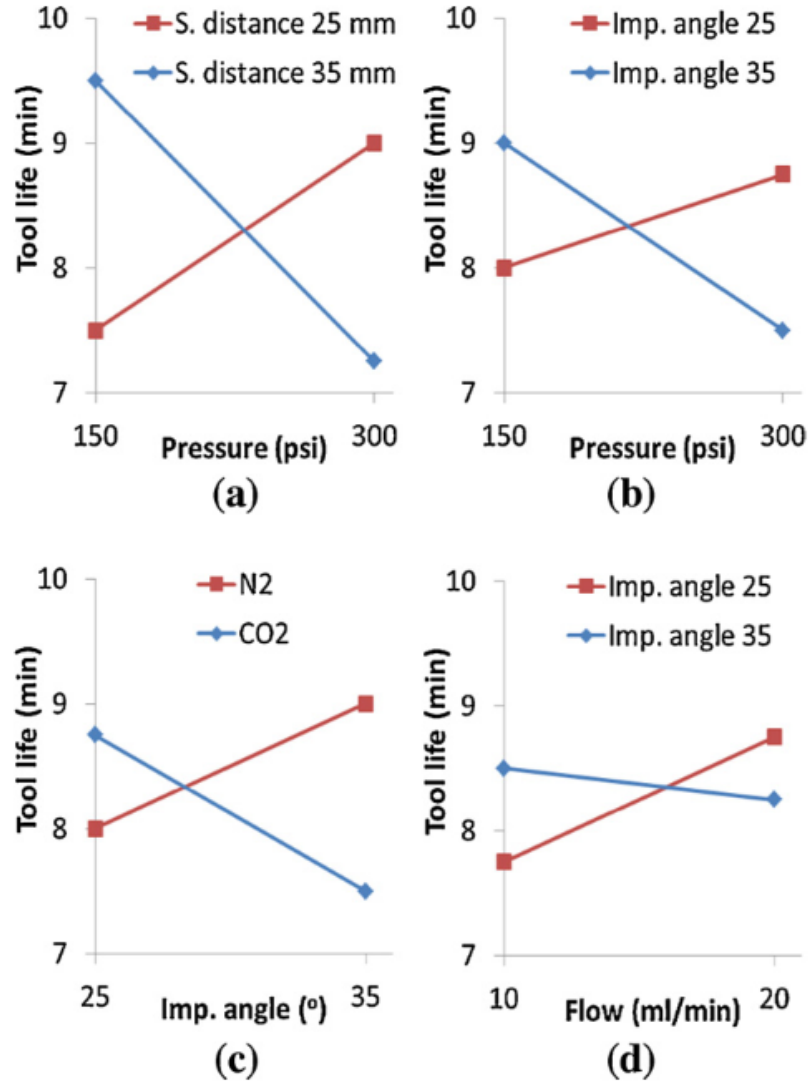
Figure 2.43: Two way interaction plots for tool life [26].

Droplet Impingement Dynamics

The first step in understanding the droplet-surface interaction phenomenon is the study of interaction a single droplet on a surface. Since this phenomenon is observed in several fields such as ink jet printing, coating of materials, ordinary and electrostatic-spray painting for the automotive and aerospace industry, evaporative cooling and fuel injection for engine systems, extensive research has been performed over the years for understanding the droplet dynamics [104].

Some of the common droplet-surface interaction scenarios encountered in practi-
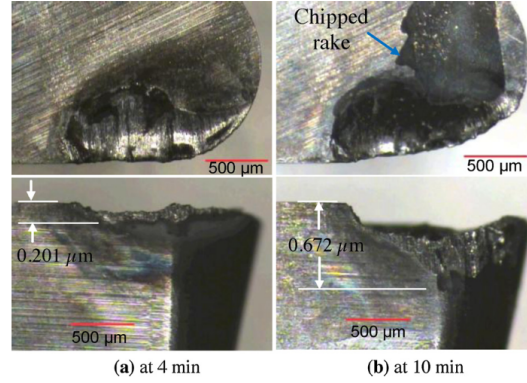
Figure 2.44: Tool rake and flank faces for 150 psi, 20 ml/min and air-CO_2 combination [26].

Figure 2.45: Chips produced using carrier gases (a) air-CO_2 and (b) N_2 [26].

cal applications are shown in Fig. 2.46 [27]. In the case of ACF system for machining, the oblique impact of multiple droplets on a solid surface (initial formation) or a shallow liquid surface (after initial impact of droplets) are encountered. The droplet dynamics in these cases is thus critical to selecting the dielectric fluid, droplet parameters such as size and velocity and also spray parameters such as gas pressure, impingement angle and length of spray.

The outcome of droplet impact depends on the impinging parameters such as droplet diameter (d_m), droplet velocity (v_d) and liquid properties such as dynamic viscosity (μ), density (ρ) and surface tension (σ). Depending on the aforementioned factors, the spray-surface interaction on a solid surface may correspond to one of the four regimes, viz., (i) stick, (ii) rebound, (iii) spread and (iv) splash (see Fig. 2.47).
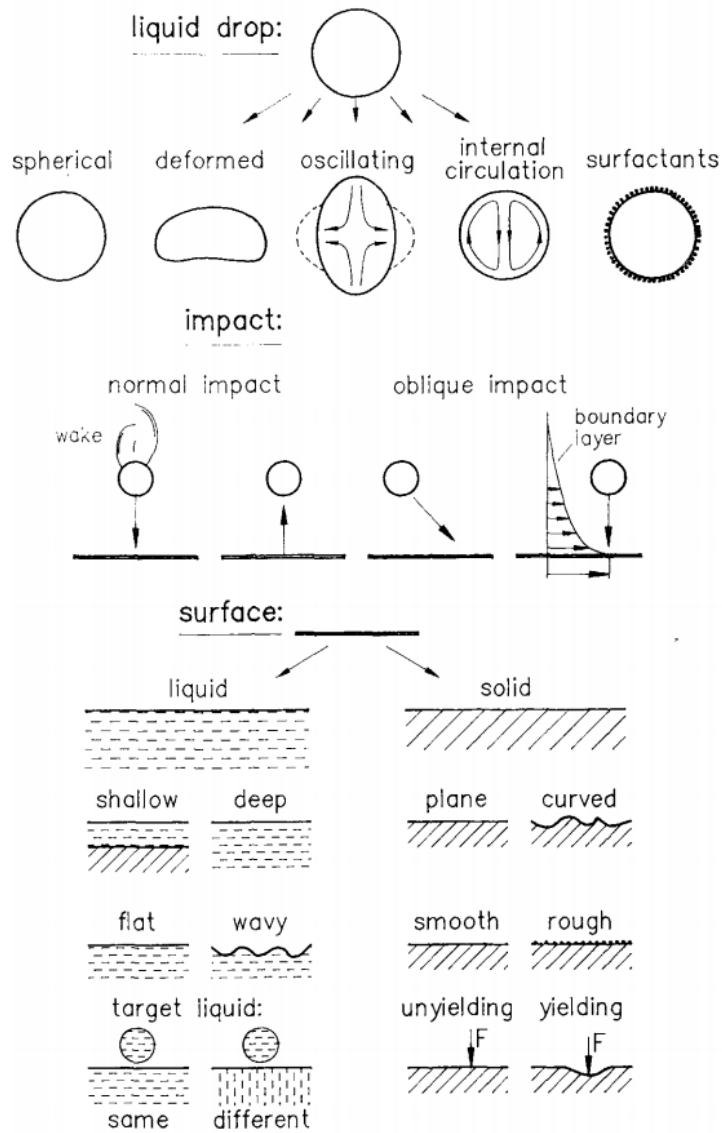
Figure 2.46: Conditions governing the dynamics of a droplet on impact [27].
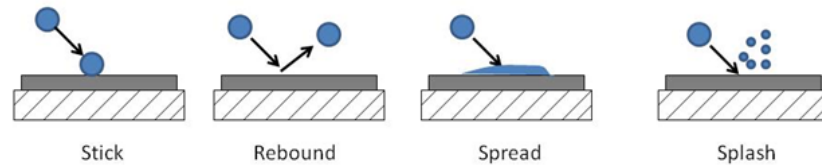
Figure 2.47: Regimes of droplet-surface interaction

Since the impact process is affected by a large number of fluid properties and impingement conditions, these regimes are characterized by non-dimensional numbers such as Weber number (We), Reynolds number (Re) and Ohnesorge num-

ber (Oh) [28].

$$We = \frac{\rho v_{dn}^2 d}{\sigma}, \tag{2.2}$$

$$Re = \frac{\rho v_{dn} d}{\mu}, and \tag{2.3}$$

$$Oh = \frac{\mu}{\sqrt{d\sigma\rho}}, \tag{2.4}$$

where v_{dn} is the normal component of the droplet velocity. We is the ratio of inertial forces to surface tension, Re is the ratio of inertial forces to viscous forces and Oh is the ratio of viscous forces to inertial forces and surface tension.

When the impact energy of the droplet is low, it will *stick* to the surface retaining its spherical shape without appreciable deformation. Stanton et. al. (1998) [105] found empirically that stick phenomenon occurs for $We < 5$. At a higher impact energy, the droplet will entrap a layer of air between the surface and itself, thereby causing it to *rebound* on impact. Stow and Hadfield (1981) [106] determined that droplets rebound for $5 < We < 10$ which is in agreement with that proposed by Stanton et. al. (1998) [105]. When the impact energy is sufficiently high so as to prevent entrapment of air, the droplets tend to deposit on the impinging surface and *spread*. At much higher impact energy, *splashing* is observed, where the droplets undergo unstable break-up process on impacting the surface and fail to form a film on the surface. The transition from spreading to splashing regime is shown in Fig. 2.48. Both *spreading* and *splashing* occur at $We > 10$ and the regimes are identified by using the non-dimensional numbers that are specific to the impact conditions which are defined as follows.

For a single droplet impinging on a dry surface, the boundary between spreading and splashing regimes is governed by K_m which is given by,

$$K_m = \frac{(\rho d_d)^{3/4} v_{dn}^{5/4}}{\sigma^{1/2} \mu^{1/4}}. \tag{2.5}$$

For a single droplet impinging on the liquid surface of a thin film, the boundary
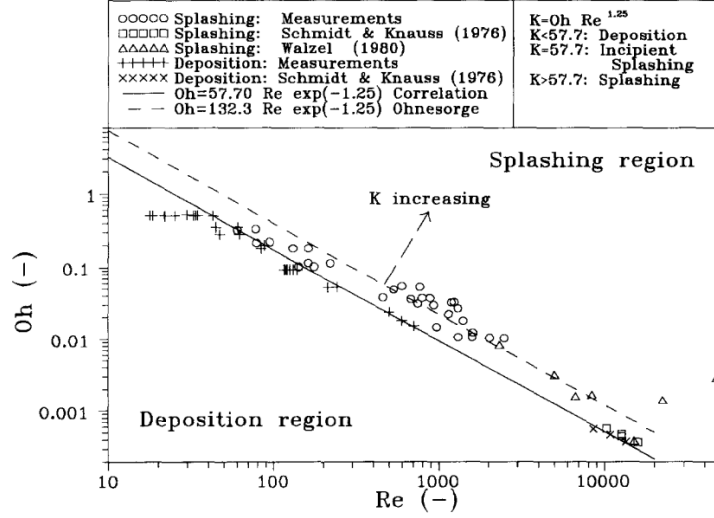
Figure 2.48: Limits for spreading and splashing of impacting droplets [28]

between spreading and splashing regimes is governed by K that is defined as,

$$K = \frac{(\rho d_d)^{6/5} v_{dn}^2}{\sigma^{4/5} \mu^{1/2}}. \tag{2.6}$$

For a train of droplets impinging on the liquid surface such as that encountered in ACF system for machining applications, the boundary between spreading and splashing regimes is governed by K_y defined as,

$$K_y = v_{dn} \left(\frac{\rho}{\sigma}\right)^{1/4} \left(\frac{\rho}{\mu}\right)^{1/8} f^{-3/8}. \tag{2.7}$$

Among the four regimes, for effective film formation, the droplet interaction has to be in the spreading regime. The spread-regime occurs for $We > 10$ and $K_m < 57.7$ or $K_y < 17$. This is because the film should be able to penetrate the tool-chip interface and also possess sufficient velocity for removal of chips. However, the velocity cannot be made higher than that specified by aforementioned conditions since droplets will then splash which will prevent the film formation on the machined surface. Therefore it is critical to identify the combination of spray parameters that will ensure formation of film on the machining surface through experimental or computational methods. Modeling of sprays and film formation has been investigated through computational modeling for applications such as

53

spray forming, spray cooling and combustion of fuels. Some of these studies are reviewed in the following section.

2.5 Modeling Sprays and Film Formation

In order to ensure the formation of dielectric film on the workpiece surface during machining, it is necessary to determine the velocity of the droplets at specific distances form the exit of the droplet nozzle. The velocity of the droplets is influenced by the nozzle configuration and carrier gas pressure. Research on studying spray characteristics with ACF system is presented since it is similar to the proposed Spray-EDM process in terms of the atomized-spray formation, spray-surface interaction and film formation. Experimental investigation were carried out by Rukosuyev et. al (2010) [29] and Nath et. al (2012) [26] to determine the spray pattern for effective application to micro-milling and turning titanium alloys respectively. The effect of the velocity of water droplets and carrier gas on spray characteristics such as the focus length and height (see Fig. 2.49) was studied by Rukosuyev. et. al (2010) [29]. This is because a narrow and focused spray of droplets is required due to smaller cutting zone in the micro-machining. While the focus height determines the diameter of spray, the focus length helps to select the distance between the nozzle tip and the workpiece. Experiments were also carried out for different nozzle configurations shown in Fig. 2.50. The nozzle configurations with the gas nozzle positioned within the droplet nozzle are observed to produce a focused spray (see Fig. 2.51). Also, a converging gas nozzle has a better focusing effect compared to a straight nozzle, especially for higher higher droplet velocities. The effect of droplet and gas velocities were studied further using the nozzle configuration (a) in Fig. 2.50. A higher focus length and height is observed for greater droplet velocities since the gas from the inner nozzle takes greater time in entraining faster droplets compared to slower ones due to the droplet inertias (see Fig. 2.52).

Nath et. al (2012) [26] studied the spray characteristics including the droplet
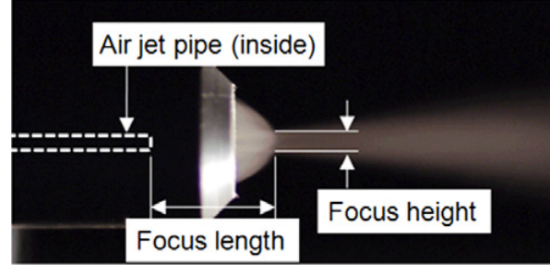
Figure 2.49: Spray characteristics [29]
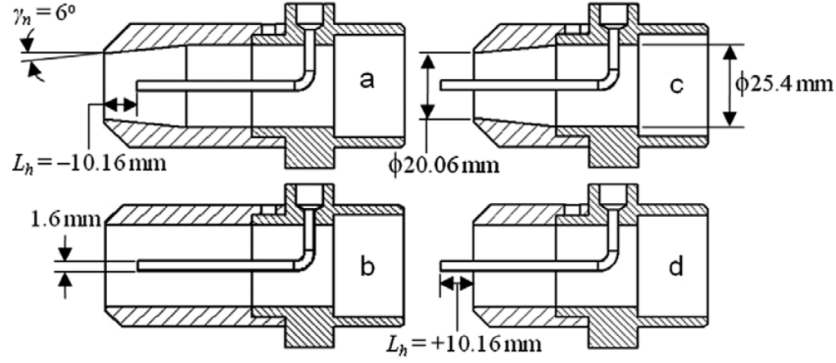
Figure 2.50: Nozzle configurations considered in spray pattern investigation [29]
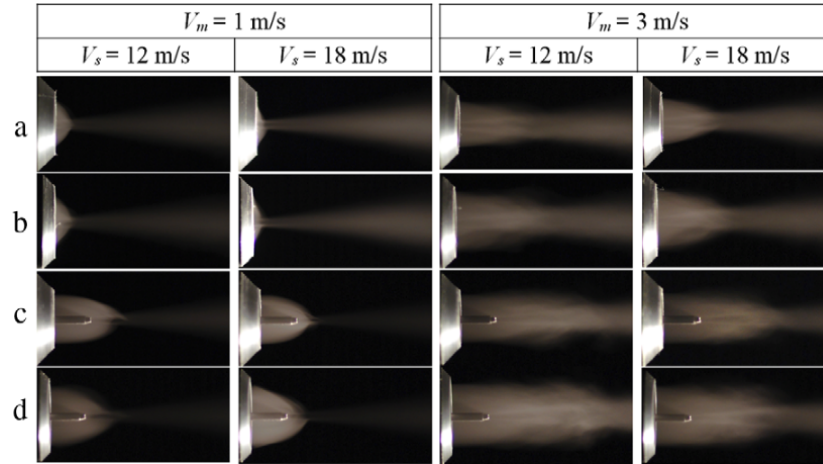
Figure 2.51: Photographs of spray for different nozzle configurations [29]

entrainment zone and flow development regions as a function of droplet and gas velocities through experimental research and analytical modeling. Apart from spray characteristics, the effect of spray parameters on turning performance measures such as tool wear and surface roughness were also investigated. A higher droplet velocity resulted in smaller droplet entrainment angle as shown in Fig. 2.53. An
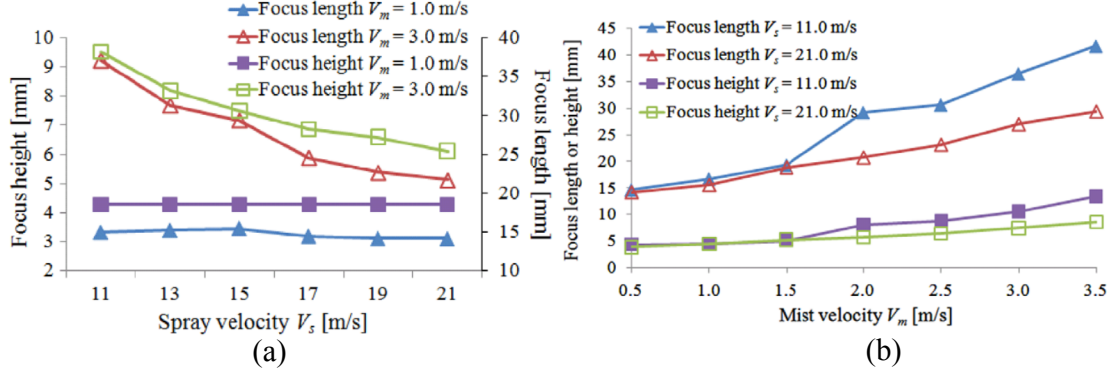
Figure 2.52: Effect of (a) droplet velocity and (b) gas velocity on focus length and focus height [29]

increase in gas velocity resulted in larger droplet entrainment angle, thereby producing a smaller droplet entrainment zone. An interesting observation in the study was the formation of a *core region* at near the exit of the nozzle unit where minimum flux of droplets exists. It is critical to ensure that the machining zone is not within this distance range from the nozzle because uniform distribution of droplets is essential for spreading and effective penetration into the too-chip interface. This is schematically shown in Fig. 2.54.

(a) $\theta_r = 43.26°$, FF ≥ 32 mm   **(b)** $\theta_r = 24.44°$, FF ≥ 24 mm

(c) $\theta_r = 55.0°$, FF ≥ 35 mm   **(d)** $\theta_r = 29.05°$, FF ≥ 30 mm
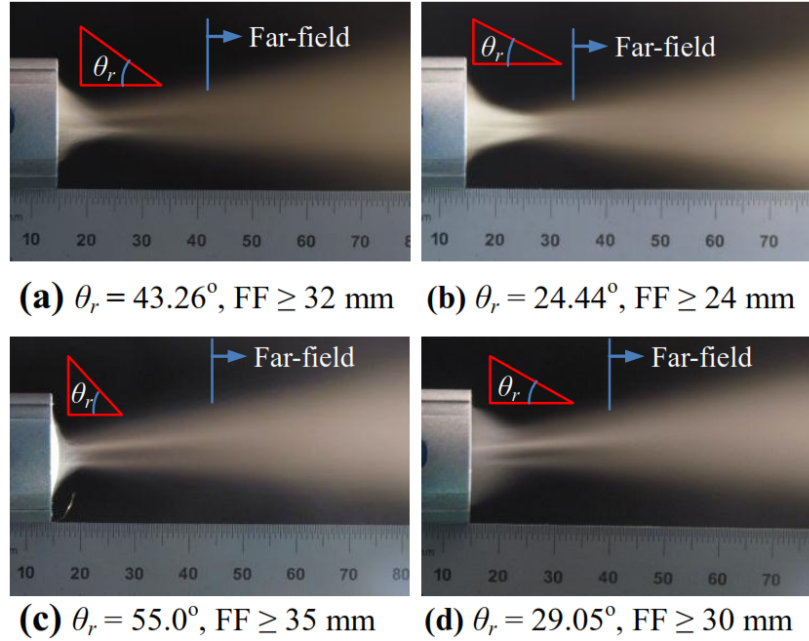
Figure 2.53: Photographs of spray for different droplet, U_d and gas velocity, U_g [26]
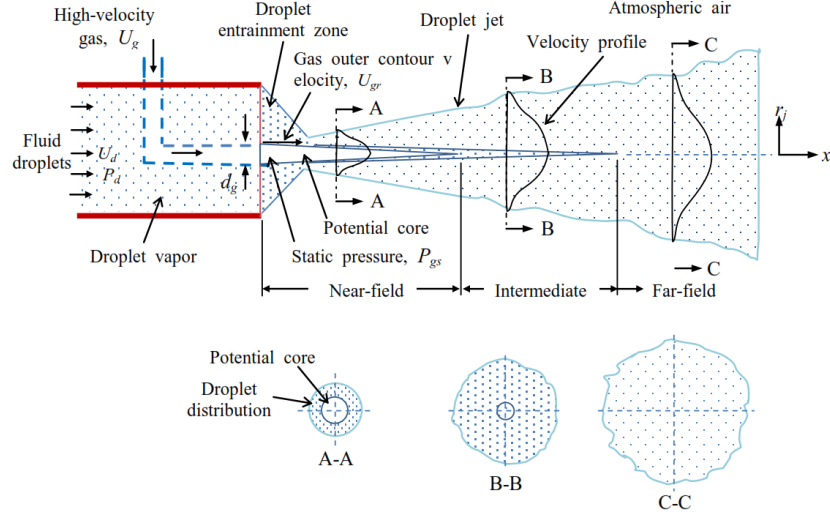
Figure 2.54: Schematic of the spray produced by high velocity gas [26]

A greater spray distance was observed to produce lesser tool wear because of the uniform flux of droplets across the cross-section of the spray and the absence of *potential core*. A uniform flux of droplets ensures that the film formed on the toll rake face penetrates the interface effectively, thereby providing superior cooling and lubrication performance. The flank wear was observed to be 0.721μm and 0.453μm after 8 minutes of machining for spray distance of 25 mm and 35 mm, respectively. A combination of larger spray distance, higher droplet velocity and smaller gas velocity was found to enhance tool life in titanium machining (see Fig. 2.55).

In order to study the effect of nozzle geometry and spray system parameters on the spray characteristics, a computational model would be helpful. Also, these studies did not determine the droplet velocity directly which would require extensive set up that are based on phase Doppler principle. A computational model will not only reduce the amount of time spent on evaluating different nozzle design iterations but also determine the droplet velocity variation along the spray distance taking the compressible flow of gas into account. There is no computational model to study the liquid spray and film formation using the ACF system till date and some of the available models for applications such as spray forming and spray coating processes are discussed below.

(a)   (b)
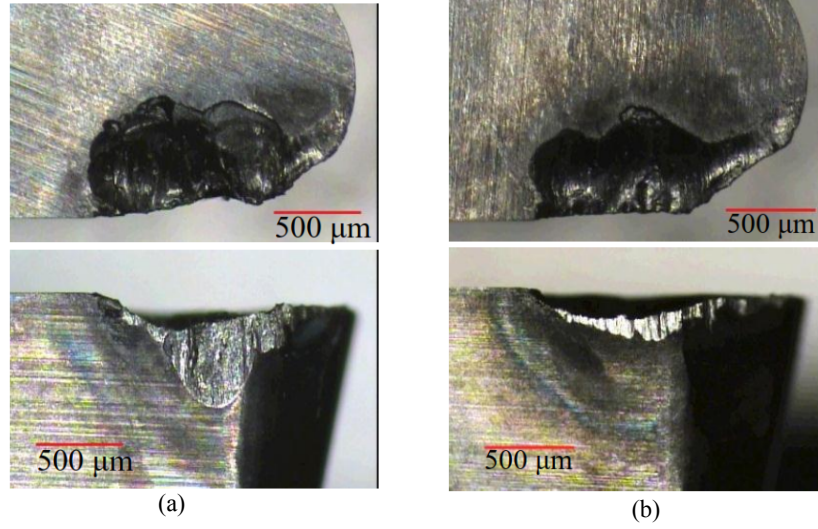
Figure 2.55: Tool rake and flank wear for (a) U_d= 0.2 m/s, U_g= 26 m/s, S_d= 25 mm and (b) U_d= 1.2 m/s, U_g= 26 m/s, S_d= 35 mm [26]

Boughner et. al. (2011) developed a mathematical model to determine the film thickness on a rotating cylindrical surface using an ACF spray system. The time to create a uniform micro-film on the surface and the thickness of the film were evaluated as a function of the fluid properties, droplet and gas velocities. The losses in the flow rate of fluid such as in the delivery tube, nozzle, rebound losses and evaporation of the fluid were quantified and film thickness was predicted. The film thickness, h_f was evaluated as,

$$h_f(t) = \frac{t * dV/dt}{A_{cylinder}} \qquad (2.8)$$

However, the assumptions in this model are too simplistic and does not consider several factors that are critical to modeling this phenomenon. The droplet velocity is assumed to be equal to the gas velocity and is only valid for regions that are farther form the nozzle exit. Since the distances between the nozzle and the machining region is typically small, especially in micro-machining applications this assumption severely affects the modeling of droplets in the carrier gas field. The loss of fluid droplets in the dielectric was assumed to be an arbitrary percentage of total flow rate of fluid. Also, the droplets are assumed to be impinging on a

dry surface during machining. While this is true for the initial stage of spray and film formation, droplets generated after the initial period impact a machining surface that has a layer of thin fluid film formed due to the impingement of earlier droplets. The validity of the model is restricted to lower gas velocities since compressible effects are not considered in the film modeling. The spatial variation in film formed on the surface is significant and cannot be assumed to have a uniform thickness throughout the surface.

Jeyakumar et. al. (2008) [30] studied the flow pattern of the atomizing gas in the spray deposition of Al 7075 alloy. A two-dimensional, steady state, axisymmetric model using compressible gas model was developed using commercial computational fluid dynamics code ANSYS Fluent^{TM}. The velocity field of the atomizing gas around the nozzle was studied for two different nozzle configurations. A nozzle design with a protrusion at the exit preferably around 2 or 3 mm enhanced the flow of the molten metal from the delivery tube since the location of the melt ejection coincided with the position of minimum aspiration pressure (see Fig. 2.56).

Though the model captured the trend of pressure variation for different protrusion lengths, a considerable deviation for the experimental values was observed (see Fig. 2.57). Also, the model did not study the droplets of metal and the formation of spray from the nozzle for improving the spray coating process. Hence the application of this model to study the spray and film formation on the machining surface is limited.

Mi et. al. (2008) [31] developed a two-dimensional, axisymmetrical model study the atomization, transport and deposition of droplets of IN718 Ni super-alloy in the spray forming process. After establishing the flow field due to the atomizing gas, the molten metal droplets were injected into the flow field with the appropriate size and velocity distribution. The subsequent droplet trajectory, heat transfer/momentum transfer were determined using the Discrete Phase Modeling (DPM) approach that is based on solving the force-balance equations of the droplets. The forces acting on the droplets including pressure gradient force and
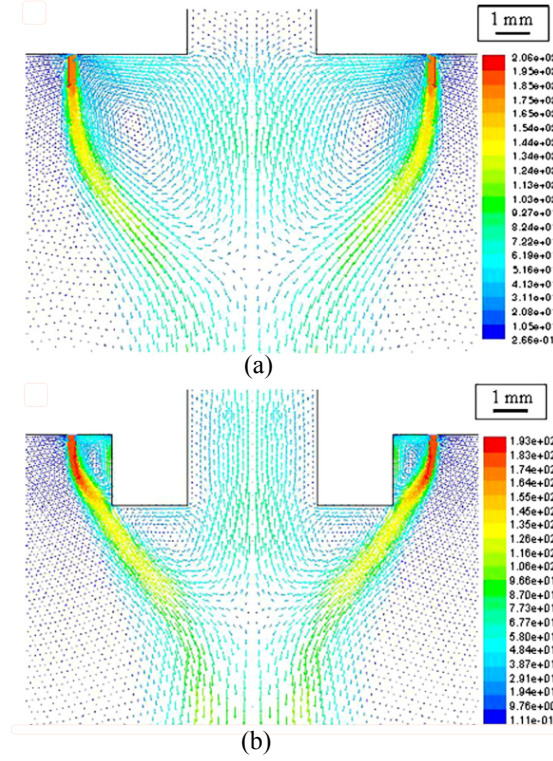
Figure 2.56: Velocity vector distribution for (a) nozzle without protrusion and (b) nozzle with protrusion [30]
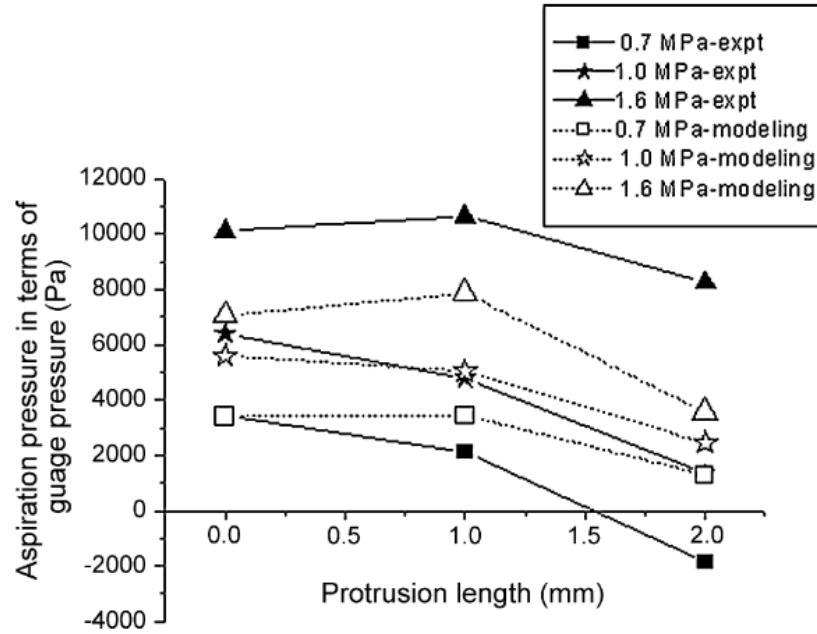
Figure 2.57: Comparison of experimental and model results for aspiration pressure at the tip of melt delivery tube [30]

drag force were considered in the model. Due to the coupling between the atomizing gas and the droplets, the effect of the gas pressure on droplet characteristics could be studied using this approach. The droplets were then impinged on the substrate surface to simulate the deposition process. The cross-section of the deposited material is shown in Fig. 2.58.
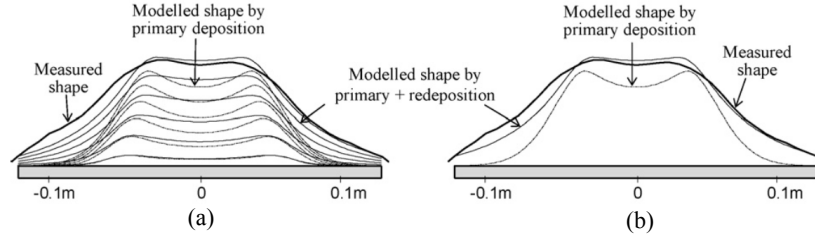
Figure 2.58: Cross-section of the deposited metal (a) every 40 revolutions of the target surface and (b) the end of spray forming [31]
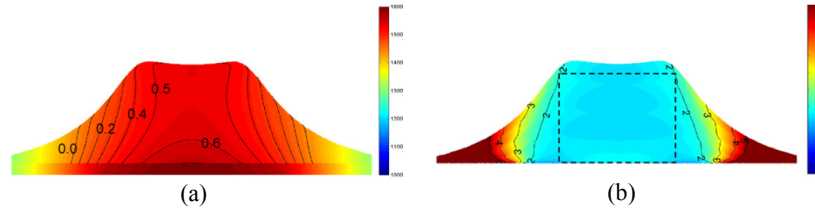
Figure 2.59: (a) Internal heat flow in deposited material after spray forming (b) the simulated porosity distribution [31]

However, their model used only one-way coupling between the gas and the metal droplets (the effect of droplets on gas field was assumed to be negligible). Also, the collision and coalescence among droplets in the spray was ignored in the model.

Khatami et. al. (2011) [107] developed a two-dimensional model to study the Chemical Spray Pyrolysis (CSP) technique for manufacturing mixed metal nano-composite films that are widely used for sensor applications. The droplets of precursor material in the nanometer range are produced by atomization through a nozzle prior to impinging the substrate. The aerosol model studied the effect of synthesis parameters that affects the droplet characteristics during the deposition process. It was observed that higher mass flow rate produces droplets with high

61

proportion of the solvent material. Also, swirl motion around the spray inlet enhances radial spread of droplets and reduces the size of the droplets. However, the actual deposition of the droplets on the substrate was not simulated since film formation was not incorporated in the computational model.

Weiner et. al. (1993) [32] studied the dispersion of liquid droplets from an air-assisted sprayer. A two-dimensional model was developed initially and later extended to three dimensions. The gas velocity was experimentally determined using an ultrasonic anemometer which simultaneously measures velocity in three directions. Though satisfactory agreement was observed between the experimental and model predictions of the center-line gas velocity, the rate of exponential decay fits closely for distances less than 3m (see Fig. 2.60). The droplet trajectories were evaluated using the DPM approach but the collision and coalescence was not taken into consideration in their model. The size of the droplets studied was around 250μm which is significantly larger than that encountered in the ACF spray system.
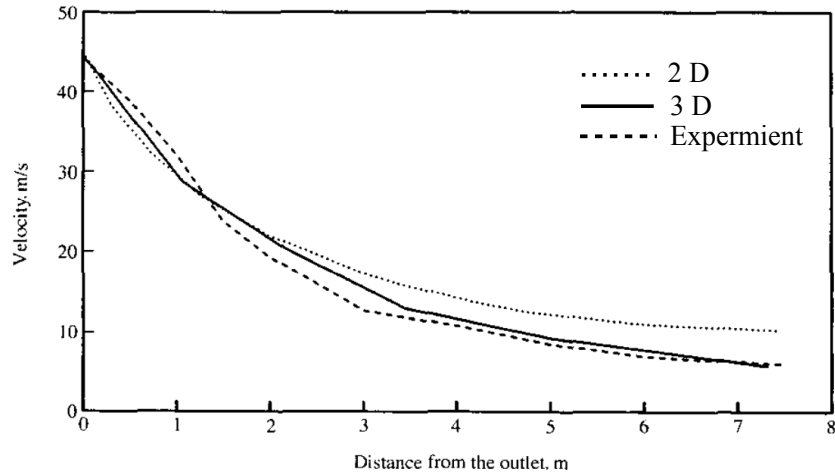
Figure 2.60: Comparison of experimental and model results of center-line velocities of gas [32]

Ellwood and Braslaw [33] developed a finite-element model to study the electrostatic spray coating process using a rotary bell atomizer. Their study was aimed at improving the transfer efficiencies of the paint spray from the atomizer to the electrically ground target by changing the parameters of the bell atomizer.

An iterative particle source in cell (PSIC) approach was used to compute the spray pattern and the momentum transfer between the gas phase and the paint droplets. The three-dimensional geometry, streamlines of the gas and the electric field due to the potential between the atomizer and the ground target is shown in Fig. 2.61. The charged paint droplets influence this electric field and are observed to improve the flux of droplets impacting the desired regions on target surface.
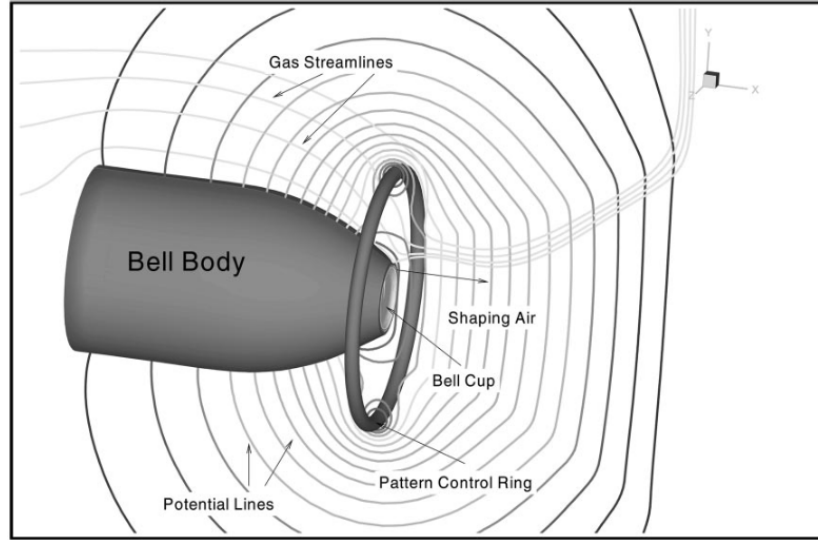
Figure 2.61: Steady state flow conditions around the rotary bell without the paint droplets [33]

However, unlike this model, the dielectric spray in Spray-EDM is not subject to electric potential. Also, the computational model developed does not study the droplet-surface interaction phenomenon to predict the characteristics of the film formed on the target surface. The gas flow field and particle trajectories are assumed to be axisymmetric unlike the actual scenario.

Burger et. al. (2002) [34] developed a hybrid model combining both Eulerian and Lagrangian approaches to study the fuel injection, dispersion and evaporation in the intake manifold of an IC engine. The hybrid model provided an optimal balance between time and accuracy. An initial solution to the flow field with fuel was obtained using the Eulerian approach and then a more accurate representation of the droplet trajectories was determined using the Lagrangian approach (see
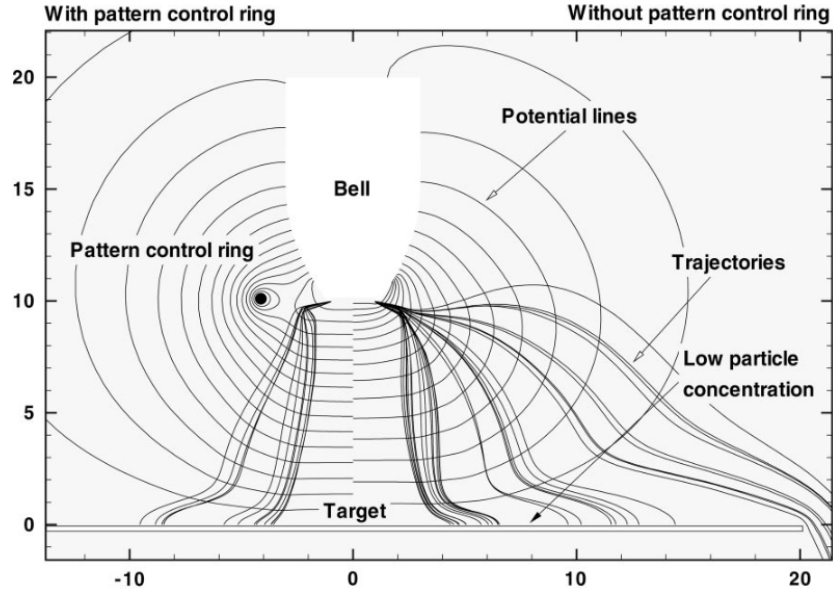
Figure 2.62: Comparison of paint droplets' trajectories with (left) and without (right) pattern control ring [33]

Fig. 2.63). The comparison of the droplet velocity for the two approaches shows that the Lagrangian model predictions are closer to the experimental values (see Fig. 2.64). This is attributed to the ability of this model to track the droplet particles in the gas field individually and not as a continuous secondary phase.

Although this model considers the interaction of the droplets with the walls of the engine cylinder, the phenomenon of film formation is not pertinent in this case. This is because the temperatures are well above the Leidenfrost point and only the splashing of fuel droplets to generate secondary droplets was included in the model to predict droplet velocities.

Colbert and Cairncross [35] developed a three-dimensional model to study the paint droplet transport in an electrostatic coating process that included the effect of charge accumulation on coating thickness of the target surfaces. A sample spray pattern on the target surface and coating thickness profile is shown in Fig. 2.65. The trajectories of smaller droplets are dominated by drag and follows the air stream path closely. On the other hand, the larger droplets that are entrained in th air stream have momentum that is sufficient to enable deposition on the
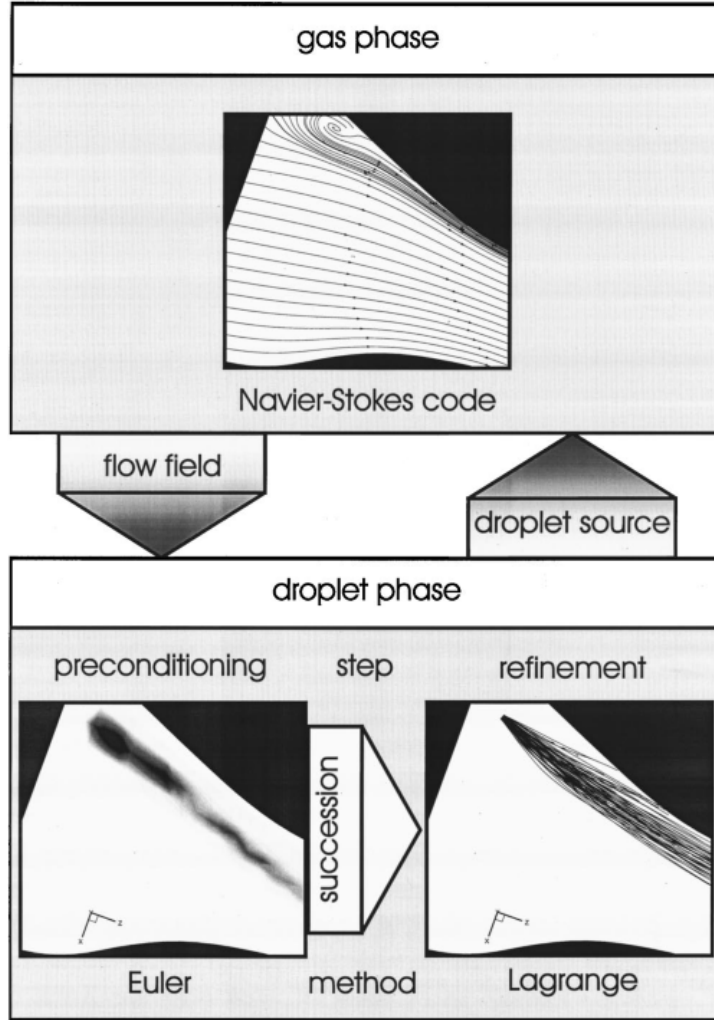
Figure 2.63: Structure of the hybrid model [34]

surface leading to a *dot pattern* or a *ring pattern*. However, a dilute droplet concentration was assumed in the model and interaction between droplets and influence of droplets on the gas phase was not included. This assumption is invalid in critical regions such as the exit of the rotary sprayer.

Thus, to the best of the author's knowledge, there are no computational models available in literature to understand the complex phenomena of spray formation and transport, spray-surface interaction and film formation in atomized-fluid spray systems for machining applications. The combination of an ultrasonic atomizer and a nozzle system to focus the fluid droplets prior to deposition is unique to ACF systems and necessitates the development of a new computational model
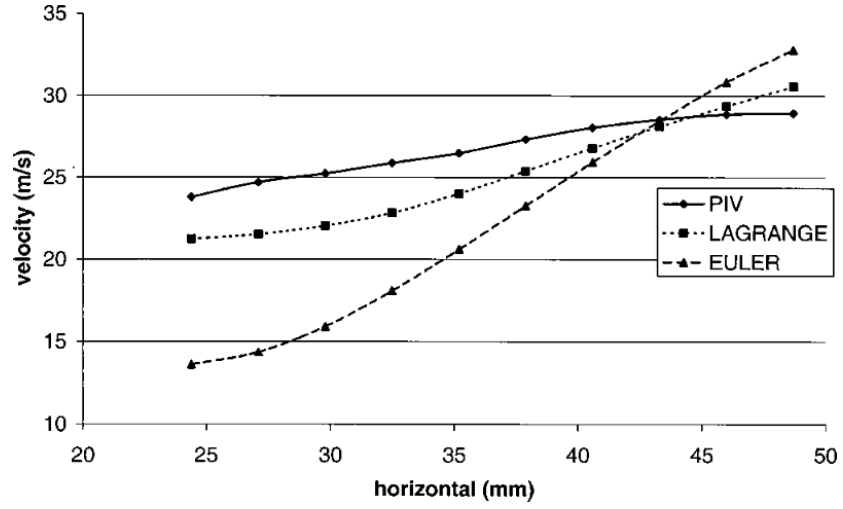
Figure 2.64: Comparison of droplet velocity using different approaches [34]

Ring pattern   Dot pattern
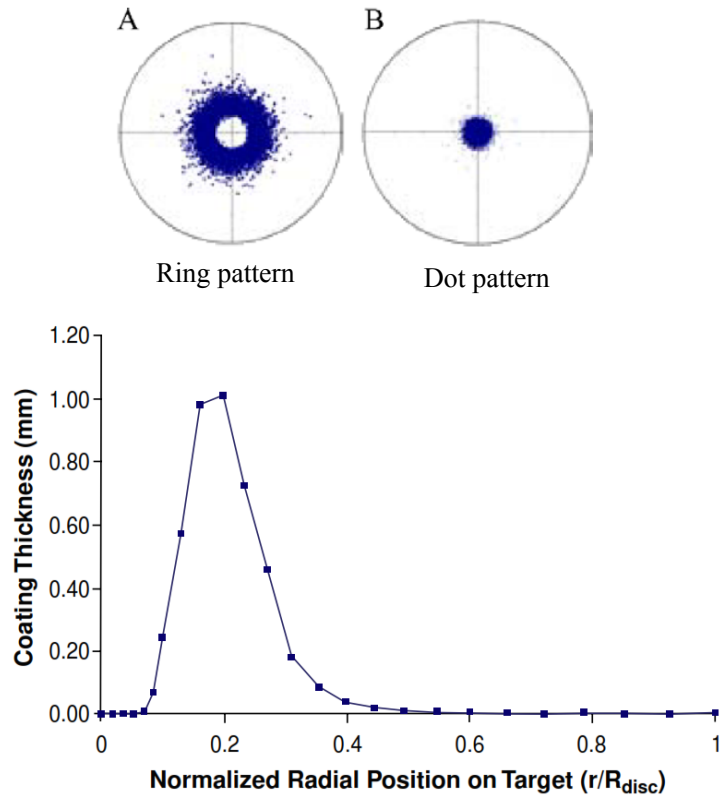
Figure 2.65: Spray patterns and film thickness profiles [35]

to understand and improve the design of spray system.

2.6   Gaps in Knowledge

The consumption of large quantities of hydrocarbon oils in EDM poses significant health and environmental hazards. Though several techniques including dry and near-dry EDM have been developed to minimize dielectric consumption, the flushing ability in these processes is reduced due the lower viscosity of the dielectric. Also, the jet flushing methods currently in practice are not suitable for certain EDM processes such as wire-EDM and micro-EDM due to the excessive deflection of the tool.

A fundamental knowledge base for the proposed Spray-EDM process does not exist. A complete understanding of droplet atomization, dielectric spray formation, thin film formation and debris flushing using a thin dielectric film is essential for developing the Spray-EDM process. Though the use of an ultrasonic atomizer with a nozzle system is similar to the ACF system, a computational model that thoroughly investigates the aforementioned phenomena in ACF system has not been developed. This is attributed to the multi-length scale and multi-time scale phenomena involved in the spray and film formation processes. The current models do not estimate the characteristics of the film formed on the machining surface in three dimensions. Also, the compressibility effects associated with the flow of the carrier gas through the nozzle unit have been ignored. The collision and coalescence among the droplets of dielectric fluid have not been considered in these studies.

The use of a thin dielectric film to flush debris from the inter-electrode gap in EDM has not been investigated. The Spray-EDM process is different from other techniques in that a thin film of dielectric is used in this process and not a bulk liquid medium as encountered in other EDM techniques. The existing models related to debris flushing in EDM do not take into account critical process-related factors including plasma pressure, actual topography of the machined surface and non-uniform size of debris particles.

Chapter 3

Spray-EDM : Concept and Modeling

In order to develop an efficient Spray-EDM process, it is essential to understand the role of spray system parameters on dielectric film formation on the workpiece surface and debris flushing from the inter-electrode gap. The phenomena in Spray-EDM including film formation and flushing are within micro-scale domain and are better understood through a computational modeling approach. The modeling of Spray-EDM process is inherently a multi-physics problem involving multi-length (μm to m) and multi-time (μs to s) scale transport phenomena, which presents a significant challenge in modeling Spray-EDM process. In this chapter, the concept of Spray-EDM including the working principle is discussed first, followed by a discussion on the modeling of dielectric spray formation, film formation and debris flushing.

3.1 Spray-EDM : Development of Concept

A schematic of the spray system used for EDM process is shown in Fig. 3.1. The spray system is used to generate the dielectric spray using an ultrasonic atomizer placed within the housing. The distance of the spray system from the machining surface and the angle of impingement are controlled using the mounting frame. The dielectric droplets from the spray system form a thin film on impacting the surface of the workpiece. The thin dielectric film penetrates the gap between the tool electrode and the workpiece.

The critical component of Spray-EDM is the atomizer system that functions as a stand-alone unit to produce and control the atomized dielectric droplets. An
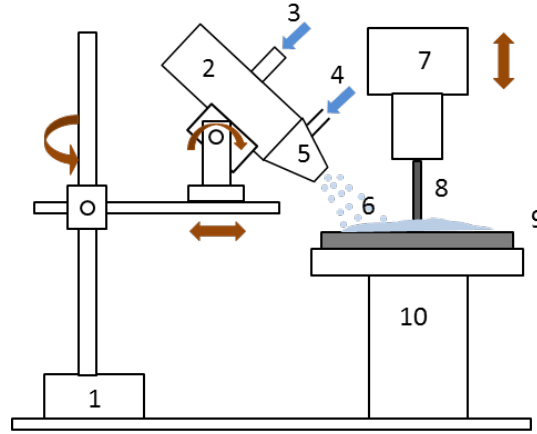
Figure 3.1: Schematic of Spray-EDM setup. 1: Mounting frame, 2: Ultrasonic atomizer housing, 3: Dielectric fluid inlet, 4: High pressure gas inlet, 5: Nozzle assembly, 6: Dielectric film, 7: Gap controlling system, 8: Tool electrode, 9: Work piece, 10: Workpiece mounting stage

ultrasonic atomizer (Model VC5040AT, Sonic and Materials, Inc., USA) with an operating frequency of 40 kHz and producing droplets with mean diameter, d_m of 60 μm is encapsulated in a circular pipe. The dynamic viscosity of the medium has to be below 0.05 Ns/m^2 for optimum atomization [108]. The atomizer spray system is shown in Fig. 3.2.
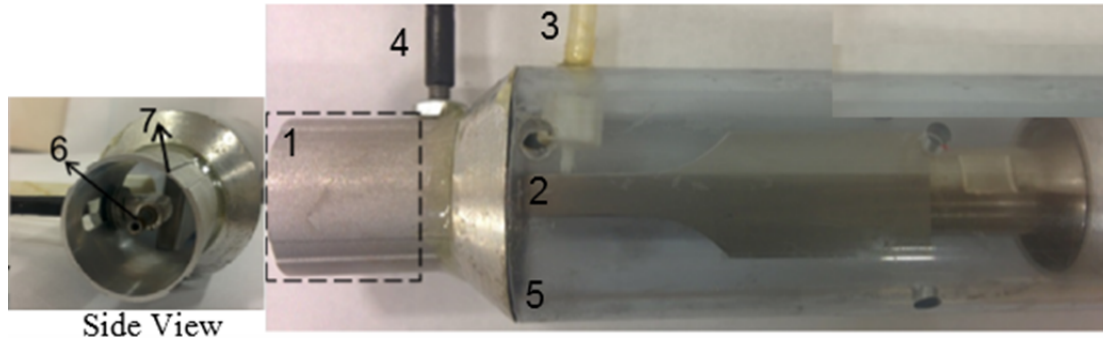
Figure 3.2: Spray system with ultrasonic atomizer and nozzle unit. 1: Nozzle assembly, 2: Atomizer tip, 3: Dielectric fluid inlet, 4: High pressure gas inlet, 5: Plastic housing, 6: Carrier gas nozzle, 7: Droplet nozzle

The dielectric fluid is supplied from an external reservoir through a plastic tube so that it impacts the tip of the atomizer horn for effective break-up into droplets. The droplets are then focused into a narrow jet using a nozzle unit that consists of two co-axial nozzles attached to the front portion of the pipe. The outer nozzle

(droplet nozzle) carries the atomized droplets while the inner nozzle (gas nozzle) carries high pressure carrier gas (air) to obtain a focused stream of droplets for application to the machining region. The convergence angles of the droplet and gas nozzles are selected as 40° and 0.75°, respectively for effective entrapment of the droplets, thus preventing the excessive divergence of the droplet spray [26].

The geometry of the nozzle unit used in the Spray-EDM process is shown in Fig. 3.3. The outer droplet nozzle has a converging section of length 25 mm and a gas nozzle (carrying high pressure gas) is placed co-axially inside it. The droplets from the ultrasonic atomizer are transported through the droplet nozzle and are accelerated when they reach the tip of gas nozzle. The exit of gas nozzle is set within the droplet nozzle (by 3 mm) for better focusing of the dielectric spray formed [29]. The distance from the exit of droplet nozzle to the target surface (spray length) and the impingement angle determine the normal component of droplet velocity on impact that governs the droplet-surface interaction phenomenon.

The formation of dielectric film on the surface of the workpiece is schematically shown in Fig. 3.4. Droplets produced by the spray system impinge the work surface at a distance, d_s from the machining zone to form a thin film of dielectric with a certain thickness (h_f) and velocity (v_f). Both h_f and v_f vary along machining surface. This dielectric film penetrates the inter-electrode gap to perform the primary functions of the dielectric in EDM, viz., to act as the sparking medium between the electrodes for discharges, to effectively remove the debris from the discharge gap and carry away heat along with it. [56]. A thin film of dielectric is sufficient to perform these functions instead of using a large quantity of dielectric. This is because only the volume of dielectric within the inter-electrode gap takes part in the discharge process in EDM and the remaining dielectric fluid does not play an effective role in the process. In addition to reducing dielectric consumption, the motion of dielectric film may have a better flushing ability compared to stationary dielectric and may remove debris particles from the discharge zone effectively. Improvement in debris flushing could also reduce the frequency of
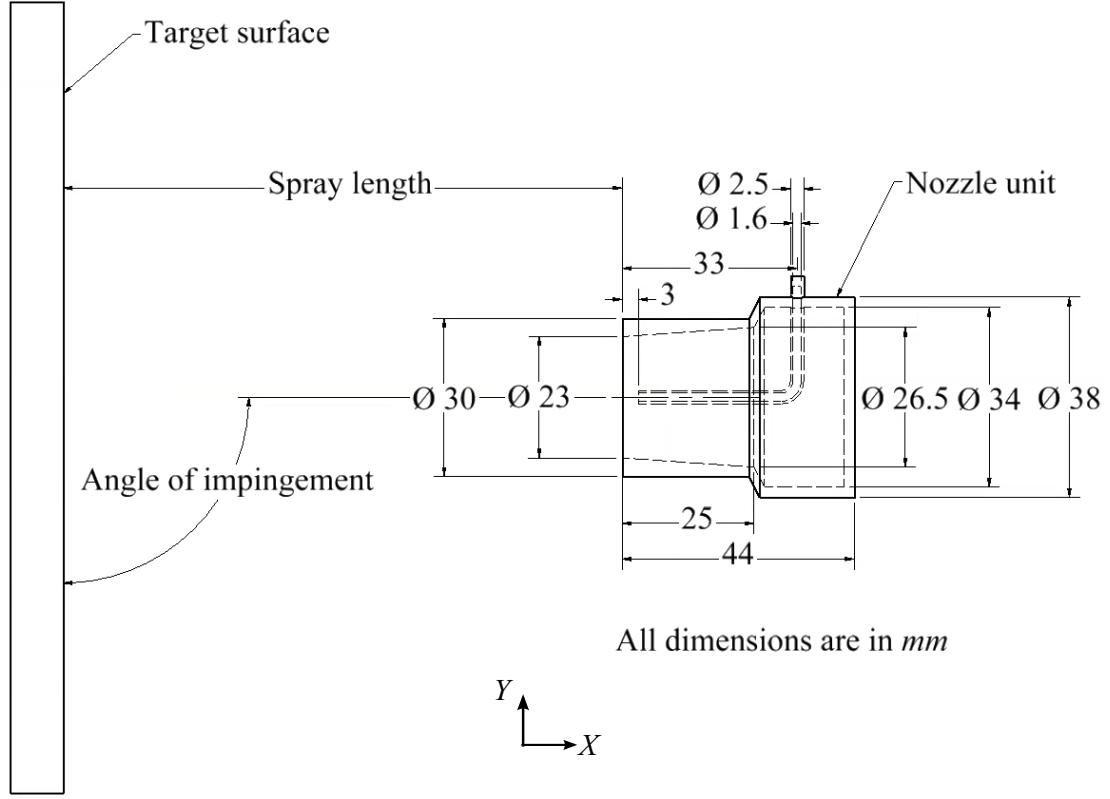
Figure 3.3: Geometry of the nozzle used in Spray-EDM

short-circuiting in EDM.

The formation of dielectric film due to spray impingement in Spray-EDM is governed by the droplet-surface interaction [102]. The outcome of droplet impact on a surface depends on the parameters such as droplet diameter (d_d), droplet velocity (v_d) and liquid properties such as dynamic viscosity (μ_d), density (ρ_d) and surface tension (σ_d). Depending on the aforementioned factors, the spray-surface interaction on a solid surface may correspond to one of the four regimes, viz., (i) stick, (ii) rebound, (iii) spread and (iv) splash. Since the impact process is affected by a large number of fluid properties and impingement conditions, these regimes are characterized by non-dimensional numbers such as Weber number (We), Reynolds number (Re), Ohnesorge number (Oh) and K_y [28]. Among the four regimes, for effective film formation and penetration of the dielectric into the discharge gap in the Spray-EDM process, the droplet interaction has to be in the spreading regime.

71
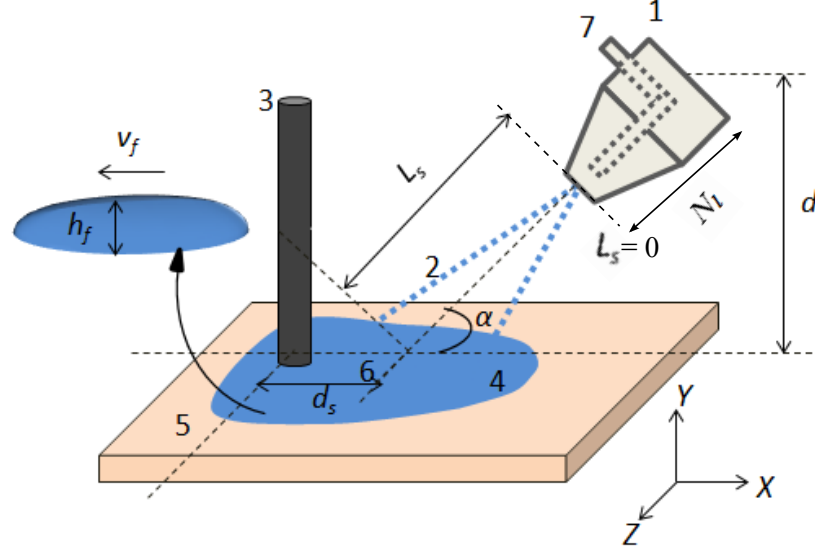
Figure 3.4: Schematic of spray parameters. 1: Nozzle with atomizer, 2: Dielectric spray, 3: Tool electrode, 4: Dielectric film, 5: Workpiece, 6: Point of spray impingement, 7: Carrier gas inlet, L_s: Distance from droplet nozzle exit, d_s: Distance of electrode from the point of spray impingement, N_l: Length of nozzle unit, α: Angle of spray impingement in XY plane

Also, the dielectric should completely fill up the inter-electrode gap (d_{gap}) since the presence of an air gap influences the discharge process and reduces the volume of material removed [8]. Hence, the film thickness should always be greater than the inter-electrode gap $(h_f \geq d_{gap})$. In addition, the film velocity (v_f) should be such that the flowing film effectively removes the debris. However the velocity of droplets cannot be higher than a particular value since droplets will then splash, preventing the film formation on the machined surface. Therefore it is critical to choose the right combination of spray parameters that will ensure formation of dielectric film on the machining surface.

The proposed method is different from near-dry EDM in that the dielectric is made of only one phase (liquid) in the form of a thin film and not a mixture of liquid and gas that is applied to discharge zone. The formation of a thin dielectric film that penetrates the inter-electrode gap and effectively flushes the debris is a unique characteristic of the proposed method. Lower MRR and higher thermal load on electrodes observed in near-dry EDM compared to Wet-EDM

72

is also overcome in Spray-EDM because there is no reduction in the effective viscosity and heat-removal capability of the dielectric by mixing with a gas phase. Also, the presence of high viscosity dielectric within the inter-electrode gap focuses the electrical discharges to a narrow region by confining the expansion of plasma channel.

The mechanism of material removal in EDM process with atomized dielectric is schematically represented in Fig. 3.5. A clean dielectric film (without any debris particles) penetrates the micro-level discharge gap between tool and workpiece electrodes. When a large voltage is applied across the electrodes over a small duration (order of micro-seconds), a high intensity electric field is generated within the gap. This overcomes the dielectric strength of the medium and leads to the breakdown of dielectric. As a result a plasma channel consisting of electrons, positive ions and neutral species is formed between electrodes. The current across the electrodes rises due to the motion of ions towards the electrodes with opposite polarity and results in the generation of an avalanche of charged particles. The intense heat of plasma melts a small portion of material on the surface of electrodes. When the applied voltage is turned off, the plasma channel collapses due to the pressure exerted by the surrounding dielectric liquid. This implosion removes the molten material from the electrodes in the form of debris particles and forms a crater on the electrode surface. The motion of dielectric film removes debris particles from the machining region and a fresh influx of dielectric liquid occupies the inter-electrode volume. One of the important characteristics of this method compared to the conventional EDM is the reduction in frequency of short-circuiting due to better flushing capability of the moving dielectric film. The moving film also has a better heat removal capability compared to stationary dielectric and reduces the temperature of tool electrode effectively. This will result in reduced tool electrode wear compared to conventional method. Finally, the gap becomes insulating again as the dielectric strength is recovered and the process is repeated for subsequent discharges.
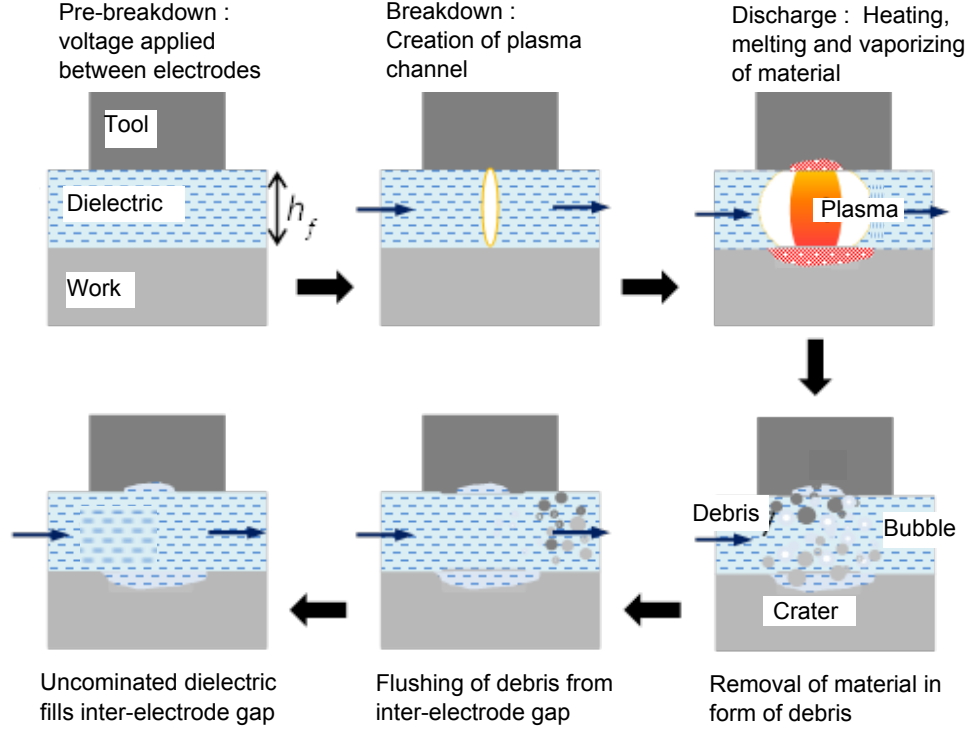
Figure 3.5: Schematic of material removal in Spray-EDM process.

3.2 Modeling Approach

In order to study debris flushing in Spray-EDM through Computational Fluid Dynamics (CFD) approach, three models, viz., (i) dielectric spray model, (ii) film formation model and (iii) debris flushing model are developed. A schematic of the modeling approach along with input and output parameters for each model is shown in Fig. 3.6.

The characteristics of the dielectric spray are influenced by the properties of dielectric medium including density and viscosity, carrier gas pressure, impingement angle, mass flow rate of dielectric and size of dielectric droplets and geometry of the nozzle. The dielectric spray model is used to determine the velocity of the carrier gas and the dielectric droplets at various distances from the nozzle exit along its axis. This model includes the compressible flow of carrier gas and the interaction between the dielectric droplets and the carrier gas. The break up and coalescence among droplets are also taken into account. Using the results

Dielectric properties,
spray parameters,
nozzle geometry $\longrightarrow$ Dielectric Spray Model

Carrier gas velocity, dielectric droplets velocity

Range of impingement angles and
distance from nozzle exit for spreading regime

Film Formation Model

Film thickness and velocity on machining surface

Plasma pressure and
radius, debris size $\longrightarrow$ Debris Flushing Model
and velocity,
material properties

Distribution of debris particles around crater

Figure 3.6: Modeling methodology of Spray-EDM

from the dielectric spray model, the range of impingement angles and distances from nozzle exit that ensure the droplet-surface interaction is within the spreading regime are estimated. The film formation model is developed using the Eulerian Wall Film (EWF) approach to estimate the film characteristics. The EWF approach accounts for the mass and momentum transfer from the dielectric droplets in the spray to the film formed on the machining surface. The impingement of droplets on a thin layer of dielectric, film spreading due to gravity and surface tension effects are included in this model. Using the model, a three-dimensional profile of film is obtained and h_f and v_f for different combinations of gas pressure, impingement angle and distance from nozzle exit are determined.

The debris flushing model is developed to predict the trajectory of debris by taking into account plasma pressure and radius, non-uniform debris size distribution, debris velocity, density of workpiece material and actual topography of the machined crater. The trajectory of debris particles is obtained using the Discrete Phase Modeling (DPM) approach that is based on solving force-balance equations of the individual debris particles in a Lagrangian reference frame. The

debris flushing model is used to evaluate the effectiveness of debris flushing using Spray-EDM for different combinations of spray system parameters.

3.3 Dielectric Spray Model

The objective of the dielectric spray model is to determine the range of impingement angles and distances from the nozzle exit that can be used in Spray-EDM process. It is a three-dimensional, steady-state, turbulent flow model developed using Ansys Fluent$^{\text{TM}}$. It is based on the Discrete Phase Model (DPM) that solves the trajectory of dielectric droplets (secondary phase) dispersed in carrier gas (primary phase) by considering the interaction between the two phases. The DPM approach is applicable for modeling Spray-EDM process since the volume fraction of the droplets is lesser than 10% of the carrier gas [109]. A similar approach has been implemented to study the spray coating and spray forming processes in Refs. [107, 30, 32]. However, only the droplet spray characteristics were investigated and the deposition and film formation on the substrate were not considered in their studies. In this research, modeling dielectric sprays is done in two steps. First, the steady state flow field of the carrier gas is established by solving the Navier-Stokes equation in three dimensions. Then, the dielectric droplets are injected into the computational domain to study the effect of continuum flow field on the droplet trajectories.

3.3.1 Model Description

Compressible flow model for carrier gas

In order to take the compressibility effects of the carrier gas (air) at high pressures, the ideal gas law is used to compute the density variation. The pressure-based solver with coupled algorithm for pressure-velocity coupling is a good alternative to the density-based solvers for modeling compressible flows in Fluent,

especially for steady cases with significant low-speed flow regions [110]. Hence this formulation is used in the current model. Also, the energy equation and viscous dissipation terms are activated for accurate modeling of compressible flow [109]. The Shear-Stress Transport (SST) $k - \omega$ model yields more accurate and reliable results for flows with adverse pressure gradients such as that encountered in the current study and is used for modeling turbulence [111]. Least squares cell-based gradient discretization is preferred over other gradient methods since it is less computationally expensive and offers the same accuracy as other methods for unstructured meshes [111]. The second-order and higher-order schemes for pressure terms, and second-order upwind interpolation scheme for density and momentum are implemented for accurate modeling of carrier gas flow field. The use of aforementioned higher-order spatial discretization schemes necessitates the implementation of Higher-Order Term Relaxation (HOTR) with a relaxation factor of 0.25 for flow variables in order to improve the startup of solution and reduce numerical instabilities [109].

Interaction between dielectric droplets and carrier gas

After determining the flow field of the carrier gas, the trajectories of dielectric droplets (Chem Finish EDM oil) in carrier gas are determined by using the DPM approach. It is based on Lagrangian formulation that enables the individual tracking of droplets at specified intervals during the fluid phase computation [111]. The trajectory of the droplets is determined by integrating the force balance on each droplet given by,

$$\frac{d\vec{v_d}}{dt} \ = \ F_D(\vec{u} - \vec{v_d}) \ + \ \frac{\vec{g}(\rho \ - \ \rho_d)}{\rho_d} \ + \ \vec{F}, \qquad (3.1)$$

where, $\vec{u}$ and ρ are velocity and density of the carrier gas, $\vec{v_d}$ and ρ_d are velocity and density of the dielectric droplet, $\vec{F}$ is an additional acceleration term on the droplets due to virtual mass force, thermophoretic force or Saffman's lift force, all

of which are negligible in this case and $\vec{g}$ is the acceleration due to gravity [111]. $F_D(\vec{u} - \vec{v_d})$ is the drag force per unit mass and F_D is given as,

$$F_D = \frac{18\mu}{\rho_d\, d_d^2}\frac{C_D\ Re}{24},\tag{3.2}$$

where, μ is the dynamic viscosity of the carrier gas, d_d is the diameter of the dielectric droplet and C_D is the drag coefficient. The relative Reynold's number, Re is defined as,

$$Re \equiv \frac{\rho\ d_d|\vec{v_d} - \vec{u}|}{\mu}.\tag{3.3}$$

Considering the droplets to be smooth particles in the primary phase, the spherical drag law is used to evaluate the drag coefficient, C_D as

$$C_D = a_1 + \frac{a_2}{Re} + \frac{a_3}{Re^2},\tag{3.4}$$

where, the constants a_1, a_2 and a_3 are obtained from Morsi and Alexander [112] for the specific range of Re. Stochastic collision and coalescence among the droplets are also included. When the droplet oscillations reach a critical value while being transported by the high velocity air, they breakup into secondary droplets. The Taylor Analogy Breakup (TAB) model is used to simulate the breakup of droplets as they are transported by the carrier gas towards the target substrate [111].

Computational domain and meshing

A rectangular box is taken as the computational domain for the dielectric spray model as shown in Fig. 3.7. The nozzle unit consisting of both the droplet nozzle and the gas nozzle is considered along with the target surface that is a flat rectangular plate. The dimensions of the rectangular box are chosen such that the spatial variation in gas velocity from the nozzle exit does not vary by more than 1% with the size of computational domain. The domain is meshed with about 4 million cells. The mesh is refined in the region of dielectric spray using a

cylinder extending from the exit of the droplet nozzle as a 'body of influence' for determining the spatial variation in droplet velocity with good resolution. Since the orthogonal quality of the mesh plays a significant role in the accuracy and stability of numerical computation, the *improve-quality* text command is executed multiple times to improve the cells with lowest orthogonal quality [109]. The Reverse Cuthill-Mckee algorithm is used to reduce the bandwidth by a factor of 85 and to increase the memory access efficiency, thereby improving the computational performance of the solver. A grid independence study is performed to ensure that dependence of the simulation results on the grid size was less than 1%.
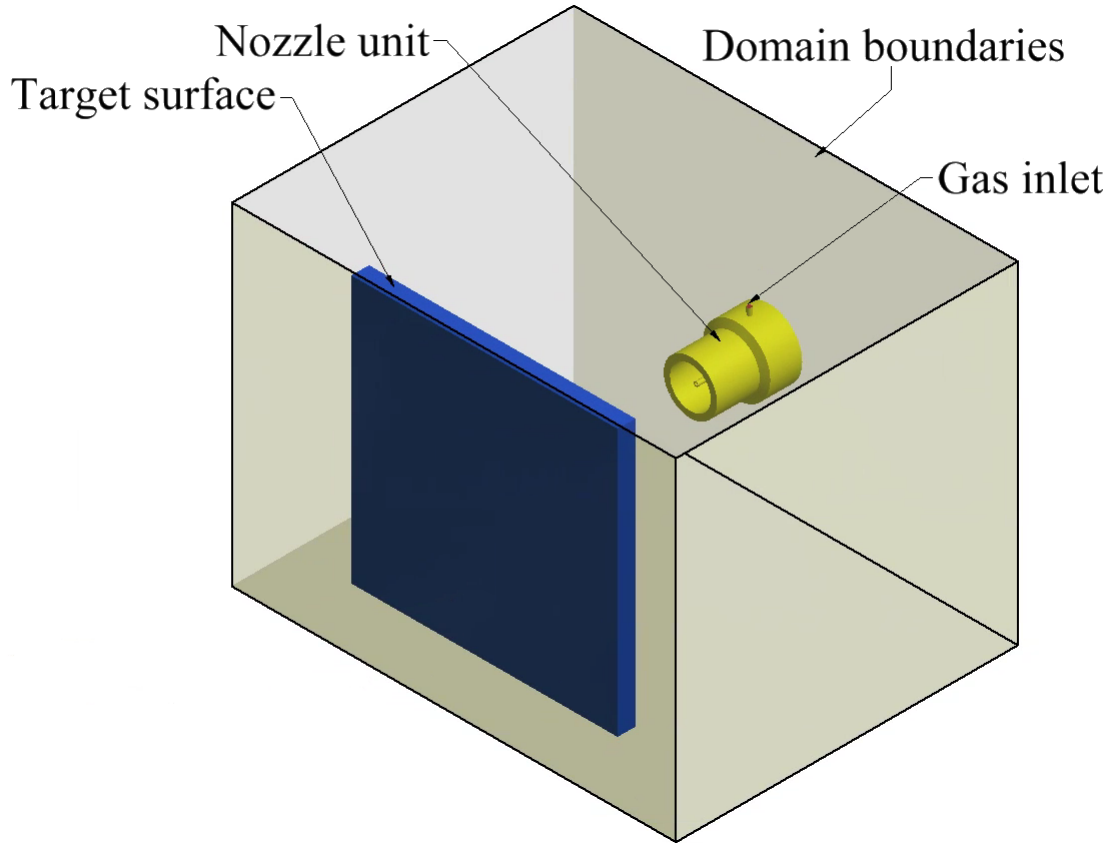
Figure 3.7: Schematic of computational domain for dielectric spray model

Boundary conditions

The inlet to the gas nozzle is modeled as a pressure inlet condition, which is varied to determine the spray characteristics for different carrier gas pressures. The flow of the gas is assumed to be normal to this boundary. The turbulent intensity and viscosity ratio are set to 1.5 and 10, respectively on this boundary. The temperature of the gas at the inlet is set to 300 K, which is the ambient temperature. The surfaces of the nozzle unit and the target are set as stationary walls with no-slip boundaries for velocity components. Since the heat transfer between these surfaces and the ambient is insignificant in this study, these walls are also assumed to be at the ambient temperature of 300 K. The boundaries of the rectangular domain are assumed to be pressure outlets with atmospheric pressure and turbulent intensity and viscosity ratio of unity since they are sufficiently far from the spray to have any effect on the numerical solution.

Droplets of dielectric fluid corresponding to the given flow rate are injected into the domain. Rosin-Rammler distribution used for defining the size distribution of the injected dielectric droplets is given as,

$$Y_{d_d} = e^{-(d_d/d_{d,mean})^n}, \tag{3.5}$$

where, Y_{d_d} is the mass fraction of droplets with diameter greater than d_d, $d_{d,mean}$ is the mean droplet size and n is the size distribution parameter and is taken as 3.5 for the ultrasonic atomization method [111]. The mean diameter of the dielectric droplets produced by the atomizer is calculated from the fluid properties and the frequency of the ultrasonic atomizer, f using the Lang formula [103] as,

$$d_{d,mean} = 0.73 \left(\frac{\sigma_d}{\rho_d f^2} \right)^{1/3}. \tag{3.6}$$

In the current study, $d_{d,mean}$ is found to be about 50 μm for $f = 40$ kHz and commercial EDM oil using Eqn. 3.6. The flow rate of the dielectric is set to 10 ml/min and the initial velocity of droplets is assumed to be 3 m/s. The boundary

conditions for solving the force-balance equations on the particles are shown in Tab. 3.1. The tracking of droplets is aborted when they are carried beyond the domain boundaries. In order to model the film formation phenomenon, the target surface is given a trap boundary condition to facilitate mass and momentum transfer from the droplets to the dielectric film formed on the machining surface.

Table 3.1: Boundary conditions (BC) for the dielectric spray model

Name	Fluid BC	DPM BC
Domain boundaries	Pressure outlet (0 Gage pressure)	Escape
Gas inlet	Pressure inlet	Escape
Nozzle unit	Stationary wall (No-slip)	Reflect
Target surface	Stationary wall (No-slip)	Trap

3.3.2 Validation of Dielectric Spray Model

The velocity of the carrier gas from the nozzle unit used in the Spray-EDM process plays a crucial role in determining the droplet velocity and hence the spreading of the dielectric film on the machining surface. The determination of droplet velocities by experimental methods is usually difficult and hence the validation of the model by comparing gas velocities has been performed. In this study, the variation of gas velocity along the distance from exit of the droplet nozzle predicted from the computational model is compared with those obtained from the experiments using the set up shown in Fig. 3.8. Experiments were performed using a Pitot-Static tube (Model PDA-18-F-16-KL, United Sensor Corp., USA) with a sensing stem diameter of 1/16″ to measure the dynamic pressure and thereby compute the gas velocity at a specific distance from the nozzle exit. The nozzle unit was mounted on precision XYZ motion stages to achieve the perfect alignment between the centers of the gas nozzle and the pitot tube. The dynamic pressure was measured using a digital manometer (HHP-2082, Omega Engineering Inc., USA) while the nozzle was translated to different positions along the

axial direction. The experiment was repeated thrice for gas pressures of 0.2, 0.4 and 0.6 MPa, respectively.
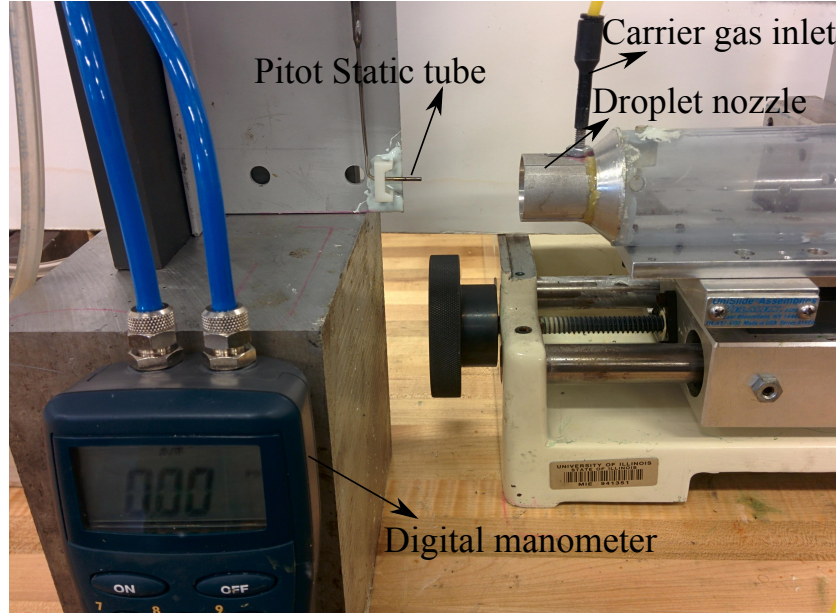
Figure 3.8: Experimental set up for determination of carrier gas velocity

The velocity vector field of the carrier gas as predicted by the dielectric spray model for different carrier gas pressures is shown in Fig. 3.9. The maximum velocity of the carrier gas occurs at the tip of the gas nozzle exit. The maximum velocity is found to be about 392 m/s, 519 m/s and 577 m/s for the gas pressures of 0.2 MPa, 0.4 MPa and 0.6 MPa, respectively. This is because when the gas pressure is increased, the stagnation pressure (P_o) increases but the static pressure (P_s) at the nozzle exit remains the same as atmospheric pressure. This results in a higher gas velocity according to the following equation.

$$\frac{P_o}{P_s} = \left(1 + \frac{\gamma - 1}{2}M^2\right)^{\gamma/(\gamma - 1)},\tag{3.7}$$

where, γ is the specific heat ratio of the carrier gas and M is the Mach number. Also, turbulent kinetic energy increases as gas velocity increases at higher pressures. The gas velocity decreases with distance from the exit due to the free expansion of air into the atmospheric conditions. It is also observed that the

carrier gas flow is confined to a conical region about the nozzle axis close to the exit.

In order to analyze the flow of carrier gas for different pressures in the regions close to the nozzle exit, enlarged images of the velocity vector field near the nozzle are shown in Fig. 3.10. The regions with high gas velocity (greater than 300 m/s) extends farther from the nozzle exit with increasing carrier gas pressures. The flow field of the carrier gas in these regions at such high pressures necessitates a compressible flow model and justifies the implementation of compressibility effects in the dielectric spray model. It is also observed that the velocity changes sharply from the wall of the gas nozzle up to a small distance and then remains almost the same up to the center of the nozzle due to the small boundary layer. The entrainment of the surrounding air into the carrier gas jet is clearly visible from the direction of the velocity vectors shown in Fig. 3.11.

The contours of velocity on the XY plane passing through the middle of the nozzle unit are also shown in Fig. 3.12. These images show the increase in gas velocity from the inlet of the gas nozzle to its exit. The velocity of gas increases from the inlet as it passes through the gas nozzle and reaches the maximum value at the exit due to the choking condition. The velocity within the gas nozzle in the regions close to the nozzle wall is zero due to the no-slip boundary conditions. The blue areas in these plots are regions with low-speed gas flow and are observed at greater distances from the nozzle exit with an increase in carrier gas pressure.

The velocities of the carrier gas along the center-line of the nozzle for varying gas pressures obtained for both the experiments as well as predicted by the dielectric spray model are shown in Fig. 3.13. The velocity is higher at the regions closer to the nozzle exit and decays with an increasing distance. The high velocity at the exit (around 400 m/s for 0.4 MPa) shows that the gas flow is compressible. It is observed that the trend of gas velocities from the model and experiments is similar and the values are in good agreement, especially beyond a distance of 20 mm from exit, where the variation is less than 10%. A slight variation in the velocity of gas is observed in the regions close to nozzle exit. This is attributed
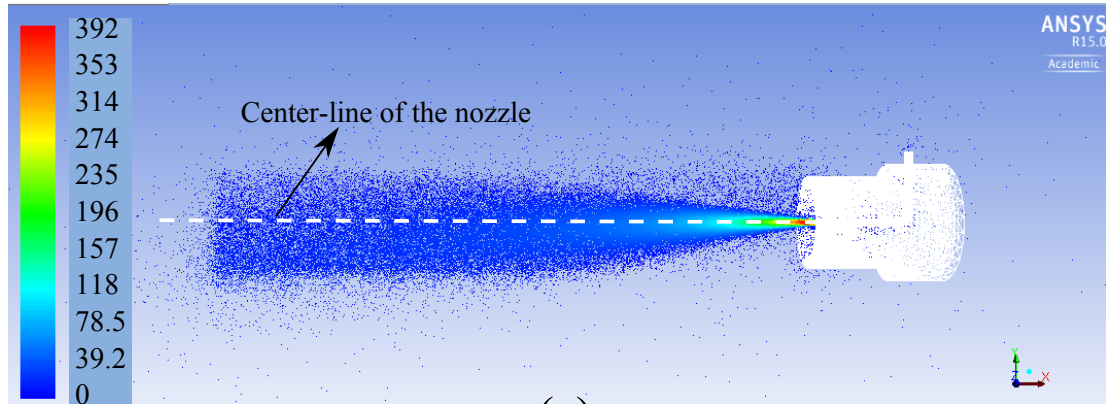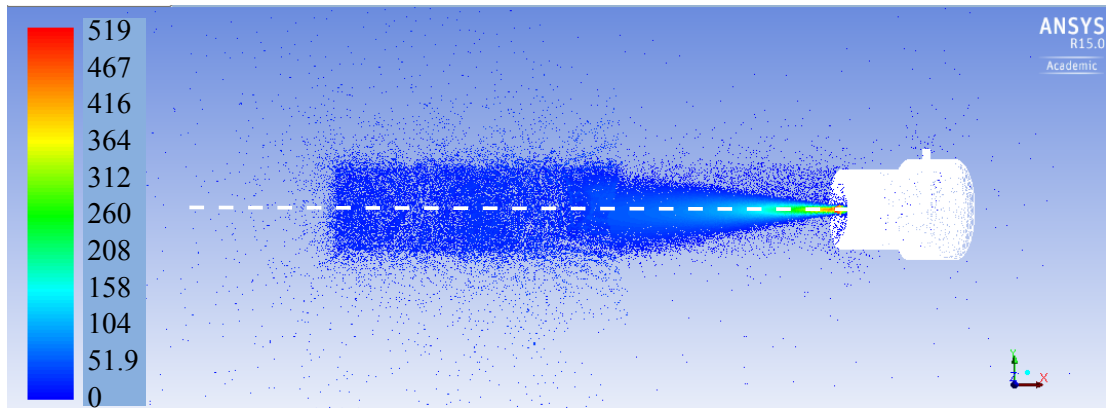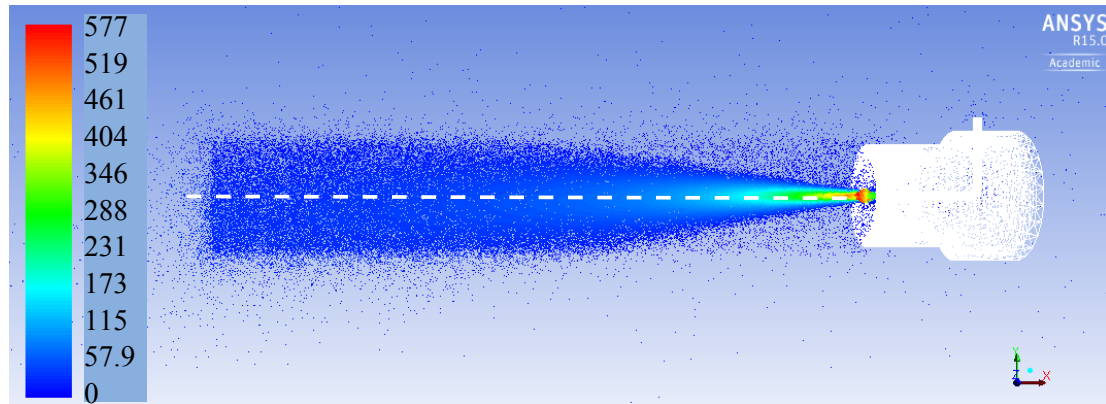
Figure 3.9: Comparison of velocity vectors of carrier gas for different pressures (a) 0.2 MPa, (b) 0.4 MPa and (c) 0.6 MPa
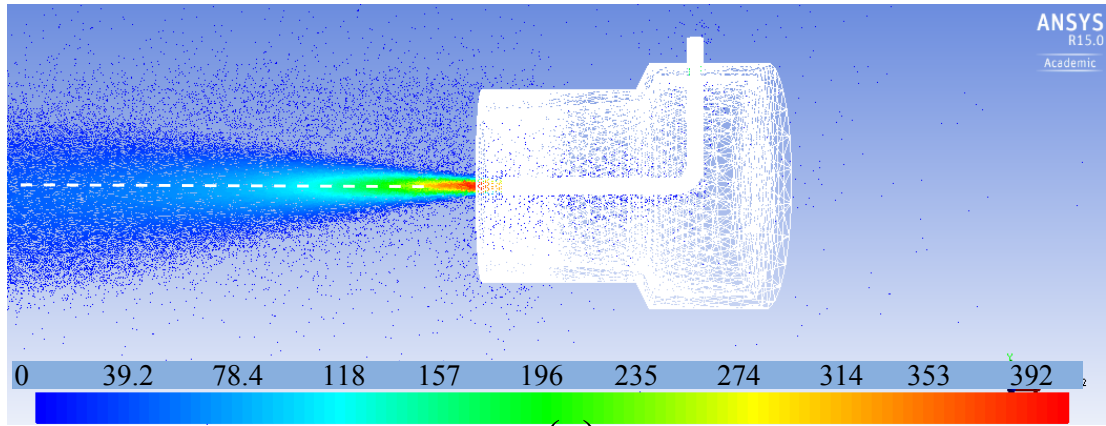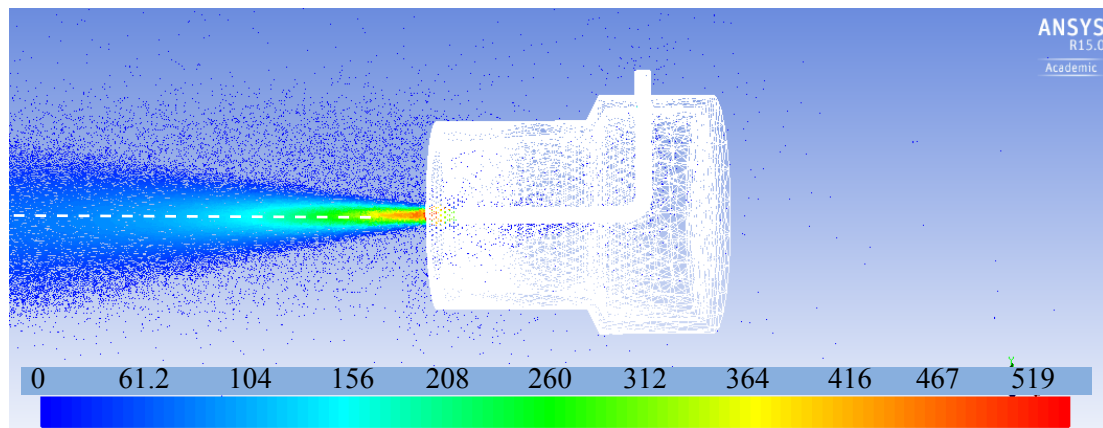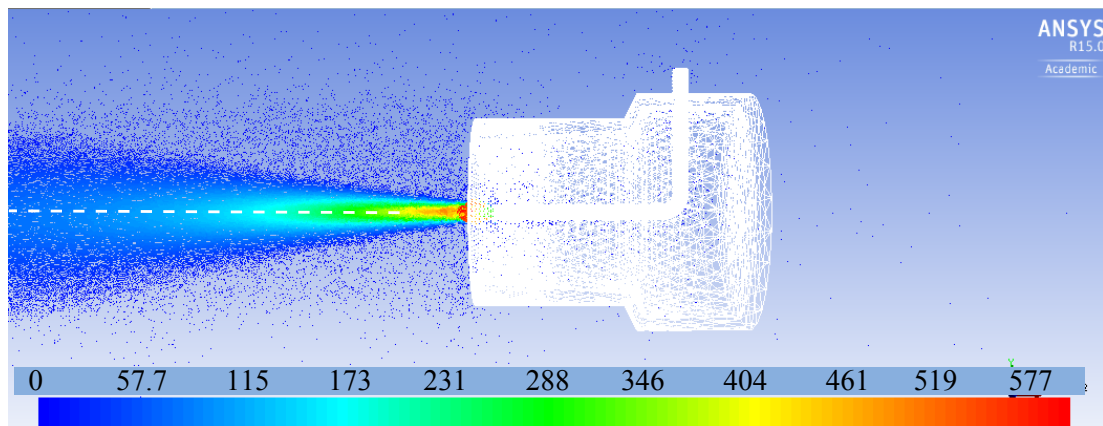
Figure 3.10: Comparison of velocity vectors of carrier gas close to nozzle exit for different pressures (a) 0.2 MPa, (b) 0.4 MPa and (c) 0.6 MPa
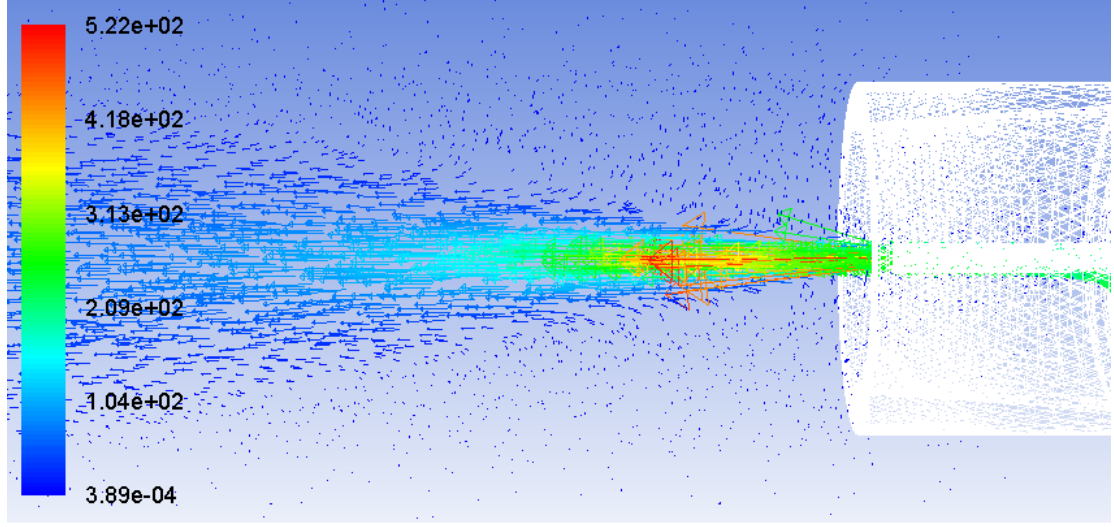
Figure 3.11: Velocity vectors of carrier gas close to nozzle exit for a gas pressure of 0.4 MPa.

to the fact that the experimental values of velocity are calculated from dynamic pressure measurements by assuming constant density for the gas.

3.3.3 Determination of Range of Impingement Angles for Spreading Regime

In order to ensure the formation of dielectric film on the machining surface, the range of spray parameters including distance from nozzle exit (L_s) and impingement angle (α) for different carrier gas pressures (P) should be determined. The droplet-surface interaction is characterized by We and K_y, which are defined as,

$$We = \frac{\rho_d v_{dn}^2 d_d}{\sigma_d} \text{ and } K_y = v_{dn}\left(\frac{\rho_d}{\sigma_d}\right)^{1/4}\left(\frac{\rho_d}{\mu_d}\right)^{1/8} f^{-3/8}, \qquad (3.8)$$

where, f is the droplet impingement frequency and K_y governs the boundary between spreading and splashing regimes for a train of droplets impinging on a surface with thin liquid film such as encountered in Spray-EDM. For the droplet-surface interaction to be within spreading regime, We must be greater than 10 and K_y should be lesser than 17 [113]. From Eqn. 3.8, it is seen that the non-dimensional numbers are influenced by the normal component of droplet veloc-
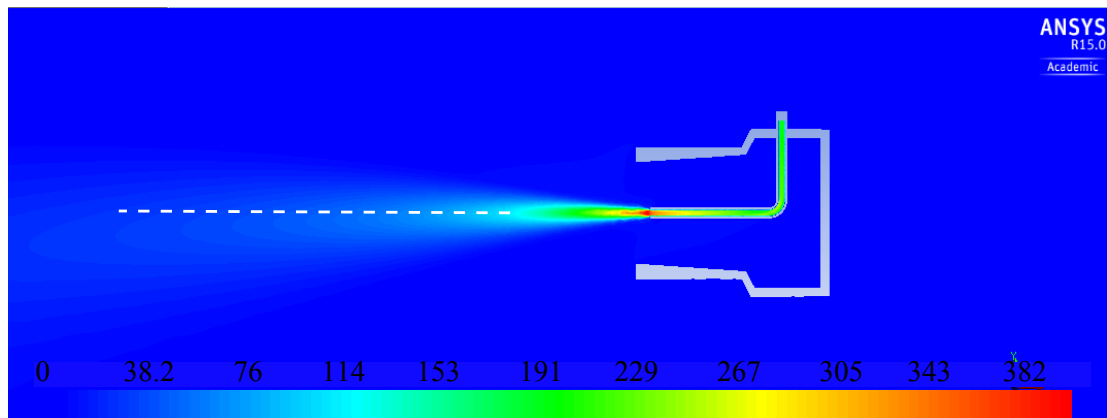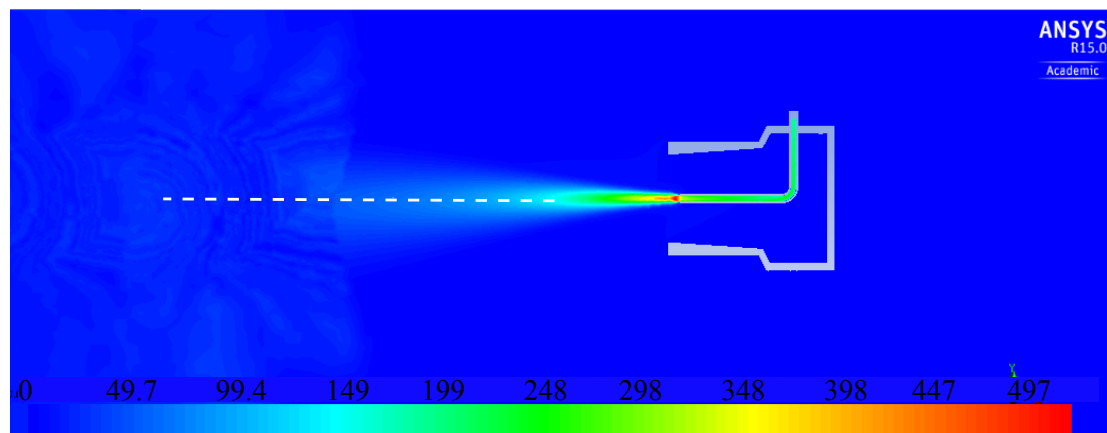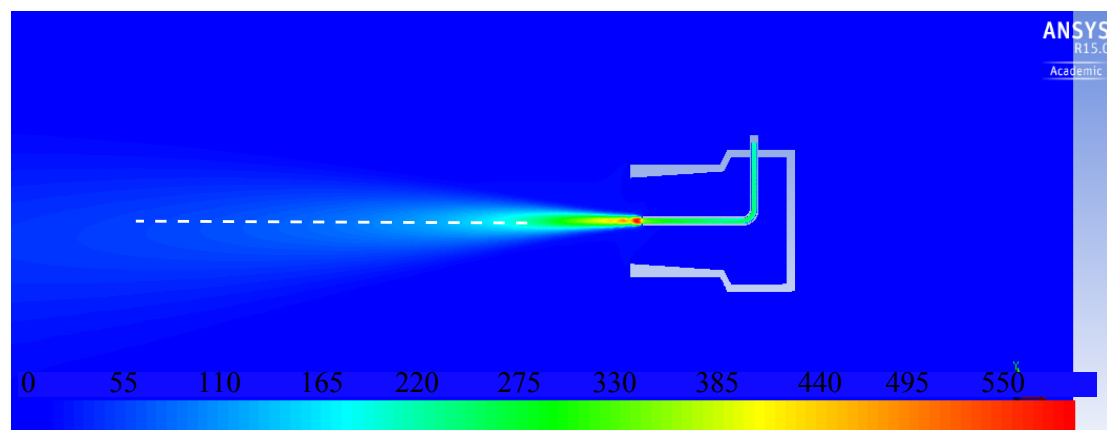
Figure 3.12: Comparison of velocity contours of carrier gas close to nozzle exit for different pressures (a) 0.2 MPa, (b) 0.4 MPa and (c) 0.6 MPa
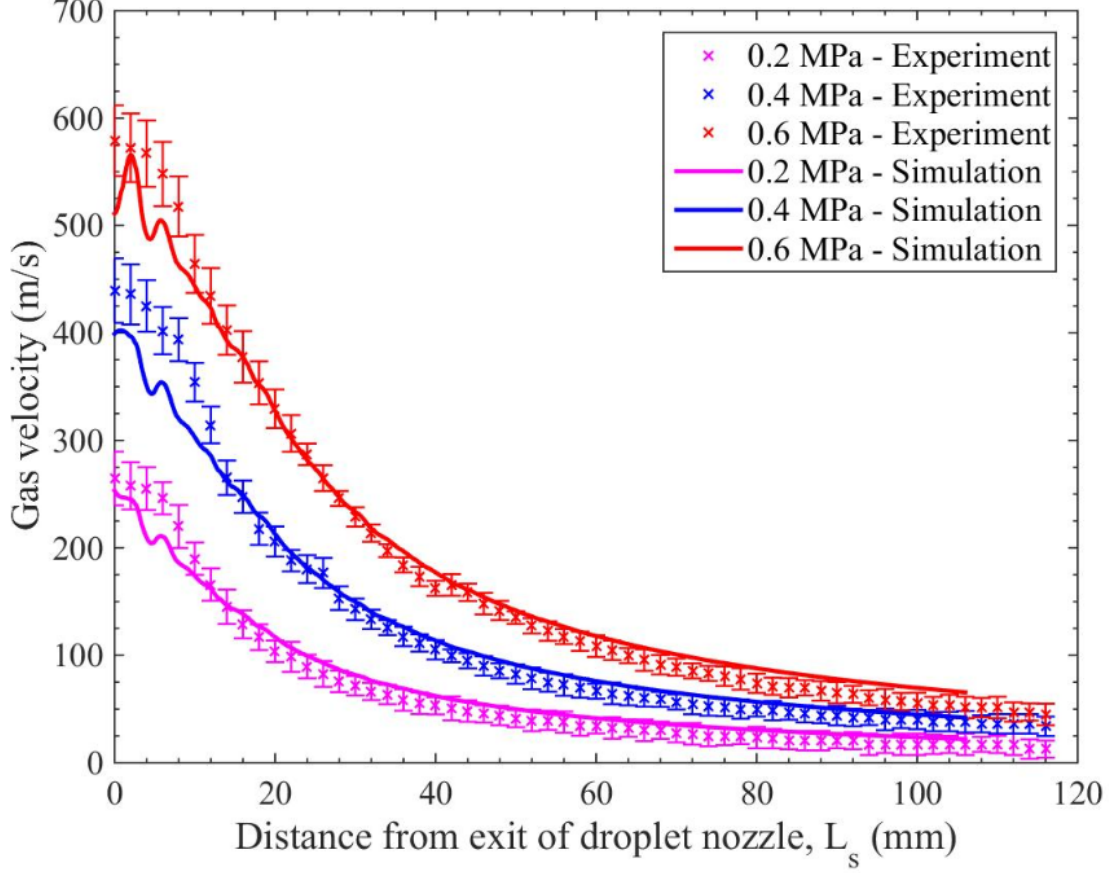
Figure 3.13: Comparison of center-line carrier gas velocity for different pressures

ity (v_{dn}) and fluid properties. The droplet normal velocity, v_{dn}, velocity of the droplets along the axis of the nozzle, v_d and the impingement angle, α are related as, $v_{dn}=v_d \sin(\alpha)$. Hence, the variation in v_d with distance from the nozzle exit has to be determined first. The range of α can then be determined using v_d, fluid properties and the limiting values of We and K_y.

The dielectric spray generated by the spray system for different pressures of carrier gas are shown in Fig. 3.14. It is observed that for all the cases, the spray focuses due to the entrainment of the surrounding air into the jet of carrier gas. The droplets are then observed to diverge downstream with a reduction in the droplet velocities. The droplets in the downstream region have lower velocities and lower flushing capability to remove the debris particles. Hence, the distance of the nozzle unit from the machining surface is critical for improving flushing

using Spray-EDM technique.

In order to study the focusing of dielectric droplets due to the carrier gas, enlarged images of the dielectric spray near the nozzle exit are shown for different gas pressures in Fig. 3.15. The droplets have a higher velocity close to the exit of the nozzle for higher carrier gas pressures. Also, the gas pressure influences the diameter of the spray at the focal point (point where the spray has the smallest diameter) and the position of the focal point. It is observed that for higher gas pressures, the focal point is closer to the nozzle exit. This is attributed to the decreased time period for droplets to be drawn into the carrier gas jet. It is observed that flux of droplets for smaller gas pressure (0.2 MPa) is lower compared to the other two cases, especially in the farther regions from nozzle exit. This is due to the poor ability of the gas jet to entrain the dielectric droplets, thereby retarding the formation of a focused spray of dielectric droplets.

The average velocity of droplets at a specific distance from the exit of droplet nozzle for different gas pressures is calculated using the velocities of all the droplets located at that particular distance and are shown in Fig. 3.16. The droplets closer to the nozzle exit have a lower velocity even though the gas velocity is higher in those regions. This is because the droplets are gradually accelerated from their initial velocity of around 3 m/s and reach their peak values after traveling a short distance in the gas phase. The maximum average velocity of droplets is observed at a distance of about 30-35 mm from the exit for all the gas pressures considered. Beyond this distance, the gas velocity decreases due to the free expansion of the carrier gas into the ambient. The dielectric droplets are then decelerated by the slower moving gas and reach a fairly constant velocity after about 200 mm. Note that the velocity of droplets is always lower than the carrier gas velocity at a given distance from the nozzle. The average droplet velocity from the dielectric spray model is fitted with an exponentially-modified Gaussian distribution [114] in order to obtain a function for the variation of droplet velocity, v_d with the distance from the nozzle exit, L_s.

Since the fluid properties and the droplet velocities along the axis of the noz-

89
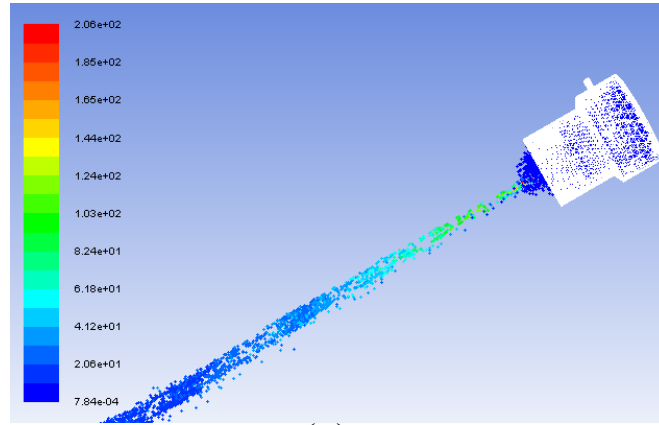
(a)
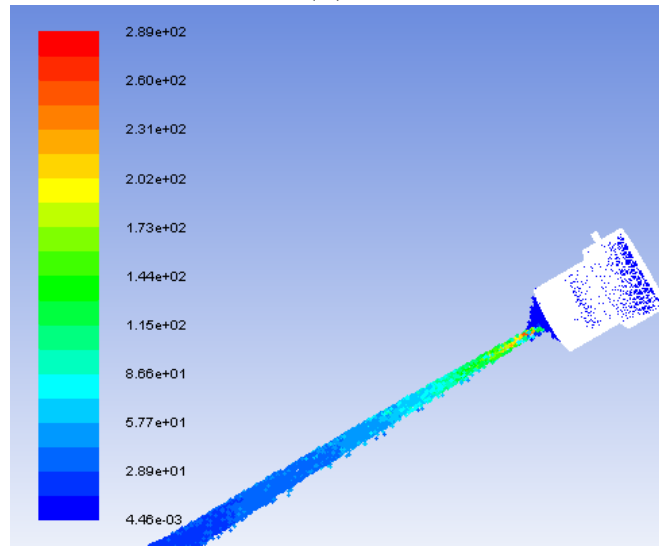
(b)
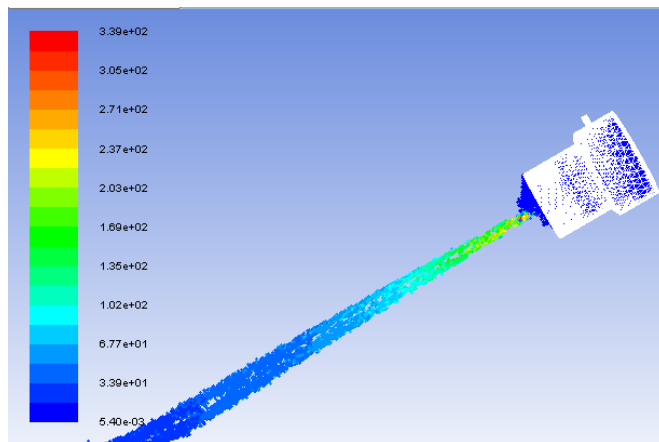
(c)

Figure 3.14: Velocity of dielectric droplets for different carrier gas pressures (a) 0.2 MPa, (b) 0.4 MPa and (c) 0.6 MPa
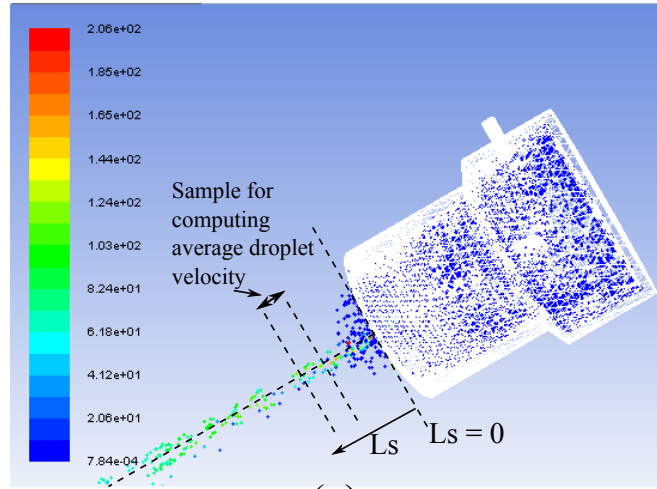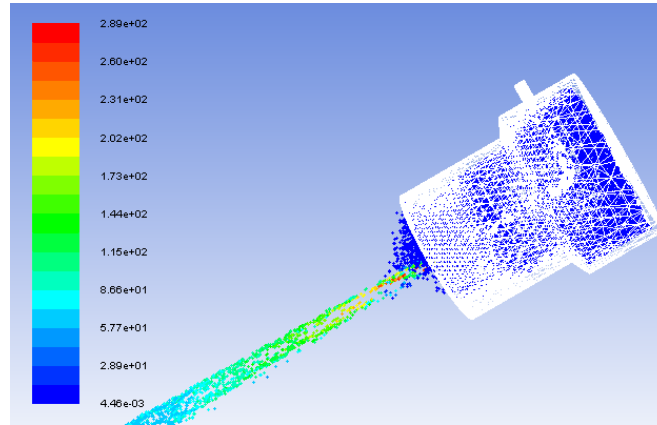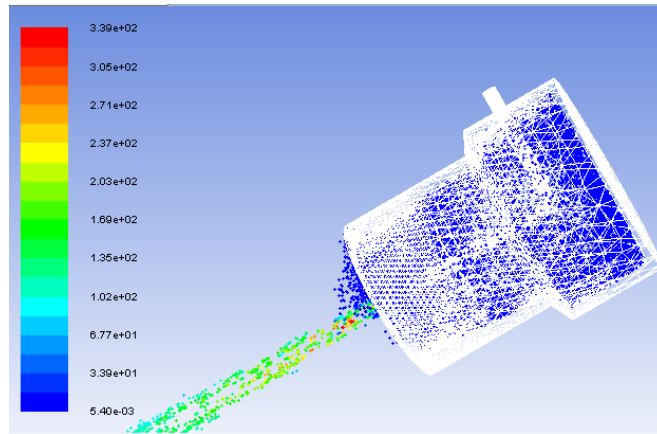
Figure 3.15: Velocity of dielectric droplets close to nozzle exit for different carrier gas pressures (a) 0.2 MPa, (b) 0.4 MPa and (c) 0.6 MPa
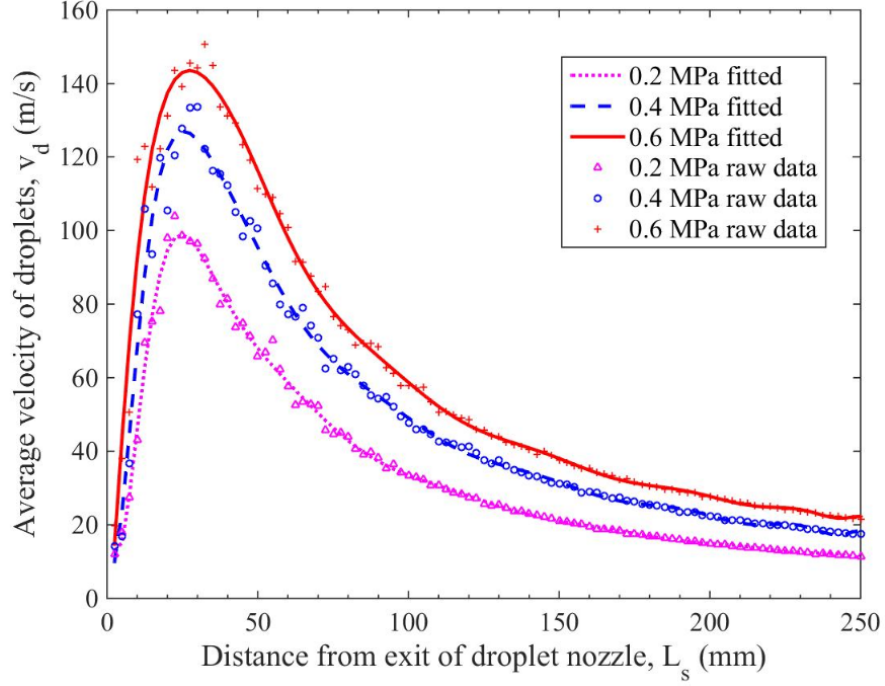
Figure 3.16: Droplet velocity variation for different gas pressures

zle (v_d) are known, the conditions for spreading regime, viz., $We > 10$ and $K_y < 17$ are used to determine two values of α. The smaller value is designated as α_{min} and the other as α_{max}. The range of impingement angles between α_{min} and α_{max} for a specific distance from the exit of droplet nozzle ensures that the droplets spread on impact with the surface. The α values calculated for different gas pressures, P are shown in Fig. 3.17. For example, when gas pressure, $P=$ 0.2 MPa and L_s=225 mm, any value of α between 12 ° and 90 ° will ensure that the droplet-surface interaction is within the spreading regime.

Lower gas pressures have a greater range of impingement angles due to lower droplet velocities associated with those cases. For example, with a gas pressure of 0.2 MPa, the droplet velocity beyond a distance of 190 mm from nozzle exit is sufficiently low such that even with an α of 90° (droplet impacts normal to the surface), the droplet-surface interaction is in spreading regime and a film is formed on the machining surface. However, for higher gas pressures, lower impingement angles with respect to the surface are required to obtain smaller droplet normal
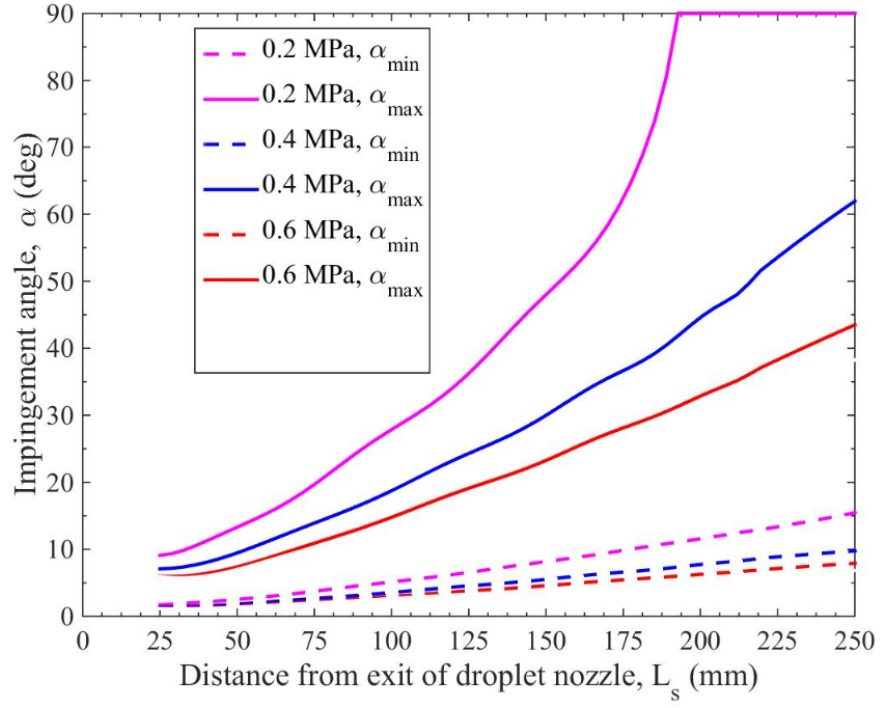
Figure 3.17: Range of α to achieve spreading on target surface for different gas pressures.

velocity, v_{dn} and ensure that spreading occurs.

3.4 Dielectric Film Formation Model

The film formation model is developed to characterize the thin fluid film in terms of thickness, h_f and velocity, v_f for a set of spray parameters. Earlier work on modeling thin film formation by Boughner *et. al.* (2011) [115] included prediction of the film thickness on a rotating cylindrical surface using an Atomized-Cutting Fluid (ACF) spray system. However, several assumptions were made that included: (i) the droplet velocity to be equal to the gas velocity, (ii) the droplets impinge on a dry surface during machining and (iii) incompressible flow of the carrier gas. While the second assumption is true for the initial stage of film formation, the subsequent droplets impact a layer of thin fluid film formed on the surface and not a dry surface. Since the spatial variation in film formed on the surface is significant in Spray-EDM, uniform film thickness throughout the surface cannot be assumed.

In this work, a three-dimensional, turbulent flow film formation model is developed. It is based on the Eulerian Wall Film (EWF) approach using Ansys Fluent$^{\text{TM}}$. A 3D model is developed considering the significant spatial variation in film thickness and velocity along the target surface, especially for impingement angles other than 90°.

3.4.1 Model Description

Eulerian Wall Film (EWF) model

The EWF model is based on the thin-film assumption theory that is applicable for films with micron-level thickness and comparably large lateral dimensions. In Spray-EDM process, the film thickness is usually a few microns and hence the EWF approach is used to predict the generation and flow of liquid films as droplets impinge the target surface [111]. The mass conservation equation for the

thin film is given as,

$$\frac{\partial h_f}{\partial t} + \nabla_s.[h_f \ \vec{V_f}] = \frac{\dot{m}_s}{\rho_d},$$ (3.9)

where, h_f, ρ_d, ∇_s, $\vec{V_f}$, and $\dot{m}_s$ are the film height, dielectric droplet density, surface gradient operator, mean film velocity and mass source per unit wall area, respectively. The momentum conservation for the film is given as,

$$\frac{\partial(h_f\vec{V_f})}{\partial t} + \nabla_s.[h_f \ \vec{V_f} \ \vec{V_f}] = -\frac{h_f \ \nabla_s \ P_L}{\rho_d} + \frac{3 \ \vec{\tau}_{fs}}{2 \ \rho_d} + (\vec{g}_\tau)h_f$$
$$- \frac{3 \ \vec{V_f} \ \nu_d}{h_f} + \frac{\dot{q}_s}{\rho_d},$$ (3.10)

where, $P_L = P - \rho h_f(\vec{n}.\vec{g})$ includes the effect of gas flow pressure and gravity component normal to the wall surface. In Eqn. 3.10, the second and third terms account for the viscous shear force at the gas-film interface and effect of gravity in the direction parallel to film flow, respectively. The fourth term is associated with viscous force only in the film and the last term includes the droplet collection and separation phenomenon [111]. The mass and momentum transfer from the DPM model to the EWF model occurs through the source terms, $\dot{m}_s$ and $\dot{\vec{q}}_s$ present in Eqn. 3.9 and Eqn. 3.10 and are defined as,

$$\dot{m}_s = \dot{m}_d \ \text{and}$$ (3.11)

$$\dot{\vec{q}}_s = \dot{m}_d.(\vec{V_d} - \vec{V_f}),$$ (3.12)

where, $\dot{m}_d$ is flow rate of the droplet stream impinging on the wall and $\vec{V_d}$, $\vec{V_f}$ are the velocities of the droplet stream and liquid film, respectively. A first-order explicit scheme is used for both spatial and temporal discretization of film parameters. The time-step, δt for solving Eqn. 3.9 and Eqn. 3.10 is set to 0.25 ms since lower time-steps are not found to have a significant effect on the film deposition process.

Boundary and initial conditions for film modeling

The computational domain and boundary conditions for film modeling is similar to that in Fig. 3.7. The target surface is given a trap boundary condition for absorbing the dielectric droplets. The initial conditions for the film thickness, h_f and velocity components, v_f on the target surface are set to zero since no film is formed prior to droplet impingement and the steady state film characteristics are evaluated after a certain number of film time-steps.

3.4.2 Validation of Film Formation Model

In order to understand the nature of film formation on the machining surface using the Spray-EDM system, an experimental testbed as shown in Fig. 3.18 is built. The film thickness is measured using an optical microscope (Model AD5040HS X3, HIROX-USA, Inc.) with 20× to 800× magnification is used along with a camera (Infinity 3, Lumenera Corporation, Canada). Precise control of the distance between the camera and the front surface of the flat target plate is crucial for proper focusing and image capture and is achieved by traversing the mounting stages on which the plate is fixed. The set up is placed on a Thor Labs$^{\text{TM}}$ optical table to ensure rigidity throughout the film imaging process. Note that the field of view of the camera at a magnification of 175× is restricted to 1 mm. In order to get images of film along the direction of the spray from the point of impingement, the optical setup is traversed by 1 mm using the positioning stages. Gas pressure, P of 0.2 MPa, dielectric flow rate of 10 ml/min, impingement angle, α of 30° and distance from nozzle exit to the target surface measured along nozzle axis, L_s of 225 mm are used. This combination of spray parameters ensures that the droplet-surface interaction is in the spreading regime and a thin dielectric film is formed on the target surface (Fig. 3.17). A sample image of the film in the stable region (between -160 mm and -161 mm from the impingement point) obtained experimentally is shown in Fig. 3.19.

The three-dimensional profile of the film for the same set of spray parameters
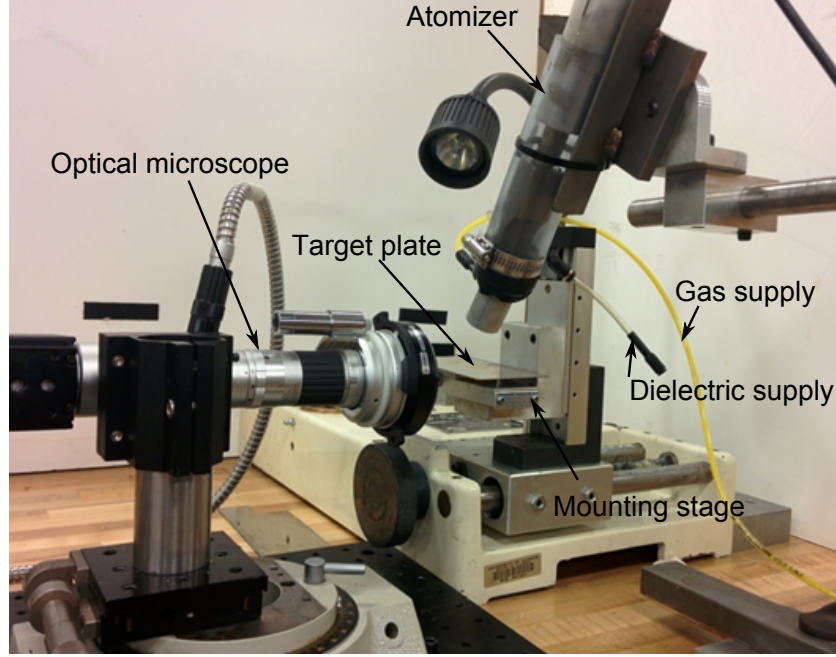
Figure 3.18: Optical setup used for capturing images of dielectric film.
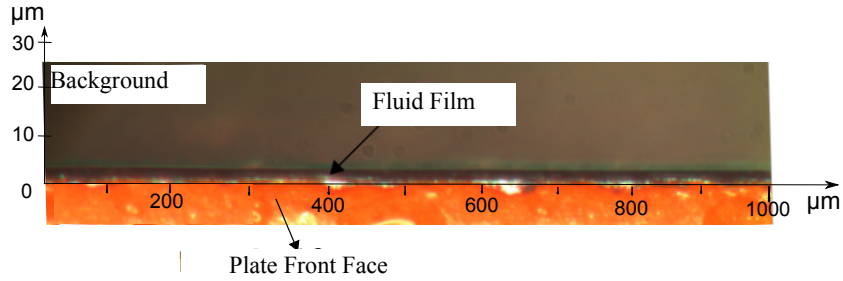
Figure 3.19: Sample image of film between -160 mm and -161 mm from the point of impingement

as predicted by the film formation model is shown in Fig. 3.20. The point X $= 0$ and Z $= 0$ corresponds to the spray impingement point (Point 6 in Fig. 3.4), which is the intersection of the center-line of the dielectric spray and the target surface. The pressure exerted by the gas on the film causes the depression at the impingement point and protrusion in the regions close to the point. Beyond this region, the film thickness is found to decrease gradually with distance along the X-direction from the impingement point.

The film thickness is compared with experimental data obtained for different combinations of carrier gas pressures, P (0.2 MPa and 0.4 MPa) and vertical
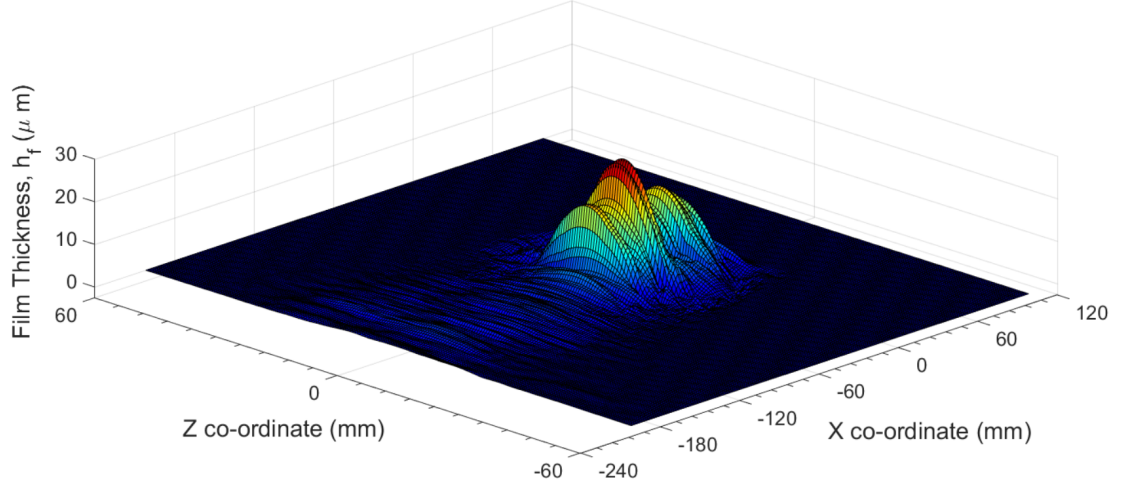
Figure 3.20: 3D plot of the film formed on the machining surface

distances between nozzle and machining surface, d (109.5 mm and 134.5 mm) and is shown in Fig. 3.21. Note that the vertical distance is obtained from Fig. 3.4 as $d=(L_s+N_l)\cdot sin\ \alpha$, where N_l=44 mm, L_s=160 mm and α=32.5° for d=109.5 mm and L_s=225 mm and α=30° for d=134.5 mm. The film thickness, h_f is plotted along its center-line on the machining surface (Z=0 in Fig. 3.20). The range of X-axis for distance along surface in Fig. 3.21 is restricted to -160 mm to -220 mm since large fluctuations in thickness are observed in the region close to the impingement point (0 to -160 mm). Also, the regions with uniform film thickness are favorable for Spray-EDM process and hence validating the film formation model in that region (-160 to -220 mm) is acceptable. The experiment is repeated 3 times for each combination of P and d and the mean and standard deviation ($\mu\pm\sigma$) are plotted. The variation in experimental film thickness for trials with the same combination of P and d is due to the transient nature of the film. Film thickness is influenced to a greater extent by d than P. A thinner film is observed for large values of d (134.5 mm) due to the reduced flux of droplets impacting the surface. Smaller values of d increase the fluctuations in film thickness due to higher gas pressures close to nozzle exit and this is evident from the deviation in the trend of thickness beyond 190 mm for the condition with P=0.4 MPa and d=109.5 mm. The model predictions show a good agreement with experimental measurements

for the range of distance considered. The difference between the model predictions and experiments is attributed to the effect of actual topography and surface energy of the machining surface on wetting/film formation phenomenon.
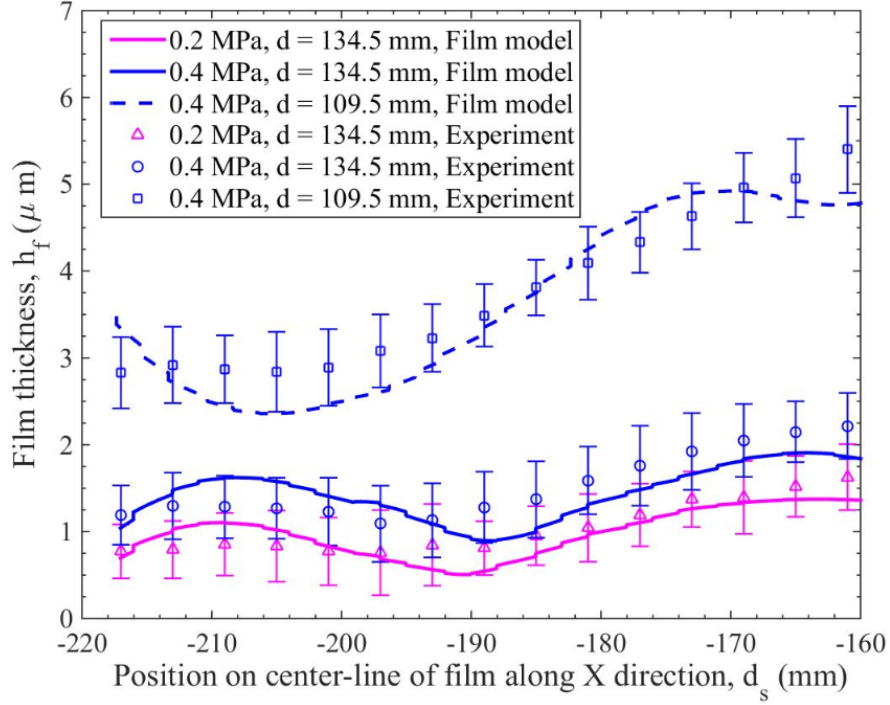
Figure 3.21: Comparison of experimental and simulated values of film thickness

3.4.3 Determination of Film Thickness and Velocity

The validated film model is used to determine the film thickness, h_f and film velocity, v_f for different combination of spray parameters. The parameters varied in this model are carrier gas pressure, P and distance, d shown in Fig. 3.4. Three levels for the factors, P and d are used in the parametric study (Table 3.2). The combinations marked with * do not result in spreading regime.

The contours of film thickness on the machining surface for the six cases (shown in Table 3.2) that result in film formation are shown in Fig. 3.22. A significant spatial variation in film thickness on the surface is observed, thereby justifying the development of a three-dimensional film formation model. For all the cases,

Table 3.2: Simulation cases studied with the film model.

Trial No.	L_s (mm)	α (°)	d (mm)	P (MPa)
1	125	30	84.5 (-1)	0.2(-1)
2*	125	30	84.5 (-1)	0.4(0)
3*	125	30	84.5 (-1)	0.6(+1)
4	160	32.5	109.5 (0)	0.2(-1)
5	160	32.5	109.5 (0)	0.4(0)
6*	160	32.5	109.5 (0)	0.6(+1)
7	225	30	134.5 (+1)	0.2(-1)
8	225	30	134.5 (+1)	0.4(0)
9	225	30	134.5 (+1)	0.6(+1)

a region of lower film thickness (blue areas) is observed near the point where the spray impinges the machining surface. Surrounding this area is a region where higher film thickness is observed due to the normal component of the carrier gas pressure. The film thickness then decreases gradually and eventually becomes zero in the regions farther from the impingement point. It is pertinent to note that for smaller values of d (Fig. 3.22 (f)), the proximity of the machining surface to the droplets not entrained within the core of the dielectric spray results in the formation of patches of film in certain regions. The film thickness is observed to be higher for lower values of d due to the higher flux of droplets impacting the machining surface.

The film thickness variation along the center-line of machining surface for the various combinations of P and d is shown in Fig. 3.23. The regions near the impingement point are seen to be unsuitable for Spray-EDM due to large fluctuations in the film characteristics. The thickness is observed to be uniform with smaller values at regions farther from the impingement point (beyond 100 mm from the impingement point for all cases except for Trial 1, P=0.2 MPa and d=84.5 mm). h_f varies to a greater extent with d than P. A smaller film thickness (about than1 μm) is observed on the surface for large distances (d=134.5 mm) from the nozzle exit. This is attributed to a drastic reduction in the flux of droplets impinging on the machining surface.

Smaller values of d result in higher film thickness and are preferred for Spray-
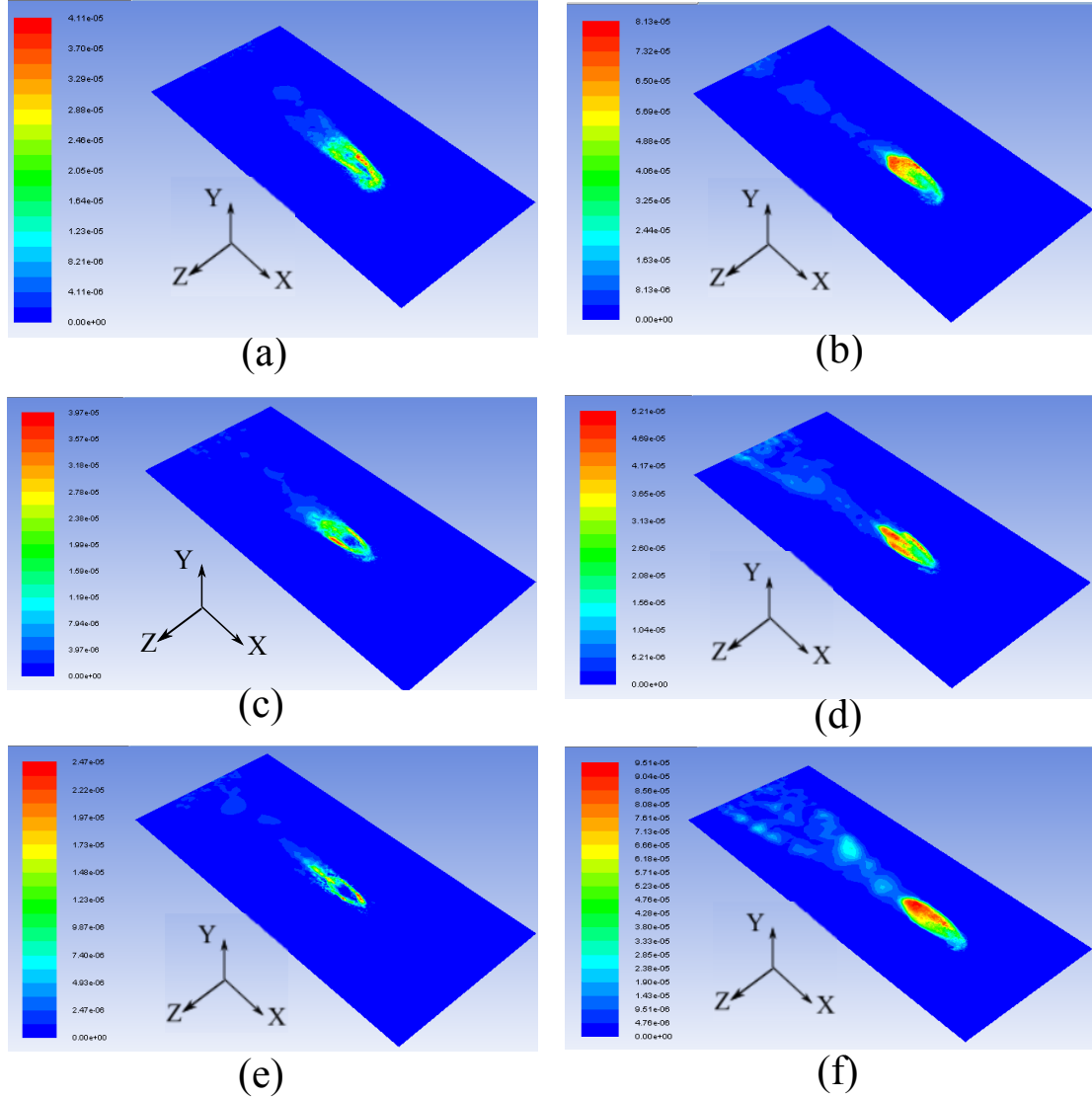
Figure 3.22: Contours of film thickness for (a) P=0.2 MPa and d=134.5 mm, (b) P=0.2 MPa and d=109.5 mm, (c) P=0.4 MPa and d=134.5 mm, (d) P=0.4 MPa and d=109.5 mm, (e) P=0.6 MPa and d=134.5 mm, (f) P=0.2 MPa and d=84.5 mm.

EDM since it is critical to ensure that the inter-electrode gap is always completely filled with dielectric fluid. However, decreasing d beyond a certain limit for a given pressure, P and impingement angle, α will result in droplets with much higher normal component velocity to impact the machining surface and the droplet-surface interaction would not be within the spreading regime.
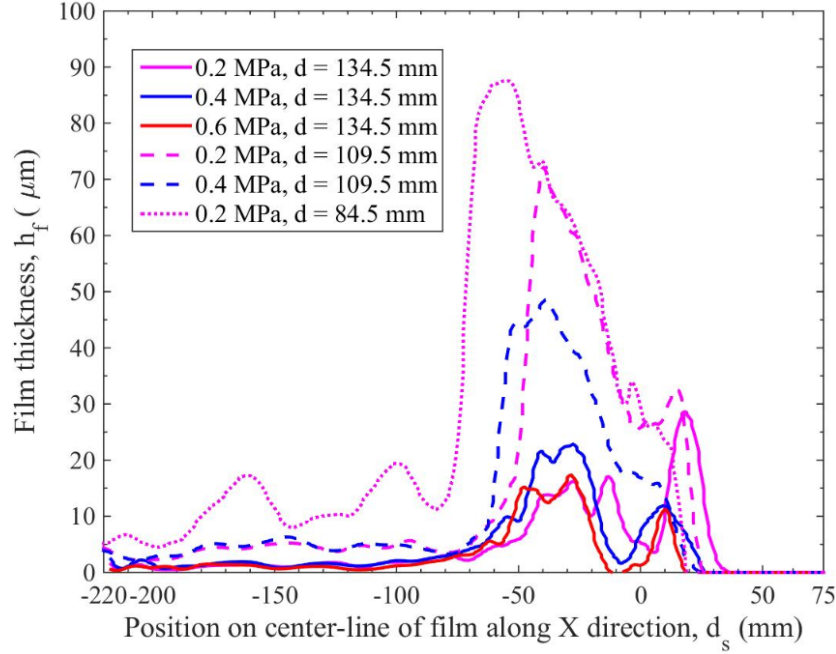
Figure 3.23: Comparison of film thickness for different combinations of spray parameters.

Figure 3.24 shows the variation in film velocity, v_f along the center-line of machining surface for different combinations of P and d. Though the film thickness (h_f) is not significantly influenced by P for a given d, the film velocity (v_f) is affected by variation in gas pressure as is evident from Fig. 3.24. Higher gas pressures increase v_f due to a greater component of gas velocity in the direction of film flow. A similar trend is observed for all the values of d considered. Among the combinations of spray parameters that ensure inter-electrode gap (say 1 μm) is completely filled with dielectric, the combinations of 0.2 MPa, 84.5 mm and 0.4 MPa, 109.5 mm are preferred to 0.2 MPa, 109.5 mm since higher film velocity in first two cases will flush the debris from the gap more effectively compared to the third case.
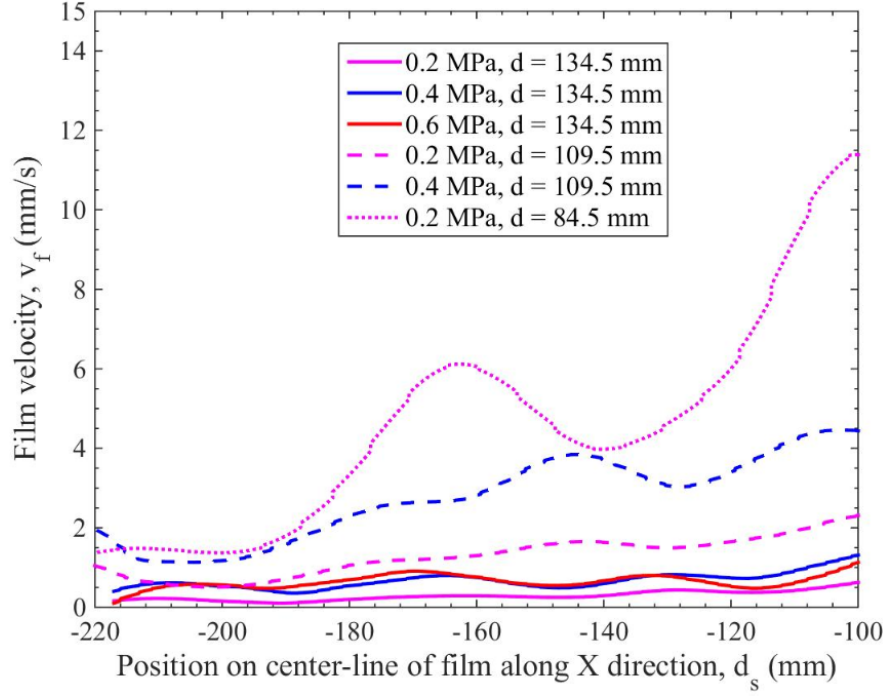
Figure 3.24: Comparison of film velocity for different combinations of spray parameters.

3.5 Debris Flushing Model

Debris flushing in EDM has a significant effect on the performance of the process. A higher material removal is achieved with an effective flushing method because of reduction in frequency of abnormal discharges that occur when debris are present in the inter-electrode gap. Flushing also impacts the tool wear, crack density and recast layer thickness on the machined surface which can be minimized by an optimal flushing method [59].

Debris flushing in EDM has been experimentally investigated by Wang *et. al.* [78] and Cetin *et. al.* [116]. In these studies, the motion of debris particles was studied using Particle Image Velocimetry (PIV) technique with a set up made of transparent materials. However, the precise real-time observation of the generation and movement of EDM debris through experiments is difficult. So, analytical and computational modeling have been explored [10, 20, 116, 22, 23]. However, these models did not account for the impact force associated with the plasma

103

discharge, which is one of the critical factors affecting the dielectric flow and trajectory of debris particles. Also, the debris particles were assumed to have uniform diameter, unlike the actual debris. Mastud *et. al.* [23] recently developed a 2-dimensional, axisymmetric model to study debris motion during the reverse micro-electrical discharge machining process. However, this model did not account for plasma explosion pressure. Further, these models could not be used to study the Spray-EDM process since a bulk liquid is assumed as the dielectric medium in these models and not a thin dielectric film (few μm) as in Spray-EDM. Also, these models do not include the actual topography of the machined surface to study the debris flushing in EDM.

A two-dimensional, transient, turbulent flow model is developed to predict the trajectories of the debris particles in the presence of a flowing dielectric film. A two-dimensional model is sufficient to model the effect of flowing film on debris flushing since the velocity of the film along the direction of d_s (Fig. 3.4) is much higher compared to the other directions. The motion of debris particles in the dielectric occurs due to the drag force exerted by the flowing dielectric liquid. A DPM approach similar to that used in dielectric spray model is used to track trajectories of EDM debris. The model also accounts for (i) plasma pressure due to discharge, (ii) actual crater geometry produced due to discharge and (iii) Rosin-Rammler size distribution of debris particles.

3.5.1   Modeling Approach

The model assumes that discharge occurs at time, $t = 0$, which results in the formation of a crater on the workpiece and several debris particles. Also, a thin dielectric film with thickness, h_f and velocity, v_f (obtained from the dielectric film model discussed in Sec. 3.4) is assumed to be formed on the machining surface. The discharge is followed by the flushing action of the dielectric film. A schematic of the fluid domain is shown in Fig. 3.25. This domain is considered to be within the stable region of the film between a distance of -180 mm and -200 mm from

the point of spray impingement. The fluid domain is bounded by the machining surface at the bottom with the tool electrode positioned in the middle and set at a distance equal to the inter-electrode gap. The flowing dielectric film enters the inter-electrode gap from the left-end with a velocity, v_f. The right-side of the domain is set at atmospheric pressure. The top side of the film is considered to be a free surface (finite slip for fluid velocity components) and a no-slip boundary condition is assumed at the work-surface and the tool surface for the flowing film. The force exerted by the flowing dielectric film on the tool electrode is determined to be negligible (order of μN) and hence, the deflection of tool is ignored [117]. The velocity of dielectric film within the inter-electrode gap, $\vec{v}'_f$ is determined by solving 2-D Navier-Stokes equations. $\vec{v}'_f$ is influenced by the film velocity at the inlet, v_f, the plasma pressure and plasma radius. The effect of plasma pressure for a given plasma radius on the dielectric film flow in the inter-electrode gap is incorporated as an initial condition in the inter-electrode region using an user-defined function.
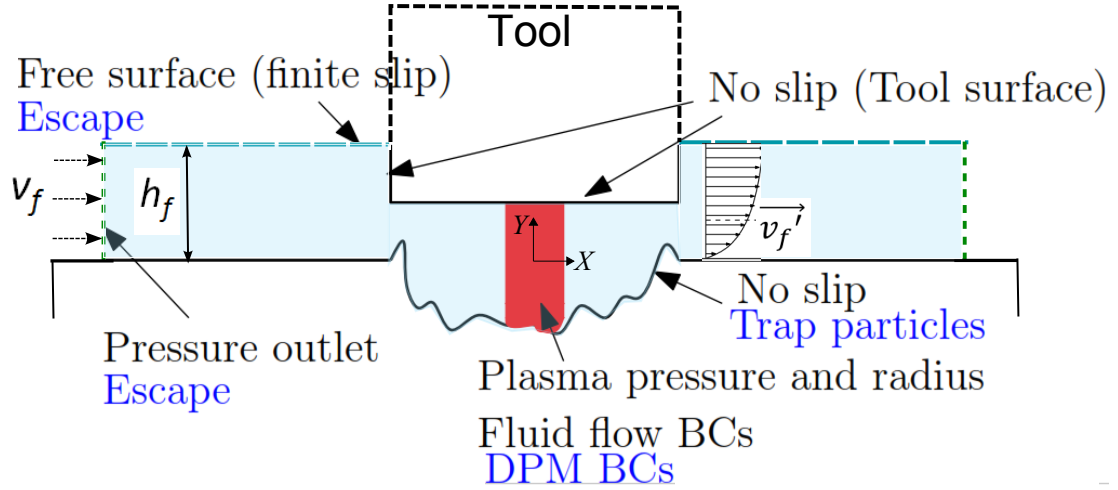
Figure 3.25: Schematic of domain and boundary conditions for debris flushing model

The flow-field of dielectric film in the inter-electrode gap is solved for the initial conditions of plasma pressure along with the injection of debris particles using CFD approach. The debris particles are injected normal to the surface with an

initial velocity and the trajectory is determined using the force-balance equation of each debris particle, given as follows.

$$\frac{d\vec{v}_{debris}}{dt} = F'_D(\vec{v'}_f - \vec{v}_{debris}) + \frac{\vec{g}(\rho_d - \rho_{debris})}{\rho_{debris}}, \qquad (3.13)$$

where, $\vec{v}_{debris}$ is the debris particle velocity, F'_D is the drag force exerted by the dielectric film on the debris, $\vec{v'}_f$ is the velocity of the dielectric film in the inter-electrode gap, ρ_d and ρ_{debris} are the density of dielectric fluid and debris particle, respectively. The drag force between the debris and the dielectric fluid film is calculated using Eqn. 3.2, where μ, ρ_d, d_d and Re are replaced by dynamic viscosity of dielectric, μ_d, density of debris, ρ_{debris}, diameter of debris particle, d_{debris} and the corresponding Reynolds number, Re', respectively. The debris particles are assumed to be spherical with particle sizes following Rosin-Rammler distribution with a mean diameter of d_{debris}, and the number of particles injected during the simulation is estimated by dividing the volume of crater by the average volume of a single debris particle.

A 'trap boundary condition' for the debris particles is considered at the machining surface to ensure that the debris particles striking the surface adhere to it. The distance at which the debris particles are trapped on the work surface from the crater center is determined by post-processing the particle trajectory results from the debris flushing model and the distribution of debris around the crater is determined.

3.5.2 Evaluation of Force Exerted by Dielectric Film on the Tool Electrode

In order to ensure the validity of the assumption that the tool electrode does not deflect due to the film motion, the force on the tool was evaluated for all the aforementioned cases of spray system parameters. The total force exerted by the dielectric fluid film on the tool is given by the sum of hydrodynamic force acting on the tool's cylindrical surface and the shear force acting on the bottom surface

of the tool. The two forces are represented in Fig. 3.26 and are calculated as,

$$F_T = F_H + F_S, \tag{3.14}$$

$$F_H = \frac{1}{2}\rho_d D \int_{h_1}^{h_f} v_f{}^2 dh \;\; \& \;\; F_S = \frac{\pi}{4}D^2\mu_d \left(\frac{dv_f}{dh}\right)_{h=h_1} \tag{3.15}$$

where, F_T, F_H and F_S are the total force, hydrodynamic force and shear force exerted on the tool electrode, h_1 corresponds to the bottom surface of tool, h_f corresponds to the top surface of the dielectric film and D is the diameter of the tool, respectively. The magnitude of forces calculated using Eq. 3.14 are shown in Fig. 3.27. A film with higher v_f exerts a greater force on the tool electrode. However, the magnitude of forces is found to be significantly small, which is in the range of 0.4–1.2 μN, suggesting that the deflection of tool due to flowing dielectric film is not a major issue in Spray-EDM for the parameters considered.
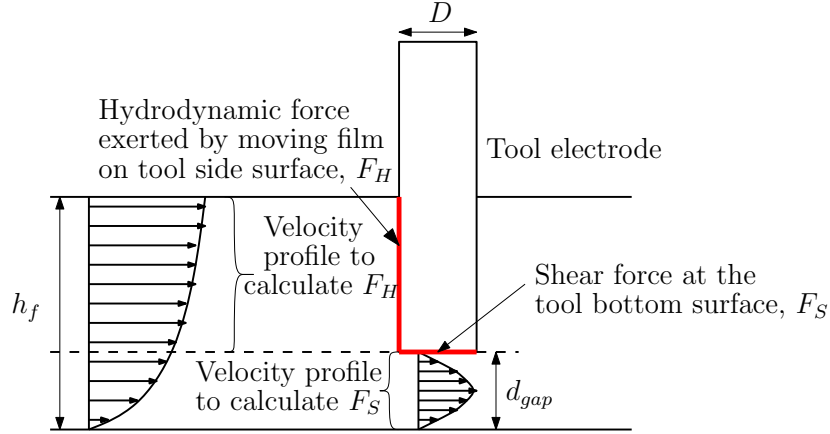
Figure 3.26: Schematic of methodology of force calculation
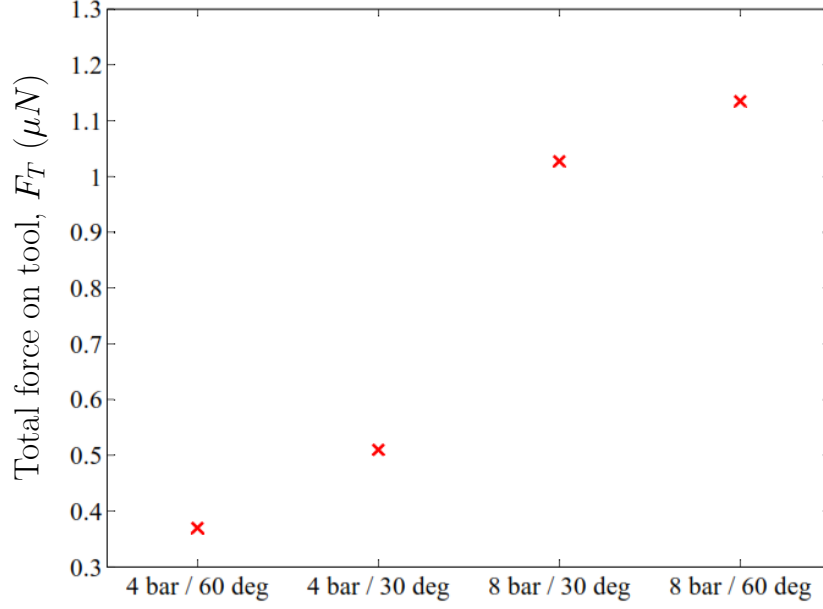
Figure 3.27: Force exerted on tool electrode for different P and α

3.6   Summary

The concept of Spray-EDM was discussed thoroughly along with the spray system components and working principle. A 3-D transient model to understand the atomization of dielectric droplets, dielectric spray formation and thin film formation was developed. In order to study the flushing of debris from the inter-electrode gap, a 2-D model based on the DPM approach was developed. Specific conclusions of the chapter are as follows.

1. The dielectric spray model is used to determine the spatial variation in droplet velocity for different carrier gas pressures. This is used along with the theory of droplet impingement dynamics to determine the range of impingement angles that ensures film formation on the machining surface, i.e. the droplet-surface interaction is within the spreading regime. Higher impingement angles could be used with smaller gas pressures or larger distances from droplet nozzle exit due to the smaller droplet velocities associated with these conditions.

2. The film formation model is developed to determine the thickness and veloc-

ity of the thin dielectric film formed on the machining surface for different combinations of spray parameters. It is observed that distance between the nozzle exit and the machining surface influences the thickness to a greater extent than the carrier gas pressure. Large distances result in smaller thickness due to a reduction in the flux of droplets impacting on the surface. Higher gas pressures result in higher film velocities for a given distance between nozzle and machining surface.

3. The debris flushing model is developed to predict the trajectory of the debris particles in the inter-electrode gap. This model takes into account critical process-related factors including the plasma pressure, plasma radius, non-uniform debris size and the actual topography of the crater.

Chapter 4

Debris Flushing Model Validation and Discussion

The objective of this part of the study is to perform EDM experiments to validate the debris flushing model and also to study the performance of the Spray-EDM process. The experimental set up for the EDM experiments is discussed first. This is followed by the validation of the debris flushing model developed in Chapter 3. The validated debris flushing model is used to determine the combination of spray parameters that result in enhanced flushing of debris from the inter-electrode gap. Finally, the Spray-EDM process is compared with Wet-EDM and Dry-EDM in terms of material removal, tool wear and flushing of debris particles from the inter-electrode gap.

4.1   Single-discharge EDM: Experimental Setup

Single-discharge EDM experiments are performed in order to isolate the fundamental mechanics of the EDM process and debris flushing from the stochastic nature of the multiple-discharge process [1]. The set up used for EDM experiments is shown in Fig. 4.1. The single-discharge EDM experiments are performed on a three-axis micro-scale Machine Tool (mMT) developed at the Micro-scale Machining and Machine Tool Research Laboratory at the University of Illinois at Urbana-Champaign. A 100 μm tungsten rod is used as cathode and the anode is a 1.5 x 1.5 x 0.25 mm Stainless Steel plate. During the discharges, the workpiece is placed in a small tank to prevent the leakage of dielectric. A piezo-actuated stage is used to set the gap distance between the two electrodes within a few hundreds of nano-meters accuracy. An Infinity camera is used for observing the discharge

process. The dielectric is either filled in the tank containing the workpiece for Wet-EDM experiments or supplied in the form of spray for the Spray-EDM experiments. For Spray-EDM, the flow rate of dielectric from a reservoir is precisely controlled using flow-control valves. Programming using G-codes is done to control the 3-axis mMT. The programs are used to perform a sequence of processes, viz., set the inter-electrode gap distance, apply the voltage across the electrodes for the discharge duration, retract the tool electrode away from workpiece and move the electrode to the next discharge location.
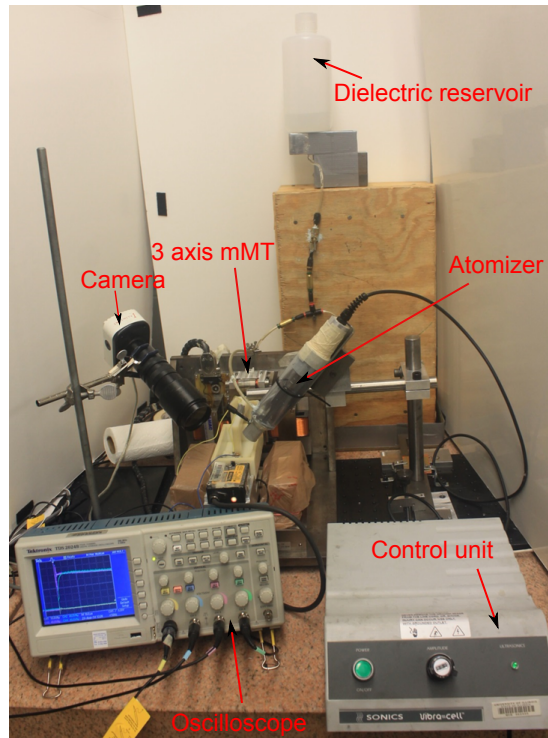
Figure 4.1: Experimental set up for Spray-EDM technique.

The current and voltage values across the gap during the discharge are collected using a 2 GigaSamples Tektronix TDS2024B oscilloscope. A sample plot of the VI characteristics obtained during the EDM discharges is shown in Fig. 4.2. The instantaneous power and the discharge energy are obtained from these data for each discharge. In order to determine the volume of material removed, a 3D topography of each crater is obtained as discussed by Heinz et. al. (2011) [19] using a Keyence LT-9010M surface scanning confocal laser with a spatial resolution

of 0.01 μm. The laser performs raster scanning of the workpiece surface (see Fig. 4.3(a)) collecting discrete height measurements every 1 μm in a rectangular region surrounding the crater. The obtained data is plotted to represent the 3D topography of the crater as shown in Fig. 4.3(b). The amount of material removed during the discharge is characterized in terms of the volume below the surface of the workpiece (crater volume) as shown in Fig. 4.3(c).
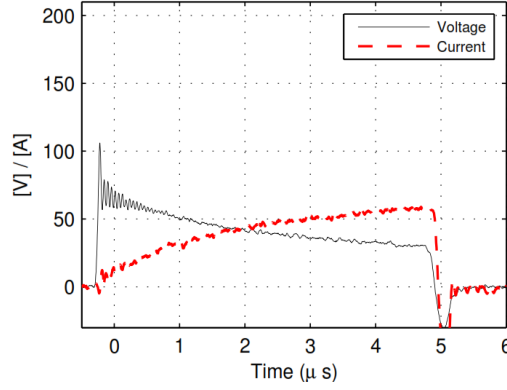
Figure 4.2: Voltage and current plots during a single EDM discharge.
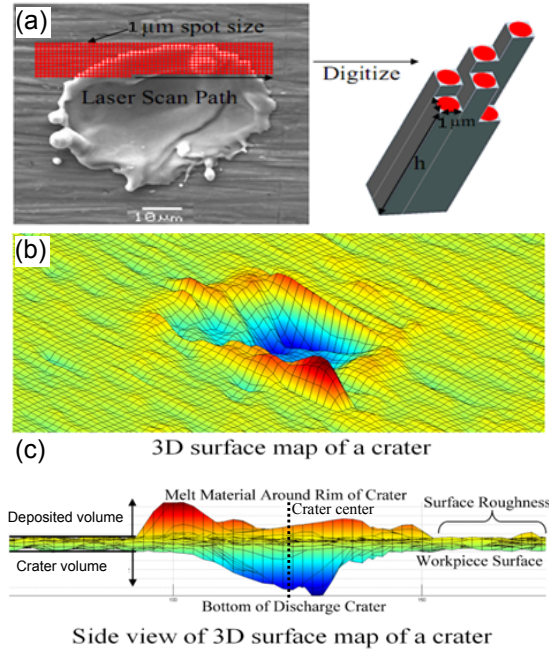
Figure 4.3: 3D topography of crater using laser scanning [19]

4.2   Validation of Debris Flushing Model

In Spray-EDM, the debris particles are concentrated on one side of the crater due to the moving film. In order to eliminate the variability induced in the experimental debris distribution due to the direction of film motion, the debris flushing model is validated for stationary dielectric ($v_f = 0$). About 200 single discharges are carried out using a stationary dielectric for the conditions listed in Table 4.1 to generate sufficient number of debris for characterization. After performing the discharges, the machined surface is scanned using a JEOL 6060 LV Scanning Electron Microscopy (SEM) to obtain high magnification images of the crater with debris particles surrounding it. A sample image of the work-surface with crater and debris particles is shown in Fig. 4.4.

Table 4.1:   Conditions for the single-discharge experiments

Open circuit voltage, V_o	200 V
Inter-electrode gap, d_{gap}	2 μm
Pulse-on time, t_{on}	5 μs
Tool	Tungsten (100 μm diameter)
Work piece	Stainless Steel
Dielectric	Chem Finish EDM 3001 Lite

The distance of each debris particle from the center of the crater is evaluated using a MATLAB$^{\text{TM}}$ script. This is achieved by calculating the number of pixels between the two points, viz., the crater center and the position of debris and then computing the distance in μm by using the calibration bar for the SEM image. The distance of all debris from the crater center is evaluated in a similar manner. The number of particles on the surface are measured for successive intervals of 25 μm from the crater center and the percentage distribution is calculated. The mean and standard deviation, $\mu \pm \sigma$, of the percentage of particles from the SEM images are evaluated.

The distribution of debris around the crater is also determined using the model developed in Chapter 3. Since the numerical model requires the mean debris par-
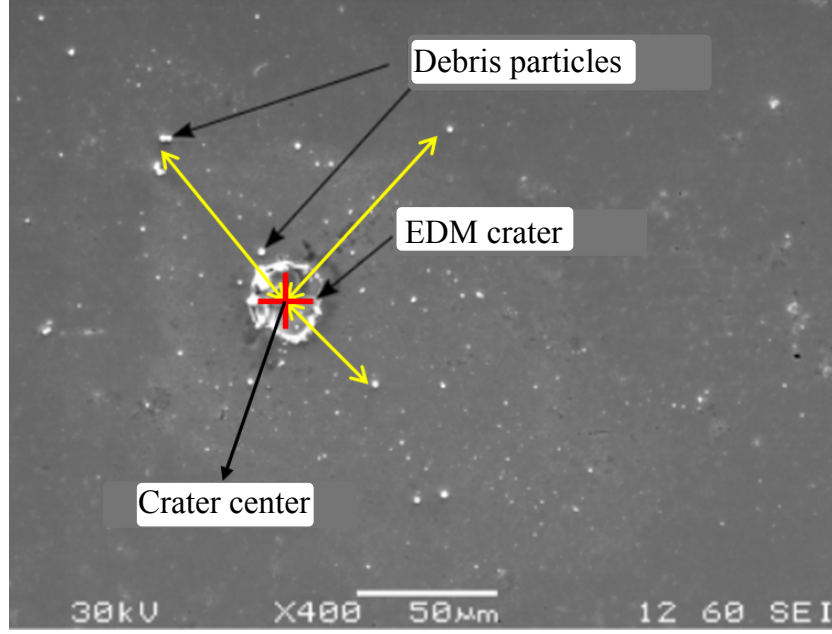
Figure 4.4: SEM image of EDM crater and debris particles

ticle size, debris obtained through single-discharge experiments are collected and analyzed using a Laser Particle Size Analyzer (Zetasizer Nano, Malvern Instruments Ltd., UK). The particles in EDM oil are agitated slightly in an ultrasonic container to enable suspension and also prevent them from coagulating prior to measuring their size. The mean diameter of debris particles is estimated to be 1.31 μm. The ejection velocity of the debris particles is determined to be about 270 m/s by using the methodology developed in [118] and the physical properties of stainless steel. Also, for an open circuit voltage of 100 V and pulse on-time of 5 μs, plasma pressure of 25 MPa as reported in [119] is used, and the plasma radius is computed using the relationship given by Patel *et. al* [120] as $0.788t_{on}^{0.75}$.

The boundary conditions and the initial conditions of the model as discussed in Sec. 3.5.1 have been used. The trajectory of debris particles as predicted by the model is shown in Fig. 4.5, where, each line represents the path taken by a single debris particle. The dielectric fluid is pushed outward to both sides from the center of EDM crater due to the pressure exerted by the plasma. Hence, the debris particles are found to be distributed on both sides of the crater for this case. The 'trap boundary condition' on the machining surface ensures that

114

the debris striking the surface adhere to it and the coordinates of the points of impact are recorded. The debris distribution is obtained by post-processing the coordinate positions at which the debris particles strike the work surface. This data is recorded for a duration of 1 ms after the discharge takes place since most of the debris are found to be deposited on the machining surface within that duration.

The percentage of debris within successive intervals of 25 μm from the crater center is compared for both the experiments and those obtained from the debris flushing model, and the results are shown in Fig. 4.6. In this plot, the percentage of particles within an interval of 25 μm is marked at the mid-point of the corresponding interval. For example, in the range of 0-25 μm from the crater center, the percentage of particles (about 21%) is marked at 12.5 μm. For the second interval, it is marked at 37.5 μm and so on. It is observed from Fig. 4.6 that the overall trend of debris distribution around the crater is in good agreement with the experimental measurements.
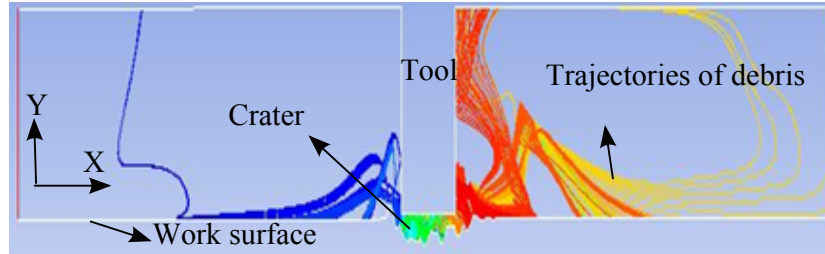
Figure 4.5: Simulated trajectory of debris particles for stationary dielectric fluid.
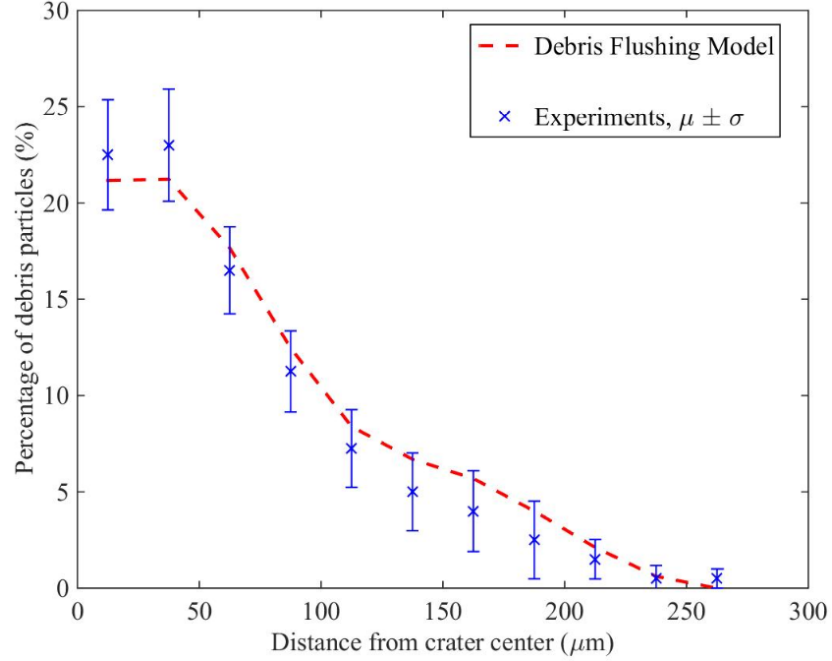
Figure 4.6: Comparison of debris distribution for experiments and computational model.

Effect of spray parameters on debris flushing

The validated debris flushing model is used to determine the distribution of debris particles for different combinations of spray parameters. For a gap distance of 1 μm, the conditions 1, 4 and 5 listed in Table 3.2 ensure that the gap is completely filled with dielectric, i.e. $h_f \geq d_{gap}$, while the other conditions have lower film thickness and are not suitable for Spray-EDM as discussed in Sec. 3.4. The average values of h_f and v_f within the stable region between -180 mm and -200 mm from the impingement point are computed. Their values for the aforementioned conditions are used in the debris flushing model and are shown in Table 4.2.

The trajectory of the debris particles in the region close to the EDM crater for the different conditions is shown in Fig. 4.7. Note that the crater and the tool electrode are within the stable region of the dielectric film formed on the machining surface, i.e. between a distance of -180 mm and -200 mm from the point of spray impingement. As discussed earlier, the debris are distributed on

Table 4.2: Film parameters used in the debris flushing model

Test conditions from Table 3.2	4	5	1
P (MPa)	0.2	0.4	0.2
d (mm)	109.5	109.5	84.5
h_f (μm)	3.5	3	6.05
v_f (mm/s)	0.53	1.15	1.55

both sides of the crater for the stationary dielectric condition. However, in the case of Spray-EDM, the debris are pushed by the moving dielectric film to one side of the crater. In Fig. 4.7, the dielectric film flows from left to right as indicated and hence, more debris are found on the right side of the crater. With an increase in film velocity, the ability of the dielectric film to carry the debris particles is improved as observed from the trajectories in Fig. 4.7. The distance of the trajectories from the machining surface increases as the film velocity is increased from 0.53 mm/s to 1.55 mm/s as seen from Fig. 4.7 (b), (c) and (d). Thus, the debris are carried farther from the crater before being deposited on the machining surface.
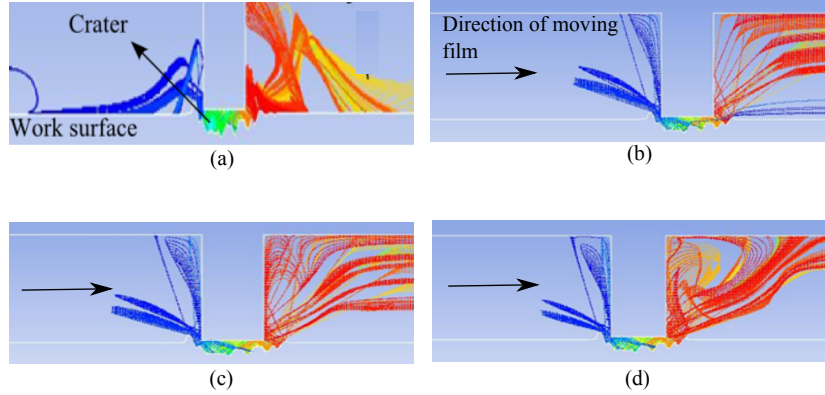
Figure 4.7: Comparison of debris trajectories for different conditions (a) Stationary dielectric fluid, (b) P=0.2 MPa, d=109.5 mm, (c) P=0.4 MPa, d=109.5 mm and (d) P=0.2 MPa, d=84.5 mm.

The debris distribution around the craters for Spray-EDM with the different combinations of spray parameters is shown in Fig. 4.8 along with that obtained using stationary dielectric. The proportion of debris particles within a 100 μm

distance from the crater center is about 40%, 31.5% and 28% for the conditions 4, 5 and 1 as listed in Table 4.2, respectively. For the stationary dielectric condition, about 75% of particles are observed within a 100 μm distance from the crater center. The improvement in debris flushing from the discharge zone as compared to the stationary dielectric condition is due to the higher velocity of the flowing dielectric film in Spray-EDM that carries the debris particles farther from the crater. As seen from Fig. 4.8, all the debris particles are observed to be within a distance of 240 μm for the stationary dielectric. However, for the Spray-EDM conditions, the debris are found to be deposited at regions farther from the crater. The moving film has sufficient velocity near the crater to carry the debris particles farther. However, beyond a certain distance, the film velocity reduces and gradual deposition of debris on the machining surface occurs. Among the three conditions for Spray-EDM, the combination of P=0.2 MPa and d=84.5 mm is observed to have the best flushing capability due to higher velocity of the dielectric film (1.55 mm/s vs 0.53 and 1.15 mm/s).
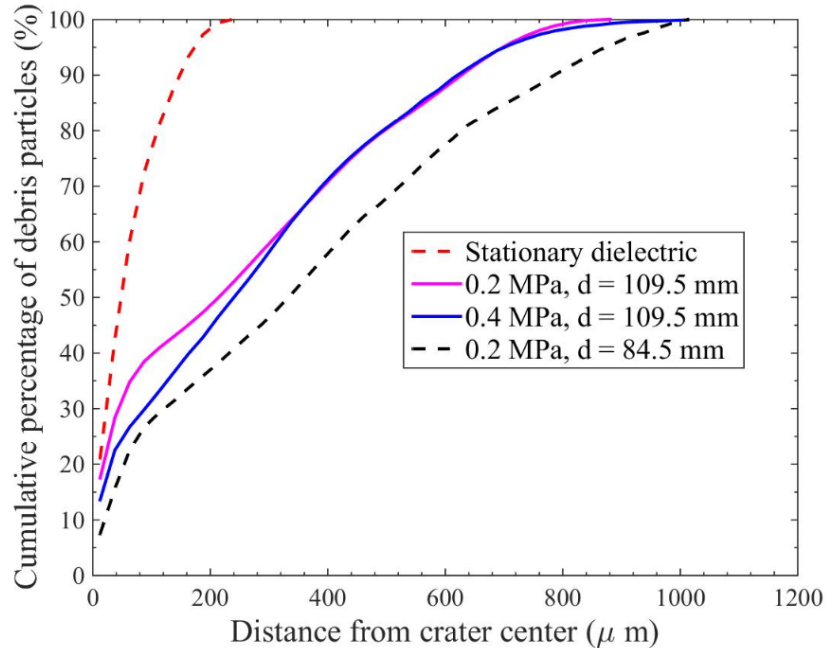
Figure 4.8: Comparison of debris distribution for different spray conditions.

4.3 Comparison of Spray-EDM, Wet-EDM and Dry-EDM Processes

The second set of single-discharge EDM experiments are conducted to evaluate the performance of the Spray-EDM process. Experiments are also performed for Wet-EDM (using stagnant dielectric) and Dry-EDM to compare the machining characteristics with that of the Spray-EDM process. Chem Finish EDM 3001 Lite^{TM} was used as the dielectric for Wet-EDM and Spray-EDM experiments, while air was used for Dry-EDM. The Spray-EDM experiments are performed using the spray parameters of P=0.4 MPa and d=109.5 mm due to the better flushing ability compared to the stationary dielectric condition as discussed in Sec. 4.2. Discharge parameters such as open gap voltage (V_o) and pulse-on time (t_{on}) are varied to evaluate the performance of the EDM process with different dielectric supply methods across a range of discharge energies. A 2^2 full factorial design with two levels for V_o and t_{on} is adopted as shown in Table 4.3.

Table 4.3: Factor levels for EDM experiments

Parameters	Low	High
Open gap voltage, V_o (V)	100	250
Pulse-on time, t_{on} (μs)	5	50

The inter-electrode gap distance (d_{gap}) was kept constant at 1μm for all cases and the experiment was performed for Wet, Dry, and Spray-EDM techniques. A gap of 1μm ensures that the electric field within the gap, $E = V_o/d_{gap}$ is greater than the dielectric strength of air and Chem Finish EDM 3001 Lite^{TM} for both voltage values considered. In Wet-EDM, the electrodes are immersed in a small tank containing EDM oil. Dry air at a pressure of 0.4 MPa is used for Dry-EDM experiments. In the case of Spray-EDM, droplets of EDM oil produced by an ultrasonic atomizer operating at 40 kHz are supplied at a flow rate of 10 ml/min by carrier gas (air) at a pressure of 0.4 MPa to the machining zone. Experiment is

repeated 30 times for each set of process parameters to determine the variability in experimental data. The three processes are compared in terms of the discharge energy, the volume of material removed, tool electrode wear and the flushing of debris from the machining region.

4.3.1 Comparison of Discharge Energy and Crater Characteristics

Figures 4.9 (a) and (b) show a comparison of discharge energy and volume of crater, respectively for the three EDM processes at different discharge conditions. The discharge energy for each condition is determined using the current and voltage values recorded by the Oscilloscope during the discharge process. As seen in Fig. 4.9(a), the discharge energy produced in Spray-EDM is highest among all the three processes, suggesting that the flow of dielectric in the form of thin film has a significant effect on the discharge process. In comparison, the discharge energy produced due to Dry-EDM is the least among the three process due to poor dielectric strength of air. The discharge energy produced by Spray-EDM is about 37% higher on an average across the discharge energies considered than that of Wet-EDM. The physics behind this observation is shown in Fig. 4.10. The higher discharge energy in Spray-EDM is attributed to the increased electrical resistance offered by the moving dielectric compared to a static dielectric medium. For a constant circuit current, I, the power given by I^2R is greater for a higher electrical resistance across the electrodes. Hence, a higher proportion of the applied energy goes into the discharge process compared to the case with static dielectric. The increased electrical resistance offered by the moving dielectric medium such as oils used in transformers has been extensively studied in Refs. [121, 122]. The authors attributed the higher resistance could be due to one or more of the following reasons: (i) increased resistance to the formation of particle chains across the inter-electrode gap due to continuous washing, (ii) prevention of formation and growth of vapor bubbles at the electrode surfaces due to the cooling effect of the moving fluid and (iii) modification of the space charge distribution in the

inter-electrode gap due to moving fluid. The crater volume shown in Fig. 4.9 (b) is determined from a three-dimensional topography of the crater obtained using a surface scanning laser as discussed in Sec. 4.1. From the topography of the crater, the volume of material below the work surface is determined using a MATLAB^{TM} script. Due to the higher discharge energy associated with the Spray-EDM process, an average increase in crater volume of about 78% compared to Wet-EDM is observed across the discharge energies considered in this study.

4.3.2   Tool Electrode Wear

Figures 4.11(a)-(f) show a comparison of SEM images of tool electrode before and after 5 discharges using the three different EDM processes. The tool electrode was examined using a JEOL 6060 LV Scanning Electroscope Microscope (SEM) to investigate the electrode wear after 5 discharges for wet, dry, and Spray-EDM methods for V_o=250 V and $t_{on} = 50\mu$s. These conditions correspond to a discharge energy that is marginally higher than that commonly employed in typical μ-EDM applications and were selected here to observe tool wear at extreme discharge conditions. The tool wear is quantified by Δ, which is the difference in length of the tool electrode before and after performing the discharges. From Figs. 4.11 (a)-(f), it is evident that Dry-EDM, using air as the dielectric, produced the highest tool wear. This is because of the low heat-removing capability of air coupled with poor flushing of debris particles that exert a higher thermal load on the tool. Among the Wet-EDM and Spray-EDM, tool wear in the latter is marginally lower than the former. Although the dielectric properties are the same, the flowing dielectric in the case of Spray-EDM resulted in a marginal improvement in tool wear in comparison to Wet-EDM. The higher plasma discharge energy in the case of Spray-EDM compared to Wet-EDM should result in greater tool wear. However this effect is compensated by an improved heat removal capability of the flowing dielectric film in comparison to Wet-EDM, thereby resulting in similar tool wear. Note that with nearly the same tool wear, the material removal in the
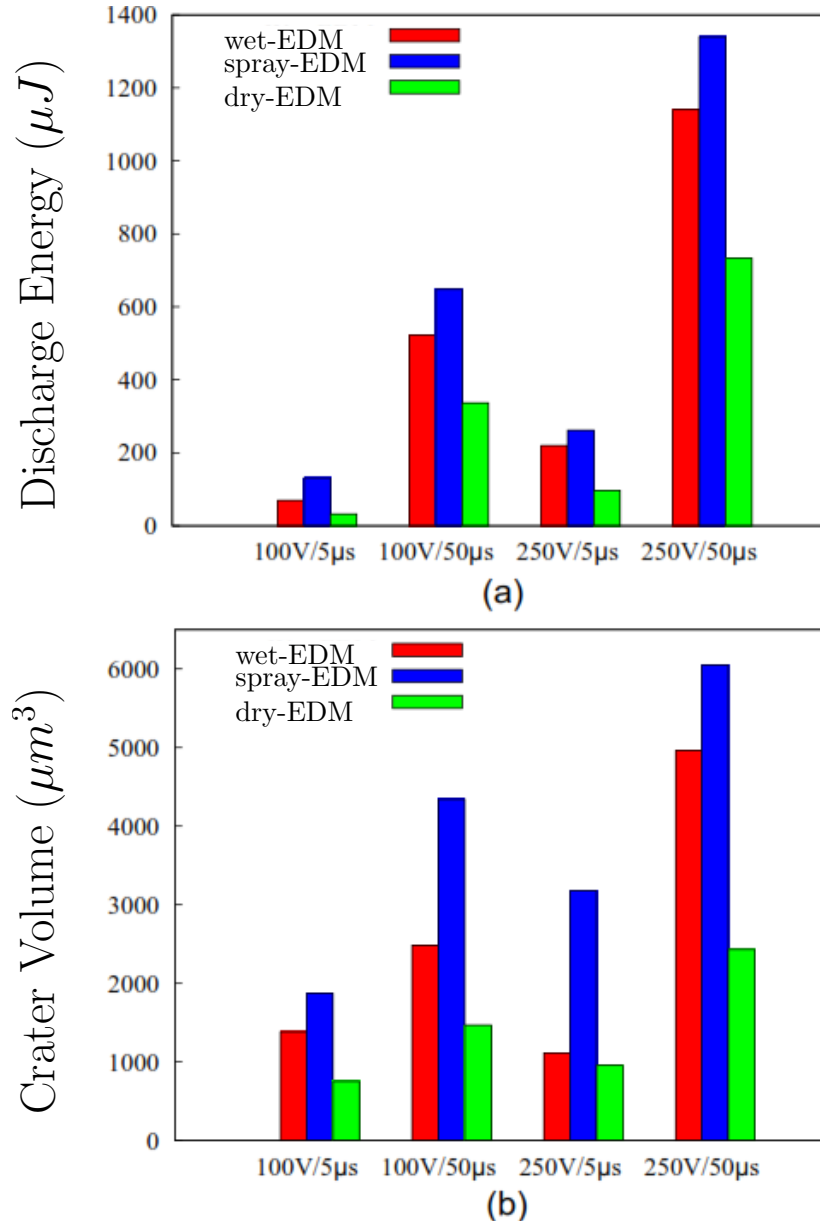
Figure 4.9: Comparison of Wet-EDM, Spray-EDM and Dry-EDM (a) discharge energy, (b) crater volume

continuous washing of inter-electrode gap	→	increased resistance to the formation of particle chains		
cooling effect of the moving fluid	→	prevention of formation and growth of vapor bubbles at the electrode surfaces	→	Higher electrical resistance across electrodes
moving fluid	→	modification of the space charge distribution in the inter-electrode gap		

Constant circuit current, I and higher resistance, R	→	Higher power, I^2R	→	higher proportion of the applied energy goes into the discharge compared to the case with static dielectric.

Figure 4.10: Physics behind the higher discharge energy in Spray-EDM.

case of Spray-EDM is significantly higher compared to Wet-EDM. Therefore, the Spray-EDM process proposed in this work not only reduces the consumption of dielectric fluid, but is also observed to improve the machining characteristics of EDM process.

4.3.3   Distribution of Debris Particles

The distribution of debris around the crater was investigated based on the SEM images of regions around crater to determine the flushing capability in each case. For this analysis, single-discharge experiments with V_o=250 V and $t_{on} = 50$ μs were performed. 30 craters were studied for debris particles distribution in each case and the SEM images are shown in Fig. 4.12. From Fig. 4.12, it is observed that the debris are concentrated on one side of the crater due to the moving dielectric film in the case of Spray-EDM. However, in wet and Dry-EDM, the debris are distributed randomly in all directions around the crater. Figures 4.13(a)-(c) shows the distribution of debris particles from the center of the crater (shown in Fig. 4.3) for Wet-EDM, Spray-EDM and Dry-EDM, respectively. From Fig. 4.13(c), about 88 % of the debris particles are observed within 100 μm from the crater center. The poor flushing ability of the gaseous dielectric results in deposition of debris
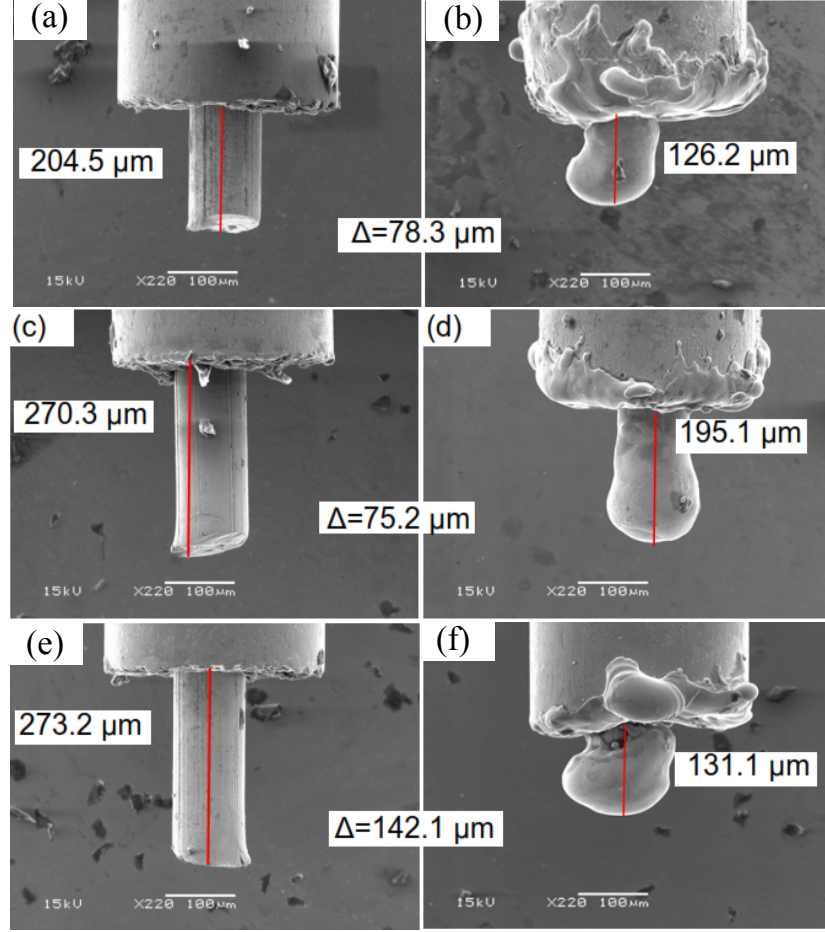
Figure 4.11: SEM images of tool electrodes before and after 5 discharges. (a) and (b): Wet-EDM; (c) and (d): Spray-EDM; (e) and (f): Dry-EDM

particles closer to the machined crater. In the case of Wet-EDM, about 62 % of the particles are deposited within 100 μm from the crater center. The higher viscosity of the liquid dielectric carries the debris particles further away from the crater center. However, in the case of Spray-EDM, only 46 % of the debris particles are found within 100 μm from the crater center. This improvement in debris flushing from the discharge zone is mainly due to the flowing dielectric film that carries the debris particles along with it.
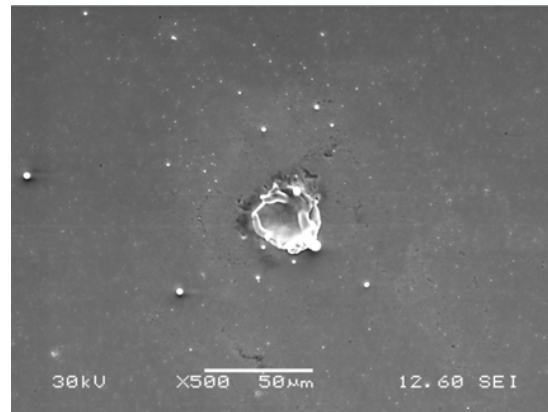
(a)
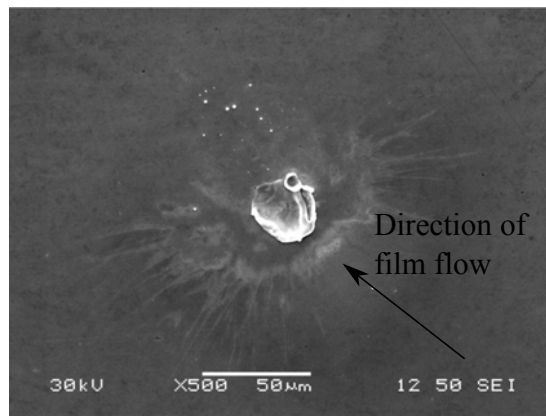
(b)
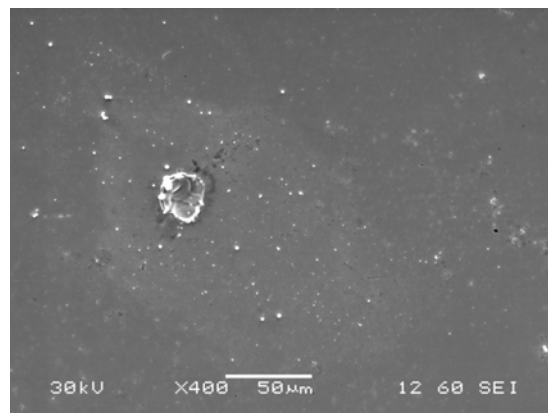
(c)

Figure 4.12: SEM images of debris particles around the EDM crater: (a) Wet-EDM; (b) Spray-EDM; (c) Dry-EDM
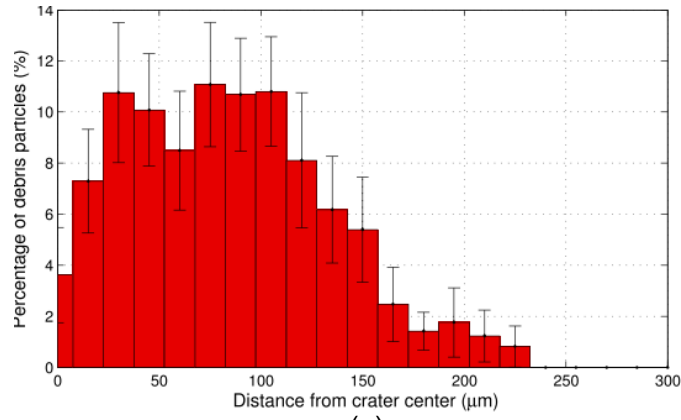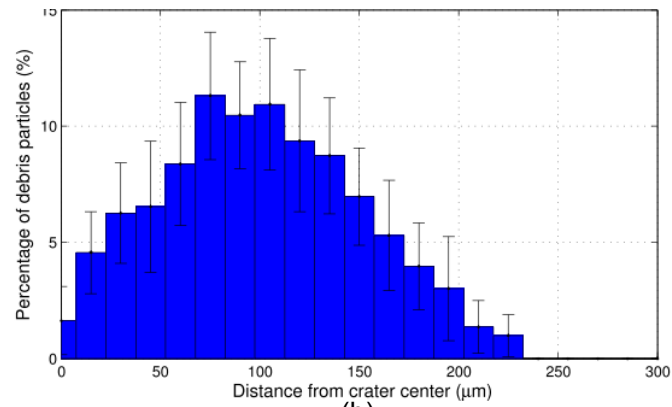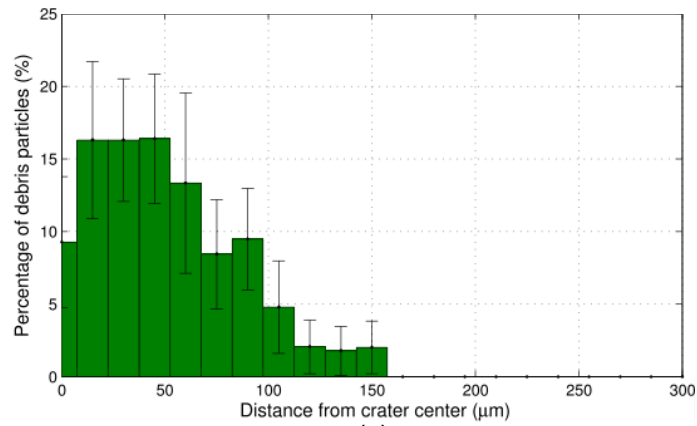
Figure 4.13: Distribution of debris particles from the crater center: (a) Wet-EDM; (b) Spray-EDM; (c) Dry-EDM

4.4 Summary

In this chapter, single-discharge EDM experiments were performed to validate a computational model developed to study the flushing of debris in Spray-EDM process. The validated model was used to determine the combination of spray parameters that resulted in enhanced flushing. EDM experiments were also done to evaluate the performance of Spray-EDM process and compare it with Wet and Dry-EDM processes. Specific conclusions of the chapter are as follows.

1. The percentage of debris within a distance of 100 μm from crater center is reduced from about 75% for the stationary dielectric condition to about 28% for Spray-EDM with a gas pressure of 0.2 MPa, impingement angle of 30° and distance between nozzle exit and machining surface of 125 mm. It is observed that dielectric films with higher velocity improve the flushing of debris from the discharge zone.

2. The discharge energy in the Spray-EDM process is 37% higher compared to Wet-EDM. This is attributed to the increased electrical resistance offered by the moving dielectric compared to a static dielectric medium, thereby a higher amount of the applied energy goes into the discharge process in Spray-EDM.

3. The volume of material removed in the Spray-EDM process is 78% higher than that observed during Wet-EDM across the range of discharge energies considered in this research.

4. The tool wear in Spray-EDM is lesser than Dry-EDM due to the better heat-removal capability of the flowing liquid film and comparable to that observed in Wet-EDM.

Chapter 5

Conclusions and Recommendations

The objective of this thesis was to develop a novel Spray-EDM process that not only minimizes the consumption of the dielectric fluid but also improves the flushing of debris from the inter-electrode gap. The research involved the development of computational models based on CFD approach to understand the phenomena associated with Spray-EDM including dielectric spray formation, film formation on the machining surface and the flushing of debris from the inter-electrode gap and create a fundamental knowledge-base for the Spray-EDM process. The dielectric spray model was developed to study the effect of spray system parameters on the gas velocity and droplet velocities. The compressibility effects of the carrier gas were taken into account in the model. The collision and coalescence among the droplets and also the momentum transfer between the two phases, viz., the carrier gas and the droplets were also considered in the model. The film formation model was developed to determine the spatial variation in film thickness and velocity on the machining surface for different spray system parameters. The Eulerian Wall Film (EWF) approach was used for modeling the mass and momentum transfer from the dielectric droplets to the film formed on the surface. Both the models were validated by comparing the model predictions with the experimental data.

The debris flushing model was developed to understand the effect of moving dielectric film on the flushing of debris from the inter-electrode gap. Critical process-related factors including the actual topography of the machined crater, plasma pressure and radius, and non-uniform size of debris particles were considered in the model. The model was validated by comparing the model predictions of debris distribution with experimental data for stationary dielectric condition. Using the

128

knowledge-base developed through the computational research, the performance of the Spray-EDM process was evaluated by single-discharge EDM experiments. The performance was then compared with Wet-EDM and Dry-EDM techniques in terms of material removal, tool electrode wear and debris flushing.

5.1   Conclusions

The specific conclusions of the research are as follows.

1. A three-dimensional and transient dielectric spray model model was developed to understand the atomization of dielectric droplets and dielectric spray formation. The compressible flow of carrier gas, interaction between the carrier gas and the dielectric droplets, collision and coalescence among the droplets were taken into account in the dielectric spray model.

2. The model was validated by comparing the experimental measurements of carrier gas velocity with those predicted by the model. The gas velocity near the nozzle exit becomes higher with increasing carrier gas pressures due to the higher values of stagnation pressure. An exponential decay in the carrier gas velocity with increasing distance from nozzle exit is observed for all the gas pressures considered. It is observed that the trend of gas velocities from the model and experiments is similar and the values are in good agreement, especially beyond a distance of 20 mm from exit, where the variation is less than 10%. A slight variation in the velocity of gas is observed in the regions close to nozzle exit. This is attributed to the fact that the experimental values of velocity are calculated from dynamic pressure measurements by assuming constant density for the carrier gas.

3. The dielectric spray model is used to determine the spatial variation in droplet velocity for different carrier gas pressures. The velocity of droplets at a specific distance from the nozzle exit is higher for higher carrier gas

pressures. The droplets closer to the nozzle exit have a lower velocity even though the gas velocity is higher in those regions. This is because the droplets are gradually accelerated from their initial velocity and reach their peak values after traveling a short distance in the gas phase. The maximum average velocity of droplets is observed at a distance of about 30-35 mm from the exit for all the gas pressures considered. Beyond this distance, the dielectric droplets are decelerated by the slower moving gas and reach a fairly constant velocity after about 200 mm. Also, the velocity of droplets is always lower than the carrier gas velocity at a given distance from the nozzle exit.

4. The velocity of dielectric droplets predicted from the dielectric spray model is used along with the theory of droplet impingement dynamics to determine the range of impingement angles that ensures film formation on the machining surface, i.e. the droplet-surface interaction is within the spreading regime. Higher impingement angles could be used with smaller gas pressures or larger distances from droplet nozzle exit due to the smaller droplet normal velocities associated with these conditions.

5. The film formation model was developed to understand the interaction between the dielectric droplets and the machining surface. The model is used to determine the thickness and velocity of the thin dielectric film formed on the machining surface for different combinations of spray parameters including carrier gas pressure, angle of spray impingement and distance between the nozzle exit and machining surface. The impingement of droplets on a thin layer of dielectric film, film spreading due to gravity and surface tension effects are included in this model.

6. The model was validated by comparing the thickness of the film formed on a target surface for different combinations of spray parameters. The film thickness is higher in the regions closer to the spray impingement point due

to the effect of the normal component of gas velocity on the film. Beyond the unstable region, a gradual reduction in the film thickness is observed for all the conditions. The model predictions show a trend of reducing film thickness with distance from the spray impingement point and is similar to the experimental measurements within the stable region of the film (-160 mm to -200 mm from impingement point). The difference between the model predictions and experiments is attributed to the effect of actual topography of the machining surface on the film formation phenomenon.

7. It is observed that distance between the nozzle exit and the machining surface influences the thickness to a greater extent than the carrier gas pressure. Large distances result in smaller thickness due to a reduction in the flux of droplets impacting on the surface. Higher gas pressures result in higher film velocities for a given distance between nozzle and machining surface.

8. A 2D debris flushing model was developed to understand the debris flushing phenomenon in EDM process by taking into account the pressure exerted by the plasma, non-uniform size of debris particles and the actual topography of the crater formed during machining. A two-dimensional model is sufficient to model the effect of flowing film on debris flushing since the velocity of the film along the direction of spray is much higher compared to the other directions. The debris produced by single-discharge experiments were analyzed using a Laser Particle Size Analyzer to determine the particle size distribution and a digital topography of the EDM crater was obtained by performing raster scanning of the machined surface using a surface scanning laser.

9. The percentage of debris within a distance of 100 μm from crater center is reduced from about 75% for the stationary dielectric condition to about 28% for Spray-EDM with gas pressure of 0.2 MPa, impingement angle of 30° and distance between nozzle exit and surface of 125 mm. It is observed

that dielectric films with higher velocity improve the flushing of debris from the discharge zone.

10. The discharge energy in the Spray-EDM process is 37% higher compared to Wet-EDM. This is attributed to the increased electrical resistance offered by the moving dielectric compared to a static dielectric medium, thereby a higher amount of the applied energy goes into the discharge process in Spray-EDM.

11. The volume of material removed in the Spray-EDM process is 78% higher than that observed during Wet-EDM across the range of discharge energies considered in this research.

12. The tool electrode wear in Spray-EDM is only 75.2 μm compared to 142.1 μm observed for Dry-EDM due to the better heat-removal capability of the flowing liquid film. It is also comparable to that observed in Wet-EDM (78.3 μm).

5.2   Recommendations for Future Work

Some of the suggestions for extending this research to develop an efficient Spary-EDM process are described below.

1. EDM experiments with multiple discharges need to be performed to evaluate the performance of Spray-EDM that could be used for commercial applications. In multiple discharges, the location of discharge within the machining region is random and that region must have a moving dielectric film with sufficient velocity for debris removal. The direction of film flow with respect to the discharge locations plays a significant role in the flushing of debris in the case of multiple discharges and hence this phenomenon needs to be investigated.

2. Additional workpiece-tool electrode material combinations need to be tested to determine the effectiveness of flushing using the Spray-EDM technique

for different machining conditions. The density of the debris produced from the workpiece material influences the trajectories of the particles. Hence, the debris flushing with Spray-EDM for different workpiece materials needs to be investigated.

3. Only a few combinations of discharge parameters including open circuit voltage and pulse-on time were tested in this research. The inter-electrode gap distance plays a significant role in the flow of thin dielectric film on the machining surface and debris removal from the machining region. Hence, a parametric study taking into account different inter-electrode gap distances and duty cycle factors (for multiple discharge experiments) needs to be performed to identify the optimal combination of discharge parameters that could be used in the Spray-EDM process.

4. The design parameters of the droplet and carrier gas nozzle need to be optimized for producing a focused dielectric spray with minimum spray diameter at the focal point and also to control the flux of droplets in the spray. An optimal configuration of the droplet and gas nozzle for the Spray-EDM process would produce effective entrainment of droplets in the carrier gas, thereby minimizing the dispersion of droplets into the ambient.

5. The roughness of the machining surface plays a significant role in the droplet-surface interaction and the ensuing film formation phenomenon [123]. The surface roughness and surface energy influence the contact angle between the droplet and the machining surface, which in turn influences the film formation. Also, the temperature of the EDM plasma alters the nature of the machining surface due to the formation of a recast layer, which might not have the same effect on the droplet interaction and film formation phenomenon as the original surface. This is a significant factor, especially for EDM with multiple discharges since a larger area is subject to the plasma discharges.

6. Only the die-sinking EDM process was investigated in this research. The performance of the Spray-EDM technique in wire-EDM and EDM-drilling applications could be investigated since the formation of films in these cases is quite different from that in die-sinking EDM. In the case of EDM drilling, it must be ensured that the surfaces of the holes are wetted by the dielectric and a film is formed between the surface and electrode. In the case of wire-EDM, the continuous movement of the EDM wire during machining could influence the film formation. Also, the effect of gravity on the film formed on the wire electrode needs to be taken into account. This is a significant difference in wire-EDM compared to the die-sinking EDM process.

7. A three-dimensional model for debris flushing with the actual machined surface topography could be developed to account for the variation in film thickness and velocity in three dimensions. Such a model will enable the accurate determination of debris distribution around the EDM crater. However, better meshing algorithms like patch-independent meshing methods that create a volume mesh before generating a surface mesh for complex geometry need to be used.

References

[1] K. G. Heinz, "Fundamental study of magnetic field-assisted micro-edm for non-magnetic materials," M.S. thesis, University of Illinois at Urbana-Champaign, 2010.

[2] A. Descoeudres, "Characterization of edm plasmas," Ph.D. dissertation, Ecole Polytechnique Federale De Lausanne, 2006.

[3] J. C. Devins, S. J. Rzad, and R. J. Schwabe, "Breakdown and prebreakdown phenomena in liquids," *Journal of Applied Physics*, vol. 52, no. 7, pp. 4531–4545, 1981.

[4] S. H. Yeo, W. Kurnia, and P. C. Tan, "Electro-thermal modelling of anode and cathode in micro-edm," *Journal of Physics D: Applied Physics*, vol. 40, no. 8, pp. 2513–2521, 2007.

[5] F. N. Leo and I. R. Pashby, "A review on the use of environmentally-friendly dielectric fluids in Electrical Discharge Machining," *Journal of Materials Processing Technology*, vol. 149, no. 1–3, pp. 341–346, 2004.

[6] N. M. Abbas, D. G. Solomon, and M. F. Bahari, "A review on current research trends in electrical discharge machining (edm)," *International Journal of Machine Tools and Manufacture*, vol. 47, no. 7-8, pp. 1214–1228, 2007.

[7] M. Kunieda, Y. Miyoshi, T. Takaya, N. Nakajima, Y. Z. Bo, and M. Yoshida, "High speed 3D milling by dry EDM," *CIRP Annals - Manufacturing Technology*, vol. 52, no. 1, pp. 147–150, 2003.

[8] C. C. Kao, J. Tao, and A. J. Shih, "Near dry electrical discharge machining," *International Journal of Machine Tools and Manufacture*, vol. 47, no. 15, pp. 2273–2281, 2007.

[9] S. L. Chen, B. H. Yan, and F. Y. Huang, "Influence of kerosene and distilled water as dielectrics on the electric discharge machining characteristics of ti-6a1-4v," *Journal of Materials Processing Technology*, vol. 87, no. 1-3, pp. 107–111, 1999.

[10] T. Masuzawa, X. Cui, and N. Taniguchi, "Improved jet flushing for edm," *CIRP Annals - Manufacturing Technology*, vol. 41, no. 1, pp. 239–242, 1992.

[11] Y. H. Guu and H. Hocheng, "Effects of workpiece rotation on machinability during electrical-discharge machining," *Materials and Manufacturing Processes*, vol. 16, no. 1, pp. 91–101, 2001.

[12] J. S. Soni, "Microanalysis of debris formed during rotary edm of titanium alloy (ti 6a1 4v) and die steel (t 215 cr12)," *Wear*, vol. 177, no. 1, pp. 71–79, 1994.

[13] M. Ghoreishi and J. Atkinson, "A comparative experimental study of machining characteristics in vibratory, rotary and vibro-rotary electro-discharge machining," *Journal of Materials Processing Technology*, vol. 120, no. 1-3, pp. 374–384, 2002.

[14] M. P. Jahan, T. Saleh, M. Rahman, and Y. S. Wong, "Development, modeling, and experimental investigation of low frequency workpiece vibration-assisted micro-edm of tungsten carbide," *Journal of Manufacturing Science and Engineering, Transactions of the ASME*, vol. 132, no. 5, 2010.

[15] C. Gao and Z. Liu, "A study of ultrasonically aided micro-electrical-discharge machining by the application of workpiece vibration," *Journal of Materials Processing Technology*, vol. 139, no. 1-3 SPEC, pp. 226–228, 2003.

[16] H. Huang, H. Zhang, L. Zhou, and H. Y. Zheng, "Ultrasonic vibration assisted electro-discharge machining of microholes in nitinol," *Journal of Micromechanics and Microengineering*, vol. 13, no. 5, pp. 693–700, 2003.

[17] S. H. Yeo, M. Murali, and H. T. Cheah, "Magnetic field assisted micro electro-discharge machining," *Journal of Micromechanics and Microengineering*, vol. 14, no. 11, pp. 1526–1529, 2004.

[18] Y. C. Lin and H. S. Lee, "Optimization of machining parameters using magnetic-force-assisted edm based on gray relational analysis," *International Journal of Advanced Manufacturing Technology*, vol. 42, no. 11-12, pp. 1052–1064, 2009.

[19] K. Heinz, S. G. Kapoor, R. E. DeVor, and V. Surla, "An investigation of magnetic-field-assisted material removal in micro-edm for nonmagnetic materials," *Journal of Manufacturing Science and Engineering, Transactions of the ASME*, vol. 133, no. 2, p. 021002, 2011.

[20] A. Okada, Y. Uno, S. Onoda, and S. Habib, "Computational fluid dynamics analysis of working fluid flow and debris movement in wire edmed kerf," *CIRP Annals - Manufacturing Technology*, vol. 58, no. 1, pp. 209–212, 2009.

[21] S. Cetin, A. Okada, and Y. Uno, "Electrode jump motion in linear motor equipped die-sinking edm," *Journal of Manufacturing Science and Engineering, Transactions of the ASME*, vol. 125, no. 4, pp. 809–815, 2003.

[22] J. Wang and F. Han, "Simulation model of debris and bubble movement in consecutive-pulse discharge of electrical discharge machining," *International Journal of Machine Tools and Manufacture*, vol. 77, no. 0, pp. 56–65, 2 2014.

[23] S. A. Mastud, N. S. Kothari, R. K. Singh, and S. S. Joshi, "Modeling debris motion in vibration assisted reverse micro electrical discharge machining process (r-medm)," *Journal of Microelectromechanical Systems*, 2014, article in Press.

[24] M. B. G. Jun, S. S. Joshi, R. E. DeVor, and S. G. Kapoor, "An experimental evaluation of an atomization-based cutting fluid application system for micromachining," *Journal of Manufacturing Science and Engineering, Transactions of the ASME*, vol. 130, no. 3, pp. 0 311 181–0 311 188, 2008.

[25] A. C. Hoyne, "A study on the fluid film of an Atomization-based Cutting Fluid (ACF) spray system during titanium machining," M.S. thesis, University of Illinois at Urbana-Champaign, 2013.

[26] C. Nath, S. G. Kapoor, R. E. DeVor, A. K. Srivastava, and J. Iverson, "Design and evaluation of an atomization-based cutting fluid spray system in turning of titanium alloy," *Journal of Manufacturing Processes*, vol. 14, no. 4, pp. 452–459, 2012.

[27] M. Rein, "Phenomena of liquid drop impact on solid and liquid surfaces," *Fluid Dynamics Research*, vol. 12, no. 2, pp. 61–93, 1993.

[28] C. Mundo, M. Sommerfeld, and C. Tropea, "Droplet-wall collisions: Experimental studies of the deformation and breakup process," *International Journal of Multiphase Flow*, vol. 21, no. 2, pp. 151–173, 1995.

[29] M. Rukosuyev, C. S. Goo, and M. B. G. Jun, "Understanding the effects of the system parameters of an ultrasonic cutting fluid application system for micro-machining," *Journal of Manufacturing Processes*, vol. 12, no. 2, pp. 92–98, 2010.

[30] M. Jeyakumar, G. S. Gupta, and S. Kumar, "Modeling of gas flow inside and outside the nozzle used in spray deposition," *Journal of Materials Processing Technology*, vol. 203, no. 13, pp. 471–479, 7/18 2008.

[31] J. Mi, P. S. Grant, U. Fritsching, O. Belkessam, I. Garmendia, and A. Landaberea, "Multiphysics modelling of the spray forming process," *Materials Science and Engineering A*, vol. 477, no. 1-2, pp. 2–8, 2008.

[32] K. L. Weiner and C. S. Parkin, "The use of computational fluid dynamic code for modelling spray from a mistblower," *Journal of Agricultural Engineering Research*, vol. 55, no. 4, pp. 313–324, 8 1993.

[33] K. R. J. Ellwood and J. Braslaw, "A finite-element model for an electrostatic bell sprayer," *Journal of Electrostatics*, vol. 45, no. 1, pp. 1–23, 1998.

[34] M. Burger, G. Klose, G. Rottenkolber, R. Schmehl, D. Giebert, O. Schfer, R. Koch, and S. Wittig, "A combined eulerian and lagrangian method for prediction of evaporating sprays," *Journal of Engineering for Gas Turbines and Power*, vol. 124, no. 3, pp. 481–488, 2002.

[35] S. A. Colbert and R. A. Cairncross, "A computer simulation for predicting electrostatic spray coating patterns," *Powder Technology*, vol. 151, no. 1–3, pp. 77–86, 2005.

[36] K. H. Ho and S. T. Newman, "State of the art electrical discharge machining (edm)," *International Journal of Machine Tools and Manufacture*, vol. 43, no. 13, pp. 1287–1300, 2003.

[37] J. Fleischer, T. Masuzawa, J. Schmidt, and M. Knoll, "New applications for micro-edm," *Journal of Materials Processing Technology*, vol. 149, no. 1–3, pp. 246–249, 2004.

[38] N. M. Abbas, N. Yusoff, and R. M. Wahab, "Electrical discharge machining (edm): Practices in malaysian industries and possible change towards green manufacturing," in *Procedia Engineering*, vol. 41, 2012, pp. 1684–1688.

[39] H. El-Hofy and H. Youssef, "Environmental hazards of nontraditional machining," in *Proceedings of the 4th IASME/WSEAS International Conference on Energy & Environment*, ser. EE'09. Stevens Point, Wisconsin, USA: World Scientific and Engineering Academy and Society (WSEAS), 2009, pp. 140–145.

[40] R. Kern, Ed., *Safe and Green EDMing, EDM Today*, July/August 2008.

[41] C. L. Goh and S. F. Ho, "Contact dermatitis from dielectric fluids in electrodischarge machining," *Contact Dermatitis*, vol. 28, no. 3, pp. 134–138, 1993.

[42] P. Govindan and S. S. Joshi, "Experimental characterization of material removal in dry electrical discharge drilling," *International Journal of Machine Tools and Manufacture*, vol. 50, no. 5, pp. 431–443, 2010.

[43] L. Liqing and S. Yingjie, "Study of dry edm with oxygen-mixed and cryogenic cooling approaches," *Procedia CIRP*, vol. 6, pp. 344–350, 2013.

[44] G. Skrabalak, J. Kozak, and M. Zybura, "Optimization of dry edm milling process," *Procedia CIRP*, vol. 6, pp. 332–337, 2013.

[45] M. Kunieda, T. Takaya, and S. Nakano, "Improvement of dry edm characteristics using piezoelectric actuator," *CIRP Annals - Manufacturing Technology*, vol. 53, no. 1, pp. 183–186, 2004.

[46] C. Kao, J. Tao, S. Lee, and A. Shih, "Dry wire electrical discharge machining of thin workpiece," vol. 34, 2006, pp. 253–260.

[47] J. Tao, A. J. Shih, and J. Ni, "Experimental study of the dry and near-dry electrical discharge milling processes," *Journal of Manufacturing Science and Engineering, Transactions of the ASME*, vol. 130, no. 1, pp. 0 110 021–0 110 029, 2008.

[48] L. C. Lee, L. C. Lim, V. Narayanan, and V. C. Venkatesh, "Quantification of surface damage of tool steels after edm," *International Journal of Machine Tools and Manufacture*, vol. 28, no. 4, pp. 359–372, 1988.

[49] B. H. Yan and C. C. Wang, "The machining characteristics of al2o3/6061al composite using rotary electro-discharge machining with a tube electrode," *Journal of Materials Processing Technology*, vol. 95, no. 1–3, pp. 222–231, 1999.

[50] J. H. Zhang, T. C. Lee, W. S. Lau, and X. Ai, "Spark erosion with ultrasonic frequency," *Journal of Materials Processing Technology*, vol. 68, no. 1, pp. 83–88, 1997.

[51] S. Joshi, P. Govindan, A. Malshe, and K. Rajurkar, "Experimental characterization of dry edm performed in a pulsating magnetic field," *CIRP Annals - Manufacturing Technology*, vol. 60, no. 1, pp. 239–242, 2011.

[52] A. C. Hoyne, C. Nath, and S. G. Kapoor, "Characterization of fluid film produced by an atomization-based cutting fluid spray system during machining," *Journal of Manufacturing Science and Engineering, Transactions of the ASME*, vol. 135, no. 5, pp. 0 510 061–0 510 068, 2013.

[53] X. Lu, J. F. Kolb, S. Xiao, M. Laroussi, K. H. Schoenbach, and E. Schamiloglu, "Dielectric strength of sub-millimeter water gaps subjected to microsecond and sub-microsecond voltage pulses," in *Pulsed Power Conference, 2005 IEEE*, 2005, pp. 600–603.

[54] Y. S. Wong, M. Rahman, H. S. Lim, H. Han, and N. Ravi, "Investigation of micro-edm material removal characteristics using single rc-pulse discharges," *Journal of Materials Processing Technology*, vol. 140, no. 13, pp. 303–307, 2003.

[55] G. G. Boothroyd, *Fundamentals of Machining and Machine Tools.* CRC/Taylor and Francis, Boca Raton, 2006.

[56] J. E. Fuller, "Electrical Discharge Machining," *ASM Handbook, Machining*, vol. 16, pp. 557–564, 1990.

[57] L. Houman, "How to estimate edm time requirements," *Met. Stamp., Vol 11, Page 15*, vol. 16, pp. 557–564, 1977.

[58] P. M. Lonardo and A. A. Bruzzone, "Effect of flushing and electrode material on die sinking edm," *CIRP Annals - Manufacturing Technology*, vol. 48, no. 1, pp. 123–126, 1999.

[59] Y. S. Wong, L. C. Lim, and L. C. Lee, "Effects of flushing on electro-discharge machined surfaces," *Journal of Materials Processing Tech.*, vol. 48, no. 1-4, pp. 299–305, 1995.

[60] S. H. Lee and X. P. Li, "Study of the effect of machining parameters on the machining characteristics in electrical discharge machining of tungsten carbide," *Journal of Materials Processing Technology*, vol. 115, no. 3, pp. 344–358, 2001.

[61] G. F. Benedict, *Electrical Discharge Machining, Non-traditional Manufacturing Processes.* Marcel-Dekker Inc., New York and Basel, 1987.

[62] H. K. Tonshoff, R. Egger, and F. Klocke, "Environmental and safety aspects of electrophysical and electrochemical processes," *CIRP Annals - Manufacturing Technology*, vol. 45, no. 2, pp. 553–568, 1996.

[63] K. Roger, "Safe and green edming," *EDM Today, July August Issue, pp. 22-25*, vol. 16, pp. 557–564, 2008.

[64] S. P. Sivapirakasam, J. Mathew, and M. Surianarayanan, "Multi-attribute decision making for green electrical discharge machining," *Expert Systems with Applications*, vol. 38, no. 7, pp. 8370–8374, 2011.

[65] C. Furudate and M. Kunieda, "Fundamental study on dry-wedm," *Seimitsu Kogaku Kaishi/Journal of the Japan Society for Precision Engineering*, vol. 67, no. 7, pp. 1180–1184, 2001.

[66] Z. Yu, T. Jun, and K. Masanori, "Dry electrical discharge machining of cemented carbide," *Journal of Materials Processing Technology*, vol. 149, no. 1-3, pp. 353–357, 2004.

[67] N. NTIS Tech Note, Ed., *Inert Gas Electrical Discharge Machining*, 1985.

[68] T. O. Hockenberry and E. M. Williams, "Dynamic evolution of events accompanying the low-voltage discharges employed in edm," *Industry and General Applications, IEEE Transactions on*, vol. IGA-3, no. 4, pp. 302–309, 1967.

[69] M. Kunieda and C. Furudate, "High precision finish cutting by dry wedm," *CIRP Annals - Manufacturing Technology*, vol. 50, no. 1, pp. 121–124, 2001.

[70] L. Q. Li, Z. L. Wang, and W. S. Zhao, "Mechanism analysis of Electrical Discharge Machining in gas," *Harbin Gongye Daxue Xuebao/Journal of Harbin Institute of Technology*, vol. 36, no. 3, pp. 359–362, 2004.

[71] M. L. Jeswani, "Electrical discharge machining in distilled water," *Wear*, vol. 72, no. 1, pp. 81–88, 1981.

[72] W. Konig and F. J. Siebers, "In?uence of the working medium on the removal process in edm sinking." *American Society of Mechanical Engineers, Production Engineering Division (Publication) PED 64*, p. 649658, 1993.

[73] R. Kranz, F. Wendl, and K. D. Wupper, "Influence of edm conditions on the toughness of tool steels," *Thyssen Edelstahl Technische Berichte*, pp. 100–105, 1990.

[74] W. Konig and L. Jorres, "Aqueous solutions of organic compounds as dielectrics for edm sinking," *CIRP Annals - Manufacturing Technology*, vol. 36, no. 1, pp. 105–109, 1987.

[75] A. C. Wang, B. H. Yan, Y. X. Tang, and F. Y. Huang, "The feasibility study on a fabricated micro slit die using micro edm," *International Journal of Advanced Manufacturing Technology*, vol. 25, no. 1-2, pp. 10–16, 2005.

[76] T. Kaneko and T. Onodera, "Improvement in machining performance of die-sinking edm by using self-adjusting fuzzy control," *Journal of Materials Processing Technology*, vol. 149, no. 1-3, pp. 204–211, 2004.

[77] W. Zhao, W. Liu, Z. Wang, S. Di, and Q. Meng, "Research on miniaturized edm device with differential reciprocating electrode driving method," *Jixie Gongcheng Xuebao/Chinese Journal of Mechanical Engineering*, vol. 36, no. 9, pp. 65–68, 2000.

[78] J. Wang, F. Han, and F. Zhao, "Improvement of edm efficiency with a new adaptive control strategy," *International Journal of Advanced Manufacturing Technology*, vol. 62, no. 9-12, pp. 1025–1040, 2012.

[79] T. Masuzawa and C. J. Heuvelman, "A self-flushing method with spark-erosion machining," *CIRP Annals - Manufacturing Technology*, vol. 32, no. 1, pp. 109–111, 1983.

[80] T. Sato, T. Mizutani, K. Yonemochi, and K. Kawata, "The development of an electrodischarge machine for micro-hole boring," *Precision Engineering*, vol. 8, no. 3, pp. 163–168, 1986.

[81] J. S. Soni and G. Chakraverti, "Machining characteristics of titanium with rotary electro-discharge machining," *Wear*, vol. 171, no. 1-2, pp. 51–58, 1994.

[82] E. Bamberg and S. Heamawatanachai, "Orbital electrode actuation to improve efficiency of drilling micro-holes by micro-edm," *Journal of Materials Processing Technology*, vol. 209, no. 4, pp. 1826–1834, 2009.

[83] G. S. Prihandana, M. Mahardika, M. Hamdi, and K. Mitsui, "Effect of low-frequency vibration on workpiece in edm processes," *Journal of Mechanical Science and Technology*, vol. 25, no. 5, pp. 1231–1234, 2011.

[84] H. Tong, Y. Li, and Y. Wang, "Experimental research on vibration assisted edm of micro-structures with non-circular cross-section," *Journal of Materials Processing Technology*, vol. 208, no. 1-3, pp. 289–298, 2008.

[85] S. Enache, C. Opran, G. Stoica, and E. Strajescu, "The study of edm with forced vibration of tool-electrode*," *CIRP Annals - Manufacturing Technology*, vol. 39, no. 1, pp. 167–170, 1990.

[86] A. Abdullah and M. R. Shabgard, "Effect of ultrasonic vibration of tool on electrical discharge machining of cemented tungsten carbide (wc-co)," *International Journal of Advanced Manufacturing Technology*, vol. 38, no. 11-12, pp. 1137–1147, 2008.

[87] V. S. R. Murti and P. K. Philip, "Comparative analysis of machining characteristics in ultrasonic assisted edm by the response surface methodology." *International Journal of Production Research*, vol. 25, no. 2, pp. 259–272, 1987.

[88] Z. N. Guo, T. C. Lee, T. M. Yue, and W. S. Lau, "A study of ultrasonic-aided wire electrical discharge machining," *Journal of Materials Processing Technology*, vol. 63, no. 1-3, pp. 823–828, 1997.

[89] D. Kremer, C. Lhiaubet, and A. Moisan, "A study of the effect of synchronizing ultrasonic vibrations with pulses in edm," *CIRP Annals - Manufacturing Technology*, vol. 40, no. 1, pp. 211–214, 1991.

[90] G. S. Prihandana, M. Mahardika, M. Hamdi, Y. S. Wong, and K. Mitsui, "Effect of micro-powder suspension and ultrasonic vibration of dielectric fluid in micro-edm processes-taguchi approach," *International Journal of Machine Tools and Manufacture*, vol. 49, no. 12-13, pp. 1035–1041, 2009.

[91] T. B. Thoe, D. K. Aspinwall, and N. Killey, "Combined ultrasonic and electrical discharge machining of ceramic coated nickel alloy," *Journal of Materials Processing Technology*, vol. 92-93, pp. 323–328, 1999.

[92] B. H. Yan, A. C. Wang, C. Y. Huang, and F. Y. Huang, "Study of precision micro-holes in borosilicate glass using micro edm combined with micro ultrasonic vibration machining," *International Journal of Machine Tools and Manufacture*, vol. 42, no. 10, pp. 1105–1112, 2002.

[93] Q. H. Zhang, J. H. Zhang, J. X. Deng, Y. Qin, and Z. W. Niu, "Ultrasonic vibration electrical discharge machining in gas," *Journal of Materials Processing Technology*, vol. 129, no. 1-3, pp. 135–138, 2002.

[94] S. H. Yeo and L. K. Tan, "Effects of ultrasonic vibrations in micro electro-discharge machining of microholes," *Journal of Micromechanics and Microengineering*, vol. 9, no. 4, pp. 345–352, 1999.

[95] B. X. Jia, D. S. Wang, and J. Z. Guo, *Machining deep micro holes by EDM with USM in inversion installing*, ser. Materials Science Forum, 2009, vol. 626 627.

[96] Y.-C. Lin and H.-S. Lee, "Machining characteristics of magnetic force-assisted edm," *International Journal of Machine Tools and Manufacture*, vol. 48, no. 11, pp. 1179–1186, 9 2008.

[97] H. E. D. Bruijn, T. H. Delft, and A. J. Pekelharing, "Effect of a magnetic field on the gap cleaning in edm," *Annals of CIRP,27*, pp. 93–95, 1978.

[98] R. Teimouri and H. Baseri, "Effects of magnetic field and rotary tool on edm performance," *Journal of Manufacturing Processes*, vol. 14, no. 3, pp. 316–322, 2012.

[99] Y. Zhang and M. B. G. Jun, "Mixed jet of independently atomized water and oil sprays as cutting fluids in micro-milling," *Manufacturing Letters*, vol. 1, no. 1, pp. 13–16, 2013.

[100] C. Nath, S. G. Kapoor, A. K. Srivastava, and J. Iverson, "Effect of fluid concentration in titanium machining with an atomization-based cutting fluid (acf) spray system," *Journal of Manufacturing Processes*, vol. 15, no. 4, pp. 419–425, 2013.

[101] C. Nath, S. G. Kapoor, A. K. Srivastava, and J. Iverson, "Study of droplet spray behavior of an atomization-based cutting fluid spray system for machining titanium alloys," *Journal of Manufacturing Science and Engineering, Transactions of the ASME*, vol. 136, no. 2, 2014.

[102] I. Ghai, J. Wentz, R. E. DeVor, S. G. Kapoor, and J. Samuel, "Droplet behavior on a rotating surface for atomization-based cutting fluid application in micromachining," *Journal of Manufacturing Science and Engineering, Transactions of the ASME*, vol. 132, no. 1, pp. 0 110 171–01 101 710, 2010.

[103] M. Dobre and L. Bolle, "Practical design of ultrasonic spray devices: experimental testing of several atomizer geometries," *Experimental Thermal and Fluid Science*, vol. 26, no. 2–4, pp. 205–211, 2002.

[104] A. H. Lefebvre, *Atomization and sprays*. New York: Hemisphere Pub. Corp., 1989.

[105] D. W. Stanton and C. J. Rutland, "Multi-dimensional modeling of thin liquid films and spray-wall interactions resulting from impinging sprays," *International Journal of Heat and Mass Transfer*, vol. 41, no. 20, pp. 3037–3054, 1998.

[106] C. D. Stow and M. G. Hadfield, "An experimental investigation of fluid flow resulting from the impact of a water drop with an unyielding dry surface," *Proceedings of the Royal Society of London. A. Mathematical and Physical Sciences*, vol. 373, no. 1755, pp. 419–441, 1981.

[107] S. M. N. Khatami and O. J. Ilegbusi, "Modeling of aerosol spray characteristics for synthesis of mixed-oxide nanocomposite sensor film," in *ASME 2011 International Mechanical Engineering Congress and Exposition, IMECE 2011*, vol. 11, 2011, pp. 581–589.

[108] *Ultrasonic atomizers*. Sonics and Materials, Inc., Newtown, CT, USA, http://www.sonics.com/liquid-datasheet/Atomizers.pdf. PDF file. [Online]. Available: http://www.sonics.com/liquid-datasheet/Atomizers.pdf

[109] *ANSYS Academic Research, Release 15.0, Help System, Ansys Fluent User's Guide, ANSYS, Inc.*

[110] *ANSYS Academic Research, Release 15.0, Help System, Ansys Fluent Tutorial Guide, ANSYS, Inc.*

[111] *ANSYS Academic Research, Release 15.0, Help System, Ansys Fluent Theory Guide, ANSYS, Inc.*

[112] S. A. Morsi and A. J. Alexander, "An investigation of particle trajectories in two-phase flow systems," *Journal of Fluid Mechanics*, vol. 55, pp. 193–208, 9 1972.

[113] A. L. Yarin and D. A. Weiss, "Impact of drops on solid surfaces: self-similar capillary waves, and splashing as a new type of kinematic discontinuity," *Journal of Fluid Mechanics*, vol. 283, pp. 141–173, 1995.

[114] P. O. Witze, "Centerline velocity decay of compressible free jets." *AIAA Journal*, vol. 12, no. 4, pp. 417–418, 1974.

[115] K. J. Boughner, J. E. Wentz, and B. J. Garske, "Development and validation of a mathematical model of microfilm formation in atomization cooling of micromachining," in *ASME 2011 International Mechanical Engineering Congress and Exposition, IMECE 2011*, vol. 3, 2011, pp. 667–676.

[116] S. Cetin, A. Okada, and Y. Uno, "Effect of debris distribution on wall concavity in deep-hole edm," *JSME International Journal, Series C: Mechanical Systems, Machine Elements and Manufacturing*, vol. 47, no. 2, pp. 553–559, 2004.

[117] A. Pattabhiraman, D. Marla, and S. G. Kapoor, "Atomized dielectric spray-based Electric Discharge Machining (Spray-EDM) for sustainable manufacturing," in *Proceedings of 2015 ASME Manufacturing Science and Engineering Conference, Charlotte, USA, MSEC 2015-9348.*, 2015.

[118] K. Rajurkar and S. Pandit, "Formation and ejection of edm debris." *Journal of engineering for industry*, vol. 108, no. 1, pp. 22–26, 1986.

[119] S. Mujumdar, D. Curreli, S. G. Kapoor, and D. Ruzic, "A model of micro Electro-Discharge Machining plasma discharge in deionized water," *Journal of Manufacturing Science and Engineering, Transactions of the ASME*, vol. 136, no. 3, 2014.

[120] M. Patel, M. Barrufet, P. Eubank, and D. DiBitonto, "Theoretical models of the electrical discharge machining process. ii. the anode erosion model," *Journal of Applied Physics*, vol. 66, no. 9, pp. 4104–4111, 1989.

[121] A. Zaky, I. Megahed, and M. El-Awa, "Effect of liquid flow velocity on the breakdown voltage of mineral oil under highly nonuniform fields," 1990, pp. 564–568.

[122] A. Zaky, I. Megahed, and M. Abdallah, "Effect of cross-field flow on conduction current and breakdown in transformer oil using point-to-plane electrodes and direct voltage," 1996, pp. 283–286.

[123] C. Huh and S. Mason, "Effects of surface roughness on wetting," *Journal of Colloid and Interface Science*, vol. 60, no. 1, pp. 11 – 38, 1977.